1 **The fate of pyruvate dictates cell growth by modulating cellular redox potential**

2

3 Ashish G. Toshniwal[1], Geanette Lam[1], Alex J. Bott[1], Ahmad A. Cluntun[1, 5], Rachel Skabelund[1],

4 Hyuck-Jin Nam[2], Dona R. Wisidagama[2], Carl S. Thummel[2] and Jared Rutter[1, 3, 4]

5

6 **Affiliations:**

7 [1] Department of Biochemistry, University of Utah, Salt Lake City, UT 84132, USA

8 [2] Department of Human Genetics, University of Utah, Salt Lake City, UT 84132, USA

9 [3] Howard Hughes Medical Institute, University of Utah School of Medicine, Salt Lake City, UT

10 84132, USA

11 [4] Lead Contact

12 [5] Present address: Department of Biochemistry & Molecular Biology, Rutgers Robert Wood

13 Johnson Medical School, Piscataway, NJ 08854

14

15 **Abstract**

16 Pyruvate occupies a central node in carbohydrate metabolism such that how it is produced and

17 consumed can optimize a cell for energy production or biosynthetic capacity. This has been

18 primarily studied in proliferating cells, but observations from the post-mitotic *Drosophila* fat body

19 led us to hypothesize that pyruvate fate might dictate the rapid cell growth observed in this organ

20 during development. Indeed, we demonstrate that augmented mitochondrial pyruvate import

21 prevented cell growth in fat body cells *in vivo* as well as in cultured mammalian hepatocytes and

22 human hepatocyte-derived cells *in vitro*. This effect on cell size was caused by an increase in the

23 NADH/NAD$^+$ ratio, which rewired metabolism toward gluconeogenesis and suppressed the

24 biomass-supporting glycolytic pathway. Amino acid synthesis was decreased, and the resulting

25 loss of protein synthesis prevented cell growth. Surprisingly, this all occurred in the face of

26 activated pro-growth signaling pathways, including mTORC1, Myc, and PI3K/Akt. These

27 observations highlight the evolutionarily conserved role of pyruvate metabolism in setting the

28 balance between energy extraction and biomass production in specialized post-mitotic cells.

29

30 **Introduction**

31 Cells must appropriately allocate available nutrients to optimize their metabolic

32 programs— for energy extraction and for the generation of building blocks that enable cell growth.

33   The balance between these processes not only maintains cellular health under varying nutritional

34   conditions but also plays an important role in determining cell fate and function (Baker & Rutter,

35   2023; DeBerardinis & Thompson, 2012; Ghosh-Choudhary et al., 2020; Metallo & Vander Heiden,

36   2013). For example, hepatocyte metabolism changes considerably between fed and fasted

37   conditions. In the fed state, hepatocytes use the majority of their nutrients to synthesize proteins,

38   lipids, and glycogen, which results in increased cell size and liver biomass (Kast et al., 1988;

39   Reinke & Asher, 2018; Sinturel et al., 2017). To meet the energy demands of other tissues during

40   fasting, the liver undergoes a metabolic shift to produce glucose from biosynthetic precursors,

41   thereby decreasing hepatocyte and liver size (Lang et al., 1998; Sinturel et al., 2017).

42   The metabolic pathways that support biosynthetic metabolism can be inappropriately

43   activated in diseases such as cancer and heart failure to promote pathological growth. For

44   example, many of the primary oncogenic adaptations in tumors prioritize anabolic metabolism

45   over ATP production, which facilitates rapid cell proliferation (Lunt & Vander Heiden, 2011;

46   Vander Heiden et al., 2009; Zhu & Thompson, 2019). Metabolic rewiring during heart failure

47   similarly results in greater biosynthetic potential and less efficient ATP production, which in post-

48   mitotic cardiomyocytes leads to increased cell size and insufficient cardiac pumping (Bornstein et

49   al., 2024; Henry et al., 2024; Weiss et al., 2023).

50   The fate of pyruvate, which is primarily generated from glucose via glycolysis in the

51   cytoplasm, is a critical node that can determine the balance between energetic and biosynthetic

52   metabolism (Baker & Rutter, 2023; Yiew & Finck, 2022). In most differentiated cells, the majority

53   of pyruvate is transported into the mitochondria via the mitochondrial pyruvate carrier (MPC)

54   complex, a heterodimer composed of MPC1 and MPC2 proteins (Bricker et al., 2012; Herzig et

55   al., 2012). Once in the mitochondria, pyruvate is converted to acetyl-CoA by the pyruvate

56   dehydrogenase complex (PDH), fueling the tricarboxylic acid (TCA) cycle and supporting efficient

57   ATP production. In cancer, stem, and other proliferative cells, more pyruvate is converted to

58   lactate and exported from the cell, a process that regenerates NAD^+, a cofactor necessary for

59   glycolytic flux (Baker & Rutter, 2023; Lunt & Vander Heiden, 2011; Zhu & Thompson, 2019). In

60   some specialized cells, including hepatocytes, pyruvate is imported into mitochondria but

61   converted to oxaloacetate, which can feed the TCA cycle but also serves as a precursor for

62   glucose production via gluconeogenesis (Holecek, 2023b; Jitrapakdee et al., 2008). We and

63   others have demonstrated that these alternative fates of pyruvate—energy generation, cell

64   proliferation, or glucose production—differentially impact the metabolic and fate decisions of

65   multiple cell types in varying contexts (Bensard et al., 2020; Cluntun et al., 2021; Wei et al., 2022;

66   Yiew & Finck, 2022). Loss of MPC function, which shifts pyruvate metabolism toward lactate

67   production and thus expedites glycolysis and the production of biosynthetic precursors, has been

68   shown to increase cell proliferation in mouse and *Drosophila* intestinal stem cells as well as in

69   various tumors (Bensard et al., 2020; Schell et al., 2017; Zangari et al., 2020). MPC expression

70   is also reduced in human and mouse models of heart failure, and genetic deletion of the MPC in

71   cardiomyocytes is sufficient to induce hypertrophy and heart failure (Cluntun et al., 2021;

72   Fernandez-Caggiano et al., 2020; McCommis et al., 2020; Zhang et al., 2020). Conversely, MPC

73   overactivation or overexpression restricts intestinal stem cell proliferation and limits the growth of

74   cardiomyocytes under hypertrophic stimuli, with excess mitochondrial pyruvate fueling the TCA

75   cycle (Bensard et al., 2020; Schell et al., 2014; Schell et al., 2017). These observations suggest

76   that mitochondrial pyruvate metabolism is central to cell proliferation as well as the size and

77   specialized functions of post-mitotic cells.

78   The mechanisms regulating cell size include well-characterized cellular signaling

79   pathways and transcriptional programs (Grewal, 2009; Liu et al., 2022; Lloyd, 2013). The CDK4-

80   Rb pathway monitors cell size in proliferating cells by coupling cell growth with cell division

81   (Amodeo & Skotheim, 2016; Ginzberg et al., 2018; Tan et al., 2021; Zhang et al., 2022). In

82   response to insulin and other growth factors, the PI3K/Akt pathway activates mTORC1, leading

83   to increased biosynthesis of proteins, lipids, and nucleotides, and consequently, increased cell

84   size (Gonzalez & Hall, 2017; Gonzalez & Rallis, 2017; Saxton & Sabatini, 2017). The pro-growth

85   transcription factor Myc drives a gene expression program that enhances metabolic activity and

86   protein synthesis, resulting in larger cells (Baena et al., 2005; Dang, 1999; Iritani & Eisenman,

87   1999; Stine et al., 2015; van Riggelen et al., 2010). However, we only partially understand how

88   metabolic pathways regulate physiological (or pathophysiological) growth, particularly in cells that

89   have distinct and specialized roles in organismal metabolism.

90   Here, we investigated whether pyruvate metabolism influences biosynthetic capacity and

91   cell size, using the *Drosophila* fat body as a model of the mammalian liver. We found that MPC

92   overexpression and increased mitochondrial pyruvate transport restrict cell growth and limit

93   protein synthesis in larval fat body cells and in spheroids of human liver-derived cells. Higher MPC

94   expression resulted in smaller cells, not by increasing TCA cycle flux as observed in other cell

95   types, but instead by redirecting mitochondrial pyruvate metabolism towards gluconeogenesis. A

96   key driver of this metabolic rewiring is a reduced cellular redox state, which disrupts the

97   biosynthesis of TCA cycle-derived amino acids, such as aspartate and glutamate, ultimately

98   reducing protein synthesis. These observations highlight how cells with specialized functions, like

99   hepatocytes, employ distinct metabolic adaptations to respond to organismal demands under

100   varying nutritional conditions.

101

102   **Results**

103   **Increased mitochondrial pyruvate transport reduces the size of *Drosophila* fat body cells**

104   The *Drosophila* fat body is functionally analogous to mammalian white adipose tissue and

105   liver, serving as a buffer to store excess nutrients in fat droplets and glycogen and deploy them

106   to support the animal with fuel during times of fasting (Arrese & Soulages, 2010; Musselman et

107   al., 2013). During larval development, fat body cells halt cell division and dramatically increase in

108   size during the third instar stage (from 72 to 120 hours After Egg Laying (AEL)) (Edgar & Orr-

109   Weaver, 2001; Zheng et al., 2016) (Fig. 1a-c). As a first step to understand the metabolic

110   programs that enables this rapid cell growth, we performed RNA-sequencing of the *Drosophila*

111   fat body across this developmental period. We observed a time-dependent change in mRNAs

112   encoding proteins that have well-characterized roles in supporting cell growth, including

113   components of the insulin and mTORC1 signaling pathways and the Myc transcriptional network

114   which correlated with increased cell size (Supplementary Fig. 1a). Amongst metabolic genes, we

115   observed modest differences in those that function in amino acid synthesis and fatty acid

116   metabolism (Supplementary Fig. 1b). The abundances of mRNAs encoding proteins involved in

117   glycolysis, oxidative phosphorylation (OxPhos), and the TCA cycle were distinctly altered in fat

118   bodies during development (Supplementary Fig. 1b). Since pyruvate metabolism is the central

119   node connecting carbohydrate metabolism and the TCA cycle, we studied the abundances of

120   mRNAs that encode proteins that regulate pyruvate metabolism (Fig. 1d). We found that the

121   expression of genes that link pyruvate to the TCA cycle were reduced including, *Pyk,* the

122   *Drosophila* pyruvate kinase homolog, which converts phosphoenolpyruvate into pyruvate; *Mpc1*

123   and *Mpc2,* which encode the two subunits of the MPC, which transports pyruvate into the

124   mitochondrial matrix; as well as *Pdha* and *Dlat,* which encode subunits of PDH complex (Fig. 1e).

125   In contrast, some mRNAs encoding proteins that regulate pyruvate abundance were upregulated

126   such as *Pepck* and *Pepck2*, which make phosphoenolpyruvate from oxaloacetate

127   (Supplementary Fig. 1c). Based on these data, we hypothesized that the suppression of

128   mitochondrial pyruvate metabolism, which is gated by the action of the MPC, might support the

129   rapid cell growth observed in fat body cells.

130   To test this hypothesis, we prevented the downregulation of the MPC during larval

131   development (Fig. 1e) by ectopically expressing *Mpc1* and *Mpc2* (termed "MPC+" Supplementary

132   Fig. 2a, 2b). The sustained expression of the MPC (both *Mpc1* and *Mpc2*) throughout the fat body

133   significantly reduced the rate of cell growth compared to a GFP-expressing control

134   (Supplementary Fig. 2c). Given the important role of the fat body in controlling organismal growth,

135   we wanted to assess the cell-autonomous effects of MPC expression using mosaic analysis in

136   individual fat body cells (Supplementary Fig. 2d) (Ito et al., 1997). We generated GFP-labeled

137   clones with expression of the MPC (MPC+), which we confirmed by immunofluorescence

138   (Supplementary Fig. 2e, f). The MPC-expressing, GFP-positive cells were significantly smaller in

139   size compared with either mock clones (control) or neighboring GFP-negative cells within the

140   same tissue. *Mpc1* knock down (*Mpc1*-KD) clones, in contrast, were marginally larger (Fig. 1f-g).

141   These results demonstrate that sustained expression of the MPC in developing fat body cells is

142   sufficient to prevent cell growth in a cell-autonomous manner.

143   If the effects of MPC expression were related to the mitochondrial transport of pyruvate,

144   then limiting the production of pyruvate should mitigate these effects. Therefore, we measured

145   cell size in larvae raised on either a normal (9% sugar) diet or a diet with no added sugars, which

146   limits the production of pyruvate from glucose and fructose. Limiting dietary sugars significantly

147   reduced the size of control clones but increased the size of MPC-expressing clones. Notably, the

148   size of MPC-expressing fat body clones was comparable to that of control clones when larvae

149   were grown in sugar-limited medium, suggesting that limiting pyruvate synthesis abolishes the

150   effect of MPC expression on fat body cell size (Fig. 1h, i). *Mpc1*-KD clones were again larger than

151   control cells and their size was unaffected by the sugar-limited diet. Inhibiting MPC activity by

152   feeding larvae a normal diet supplemented with the MPC inhibitor UK5099 ameliorated the cell

153   size effects of MPC expression (Fig. 1j and Supplementary Fig. 2g). These results indicate that

154   pyruvate transport into mitochondria inversely correlates with the size gain in fat body cells. These

155   observations also suggest that the suppression of mitochondrial pyruvate import, and metabolism

156   is required for the rapid cell size expansion observed in the fat body during larval development.

157   The size of a cell is determined by its content of proteins, nucleic acids, and lipids

158   (Bjorklund, 2019; Lloyd, 2013; Schmoller & Skotheim, 2015). To understand how MPC expression

159   affects the abundance of these macromolecules, we dissected fat bodies from control and fat

160   body-wide MPC-expressing larvae at 120 hours AEL and quantified DNA, RNA, triacylgylcerides,

161   and protein. Control and MPC+ fat bodies had equivalent DNA content (Fig. 1k, Supplementary

162   Fig. 2h) and similar levels of EdU incorporation (Supplementary Fig 2o, p), suggesting that MPC

163   expression does not impact DNA endoreplication. RNA and lipid content were modestly

164   decreased in MPC+ fat bodies compared with control tissues (Fig. 1k, Supplementary Fig. 2i, j),

165   although the number of lipid droplets was higher with MPC expression (Supplementary Fig 2l-n).

166   In contrast, MPC expression dramatically decreased protein abundance in fat bodies (Fig. 1k,

167   Supplementary Fig. 2k), and reduced protein synthesis as assessed by staining for the puromycin

168   analog, O-propargyl-puromycin (OPP) (Deliu et al., 2017; Villalobos-Cantor et al., 2023) (Fig. 1l,

169   m). These data suggest that MPC-mediated mitochondrial pyruvate import decreases protein

170   synthesis, which likely contributes to the reduced size of MPC-expressing cells. Conversely, in

171   developing fly larvae, repression of the MPC and the subsequent decrease in mitochondrial

172   pyruvate appear to provide a metabolic mechanism to support a rapid expansion in cell size.

173

174   **Growth factor signaling pathways are hyperactivated in MPC expressing cells**

175   The best understood mechanisms that govern cell size involve conserved signaling and

176   transcriptional networks (Bjorklund, 2019; Grewal, 2009; Lang et al., 1998; Lloyd, 2013). For

177   example, the mTORC1 pathway coordinates both extracellular and intracellular growth regulatory

178   signals to dictate the synthesis and degradation of macromolecules, including proteins, lipids, and

179   nucleic acids (Gonzalez & Hall, 2017; Gonzalez & Rallis, 2017; Saxton & Sabatini, 2017).

180   mTORC1 increases protein synthesis through the phosphorylation of several proteins, including

181   S6 kinase (S6K) and 4EBP1 (Fig. 2a). Since MPC-expressing clones were smaller in size and

182   had reduced protein synthesis compared with control clones, we assessed mTORC1 activity in

183   the fat body using our mosaic expression system. As a control, we confirmed that *S6k* (the

184   *Drosophila* gene encoding S6K) over-expressing clones were larger in size and had elevated

185   phospho-S6 staining compared with wild-type clones (Fig. 2b, c). Surprisingly, MPC+ clones also

186   had elevated phospho-S6 staining (Fig. 2b, c), suggesting that despite their small size, these cells

187   have high mTORC1 activity. Over-expression of *Rheb*, which is an upstream activator of

188   mTORC1, resulted in clones that were larger than wild-type controls and which had increased

189   phospho-4EBP1 staining (Fig. 2d, e). Again, even though the MPC+ clones were smaller in size,

190   we observed robust p-4EBP1 staining, indicating that mTORC1 is hyperactive in these cells.

191   Gene set enrichment analysis of RNA-sequencing data from MPC-expressing fat bodies

192   showed enrichment for signatures associated with pro-growth signaling (Supplementary Fig. 3a).

193   We assessed markers of several of these pathways in MPC+ clones. In addition to the mTORC1

194   pathway, Myc increases cell growth by regulating the transcription of ribosome subunits and

195   biosynthetic metabolic genes. We found that MPC+ clones had an elevated abundance of the

196   Myc protein, both in the cytoplasm and nucleus, (Fig. 2f, g), suggesting that the growth-promoting

197   Myc transcriptional program is active in these cells. MPC+ clones also had reduced expression

198   of the transcription factor Foxo, consistent with its downregulation by pro-growth signaling

199   pathways (Supplementary Fig. 3b). Finally, we stained for phospho-eIF2α to assess the activity

200   of the integrated stress response, which restricts global protein synthesis. Starvation robustly

201   induced the integrated stress response in control clones, but MPC+ clones exhibited no evidence

202   of activation of this pathway under normal growth conditions (Fig. 2h, i). Collectively these data

203   indicate that conventional pro-growth pathways are activated in MPC-expressing clones, which is

204   incongruent with the small size of the clones. This suggests that mitochondrial pyruvate

205   metabolism controls cell size via alternative molecular mechanisms.

206   We next performed genetic epistasis analysis to better understand the relationship

207   between MPC expression and the mTORC1, PI3K, and Myc pathways. Activation of the PI3K or

208   mTORC1 pathways, via over-expression of *PI3K*, increased the size of control but not MPC-

209   expressing fat body cells (Supplementary Fig. 3c). Similarly, activation of mTORC1 via knock

210   down of its inhibitor, Tuberous Sclerosis Complex 1 (*Tsc1*), increased the size of control cells but

211   had no effect on MPC+ cell size (Supplementary Fig. 3d). Over-expression of *Myc*, on the other

212   hand, increased the size of control and MPC+ fat body clones to a similar degree (Supplementary

213   Fig. 3e). Knock down of *Myc* was sufficient to decrease cell size to a similar extent as MPC

214   expression; however, *Myc* knock down had no additional effect on cell size in MPC+ clones

215   (Supplementary Fig. 3f). These results suggest that neither mTORC1, PI3K, nor Myc are epistatic

216   to MPC and suggest that MPC likely acts independently of these canonical pathways to regulate

217   the size of fat body cells.

218

Increased mitochondrial pyruvate transport reduces the size of HepG2 cells and spheroids

220   Since the *Drosophila* fat body has many features reminiscent of the mammalian liver, we

221   tested whether MPC expression might similarly restrict cell size in cells derived from this tissue.

222   We engineered HepG2 cells, which were originally isolated from a hepatocellular carcinoma, to

223   express epitope tagged-MPC1 and MPC2 in a doxycycline-inducible manner. We observed

224   expression of ectopic MPC1 and MPC2 starting at four hours after doxycycline treatment, which

225   increased over the duration of the time course, peaking at 24 hours post-induction (Fig. 3a). We

226   stained doxycycline-treated cells with phalloidin and measured cell size using microscopy images

227   taken at two-hour intervals. Induction of MPC expression coincided with a significant reduction in

228   cell size, which was first apparent six hours post-doxycycline treatment and was sustained for the

229   remainder of the time course (Fig. 3b). Doxycycline had no effect on the size of control HepG2

230   cells (EV). Treatment with the MPC inhibitor UK5099 for 24 hours markedly increased the size of

231   control cells and partially reversed the small size phenotype of MPC-expressing cells (Fig. 3c).

232   We also assessed cell volume by analyzing a 3D reconstruction of confocal images of phalloidin-

233   stained HepG2 cells and found that the cell volume was lower in MPC+ cells (Supplementary Fig.

234   4a).

235   We have observed that the physiological consequences of altered pyruvate metabolism

236   are more apparent in cells grown in a three-dimensional culture environment (Schell et al., 2014;

237   Wei et al., 2022). Using our doxycycline-inducible cells, we found that MPC expression resulted

238   in spheroids that were significantly smaller than control spheroids as assessed by microscopy

239   (Fig. 3d, e). Cells from MPC-expressing spheroids were also smaller as shown by flow cytometry

240   (Fig. 3f, g). When compared with control (EV) spheroids, expression of MPC had no effect on the

241   number of cells per spheroid, on the cell cycle phase distribution, or on the number of apoptotic

242   or necrotic cells (Supplementary Fig. 4b, 4c, and 4d). These analyses suggest that the smaller

243   size observed in MPC expressing spheroids is not due to effects on cell proliferation or cell death.

244   Consistent with our observations in the *Drosophila* fat body, protein content was lower in

245   MPC-expressing HepG2 spheroids compared with EV controls, whereas there was no difference

246   in the abundances of DNA, RNA, or triacylgylcerides (Fig. 3h and Supplementary Fig. 4e-h). To

247   directly assess the effect of MPC expression on protein synthesis, we induced the MPC in HepG2

248   cells and treated cells acutely with a low concentration of puromycin to label nascent proteins.

249   We found that MPC expression decreased the incorporation of the amino acid analog L-

250   homopropargylglycine (HPG) (Shen et al., 2021; Tom Dieck et al., 2012) into nascent proteins,

251   as assessed by fluorescence microscopy (Fig. 3i, j). Protein synthesis was similarly reduced in

252   MPC-expressing HepG2 spheroids (Fig. 3k, l). These observations were further supported by the

253   decreased abundance of the short-lived, destabilized GFP (d2GFP) (Li et al., 1998; Pavlova et

254   al., 2020) in MPC-expressing HepG2 spheroids compared with controls. This reduction in the

255   level of d2GFP was prevented by treatment with the MPC inhibitor UK5099 (Fig. 3m). Together

256   these data suggest that increased transport of pyruvate into mitochondria, mediated by MPC

257   expression, reduces protein synthesis and cell size in both fly and mammalian models.

258

Excess mitochondrial pyruvate promotes gluconeogenesis

260   We have previously shown that loss of the MPC reduces the contribution of glucose and

261   pyruvate to the TCA cycle (Bensard et al., 2020; Cluntun et al., 2021). To investigate how MPC

262   expression impacts carbohydrate metabolism in HepG2 cells, we performed metabolic tracing

263   using ^{13}C-glucose (Fig. 4a). We observed that MPC expression reduced the labeling fraction of

264   the glycolytic intermediates 3-phosphoglycerate (Supplementary Fig. 5a) and pyruvate

265   (Supplementary Fig. 5b), as well as alanine (Supplementary Fig. 5c), which is derived from

266   pyruvate, all of which suggests a reduction in glycolysis in these cells. Once imported into

267   mitochondria, glycolytic-derived pyruvate has two major fates: conversion to acetyl-CoA by PDH

268   or to oxaloacetate by pyruvate carboxylase (PC). These fates can be differentiated by assessing

269   the abundances of M+2 (derived from PDH) and M+3 (derived from PC) TCA cycle intermediates

270   (Fig. 4a). We found that both M+2 and M+3 isotopomers of TCA cycle intermediates were

271   modestly increased following MPC expression (Fig. 4b and 4c; Supplementary Fig. 5d-g). The

272   fact that we observe increases in TCA cycle intermediates despite decreased glycolytic labeling

273   in pyruvate suggests that the apparent labeling through PDH and PC might be underestimating

274   the effect on metabolic flux through these enzymes. Thus, it appears that MPC expression

275   increases the activity of both enzymes that utilize pyruvate. Typically, when TCA cycle flux is

276   increased, one observes an increase in activity of the electron transport chain (ETC) to oxidize

277   the resulting NADH. However, MPC expression had no impact on ETC activity as assessed by

278   measuring oxygen consumption (Fig. 4d). The implications of elevated NADH production without

279   a concomitant increase in NADH oxidation will be discussed in Fig. 5.

280   To probe the impact of increased flux through the PC and PDH reactions, we conducted

281   genetic epistatic analysis in fat body cells. We found that *Drosophila* fat body clones in which we

282   over-expressed *Pcb* (the *Drosophila* gene encoding pyruvate carboxylase) were significantly

283   smaller than controls and were equivalent in size to MPC+ clones (Fig. 4e, f). Clones expressing

284   both the MPC and *Pcb* were even smaller (Fig. 4e, f). Conversely, knock down of *Pcb* (*Pcb*-KD)

285   in MPC-expressing fat body clones completely rescued the cell size phenotype (Fig. 4e, f and

286   Supplementary Fig. 6a). Knock down of *Pcb* in MPC-expressing HepG2 cells also eliminated the

287   small cell size phenotype (Supplementary Fig. 6b). These data suggested that the small size of

288   cells expressing the MPC is likely due to increased flux through the PC reaction. Consistent with

289   this, knock down of the PDH-E1 (*Drosophila* gene *Pdha*) or PDH-E2 (*Drosophila* gene *Dlat*)

290   subunits of PDH, which should divert mitochondrial pyruvate, so it is preferentially used by PC,

291   also resulted in smaller fat body cells (Supplementary Fig. 6c-d). In contrast, activating PDH by

292   knocking down the inhibitory PDH kinases (mammalian PDKs, *Drosophila* gene *Pdk*) (Stacpoole,

293   2017; Wang et al., 2021), which should promote the flux of pyruvate through PDH and away from

294   PC, rescued cell size in MPC-expressing fat body clones (Supplementary Fig. 6c, d). Similarly, in

295   MPC-expressing HepG2 cells, activation of PDH via treatment with the PDK inhibitors DCA and

296   AZD7545 was sufficient to restore cell size (Supplementary Fig. 6e) (Stacpoole, 2017; Wang et

297   al., 2021). These analyses suggest that the reduction in cell size observed with MPC expression

298   is due to PC-mediated metabolism of pyruvate.

299   The product of PC, oxaloacetate, has three major metabolic fates: 1) feeding the TCA

300   cycle via citrate synthase as discussed above, 2) conversion to aspartate by glutamatic-

301   oxaloacetic transaminase 2 (GOT2), and 3) conversion to phosphoenolpyruvate by PEPCK2

302   leading to gluconeogenesis, synthesis of glucose (Jitrapakdee et al., 2008; Kiesel et al., 2021).

303   Sustained expression of the MPC in fat bodies increased the concentration of glucose in this

304   tissue (Fig. 4g) as well as in larval circulation (known as hemolymph) (Fig. 4h), suggesting that

305   MPC expression increases glucose production in fat body cells. Next, we tested whether

306   PEPCK2-mediated gluconeogenesis was elevated in these cells compared with controls. We

307   used ^{13}C-lactate to trace the ^{13}C-labeling of phosphoenolpyruvate and resultant glucose synthesis

308   via gluconeogenesis (Fig. 4i). We found that the relative abundance of M+3 phosphoenolpyruvate

309   was higher in MPC-expressing cells compared with controls (Fig. 4j), suggesting increased

310   activity of PEPCK2. The gluconeogenic pathway employs a series of biochemical reactions to

311   convert phosphoenolpyruvate into glucose, which is then excreted from the cell. This production

312   of M+6 glucose from lactate was also higher in MPC-expressing HepG2 cells (Fig. 4k). To test

313   whether gluconeogenesis contributes to the small size phenotype of MPC-expressing cells, we

314   knocked down enzymes in the pathway (*Drosophila* phosphoenol carboxykinase, *Pepck2,* and

315   fructose bisphosphatase, *Fbp*) and assessed cell size in *Drosophila* and HepG2 models.

316   Knockout of PEPCK2 in MPC-expressing HepG2 cells resulted in smaller spheroids (Fig. 4l) and

317   cells (Supplementary Fig. 6f). Knock down of either *Pepck2* or *Fbp* partially rescued the size

318   defect in MPC-expressing *Drosophila* fat body clones (Fig. 4n, o Supplementary Fig. 6g), and

319   *Pepck2* knock down also increased protein synthesis in these clones (Fig. 4p, q). Collectively,

320   these data suggest that the cell size and protein synthesis phenotypes observed in MPC-

321   expressing cells require PC-mediated gluconeogenesis, and this relationship is found in both the

322   *Drosophila* fat body and in HepG2 cells.

323

324   **A redox imbalance impairs protein synthesis and cell growth in MPC-expressing cells**

325   We were intrigued by the observation that MPC expression exerted its impact on cell size

326   through PC and not via increased flux through PDH. We did not observe any differences in the

327   abundances of PDH1a, phosphorylated (inactive) PDH1a, PC, PEPCK2, or G6PC proteins in

328   MPC-expressing HepG2 cells (Supplementary Fig. 7a, b). We therefore hypothesized that the

329   shift in pyruvate metabolism in response to MPC expression might be driven by changes in the

330   abundances of enzyme cofactors, metabolite regulators, or cellular redox balance. PC and PDH

331   show reciprocal regulation by such factors: PC utilizes ATP as a substrate and is allosterically

332   activated by acetyl-CoA, whereas PDH is inhibited by ATP, acetyl CoA, and NADH (Chai et al.,

333   2022; Sugden & Holness, 2011) (Supplementary Fig. 7c). In addition, several reactions in

334   gluconeogenesis require ATP or NADH (Hausler et al., 2006; Siess et al., 1977) (Supplementary

335   Fig. 7c). Upon induction of MPC expression in HepG2 cells, we observed increased abundance

336   of acetyl-CoA (Supplementary Fig. 7d), a higher ATP to ADP ratio (Supplementary Fig. 7e), a

337   greater abundance of NADH without an increase in NAD^+, and thus an increase in the cellular

338     $NADH/NAD^+$ ratio (Supplementary Fig. 7f-h). To determine how MPC expression impacts the

339   subcellular distribution of redox factors, we separated cytoplasmic and mitochondrial fractions

340   from control or MPC-expressing *Drosophila* fat bodies and measured the $NADH/NAD^+$ ratio. We

341   found that MPC expression increased the $NADH/NAD^+$ ratio in both the cytoplasm and

342   mitochondria (Fig. 5a). We observed a similar increase in the $NADH/NAD^+$ ratio in both fractions

343   in MPC-expressing HepG2 spheroids (Fig. 5b). These results suggest that the increased

344   abundances of acetyl-CoA, ATP, and NADH in MPC-expressing cells could promote the rewiring

345   of mitochondrial pyruvate metabolism through PC and support gluconeogenesis.

346   To test the hypothesis that ATP or NADH concentrations might affect cell size in MPC-

347   expressing *Drosophila* fat body clones or HepG2 cells, we utilized pharmacological or genetic

348   modulation of these molecules. Treatment with gramicidin, which decreases the ATP to ADP ratio

349   (Xue et al., 2022), did not alter the size of MPC-expressing HepG2 cells (Supplementary Fig. 7i).

350   We used several orthogonal approaches to reduce the cellular $NADH/NAD^+$ ratio in the MPC-

351   expressing systems and measured their effect on cell size. Co-expression of the *Drosophila*

352   nicotinamide mononucleotide adenylyl transferase (*Nmnat)*, which increases NAD^+ biosynthesis,

353   almost normalized the small size phenotype of MPC-expressing clones in the *Drosophila* fat body

354   (Fig. 5c, d). We observed a similar rescue of cell size following expression of the *Ciona intestinalis*

355   alternate Complex I enzyme NADH dehydrogenase (NDX) (Gospodaryov et al., 2020) or the yeast

356   NADH dehydrogenase (NDI) (Sanz et al., 2010), both of which oxidize NADH to NAD^+ without

357   concomitant proton translocation and energy capture (Fig. 5e, f). Expression of NDI in HepG2

358   cells also mitigated the effect of MPC expression on spheroid size (Supplementary Fig. 7j, k), as

359   did treatment with duroquinone (Merker et al., 2006) (Supplementary Fig. 7l), which oxidizes

360   NADH to NAD^+. To extend these investigations to three dimensional culture, we supplemented

361 the growth medium of MPC-expressing HepG2 spheroids with the NAD$^+$ precursors nicotinamide

362 riboside (NR) or nicotinamide mononucleotide (NMN), both of which recovered spheroid size (Fig.

363 5g, h).

364 Since MPC expression reduced protein synthesis in both *Drosophila* fat bodies and

365 HepG2 cells, we tested how cellular redox status might contribute to this phenotype in both

366 systems. Expression of NDX, which lowers the NADH/NAD$^+$ ratio, increased translation in MPC-

367 expressing *Drosophila* fat body clones (Fig. 5i, j). In HepG2 spheroids, boosting NAD$^+$

368 biosynthesis by supplementing growth media with NR or NMN partially rescued the abundance

369 of destabilized GFP (Fig. 5k). These results suggest that the elevated NADH/ NAD$^+$ ratio in MPC-

370 expressing cells limits protein synthesis and that normalizing that ratio increases protein synthesis

371 and cell size.

372

373 **Reduced amino acid abundance impairs size of MPC-overexpressing cells**

374 Given the reduced protein synthesis observed upon MPC expression, we assessed amino

375 acid concentrations in HepG2 using steady-state metabolomics. We found that MPC expression

376 reduced the abundance of most amino acids (Fig. 6a). To test whether the low abundances of

377 amino acids contribute to the smaller size of MPC-expressing cells, we supplemented the growth

378 media of HepG2 spheroids with excess non-essential amino acid (NEAAs)—either two or three

379 times the recommended dilution of a commercially available amino acid cocktail that includes

380 glycine, L-alanine, L-asparagine, L-aspartate, L-glutamate, L-proline, and L-serine. MPC-

381 expressing spheroids grown with excess NEAAs were comparable in size to controls (Fig. 6b, c).

382 In parallel, we provided *Drosophila* larvae with food containing excess (5x) amino acids from 72

383 to 120 hours AEL, which partially rescued cell size in MPC-expressing fat body clones (Fig. 6d,

384 e). To genetically augment intracellular amino acids, we expressed the amino acid importer

385 *slimfast* (Colombani et al., 2003) in control or MPC-expressing fat body clones and found that it

386 prevented the decrease in cell size (Fig. 6f, g).

387 To determine which amino acid(s) contribute to the cell size effects of MPC expression,

388 we cultured control and MPC-expressing HepG2 cells in media supplemented with an excess of

389 each individual amino acid from the NEAA cocktail. Treatment with excess glycine, L-alanine, or

390 L-serine had no effect on cell size (Fig. 6h). However, the size of MPC-expressing cells was

391 normalized by supplementation with L-aspartate, L-glutamate, or L-proline (Fig. 6h), all of which

392 are derived from TCA cycle intermediates. Supplementation with either L-aspartate or L-

393 glutamate also rescued the small size phenotype of MPC-expressing HepG2 spheroids

394   (Supplementary Fig. 8a, b). Increasing L-aspartate uptake by over-expressing the aspartate

395   transporter SLC1A3 also recovered size of HepG2 spheroids (Supplementary Fig. 8c, d). In

396   addition, treatment with excess (3x) NEAA partially restored the abundance of d2GFP in MPC-

397   expressing HepG2 spheroids (Supplementary Fig. 8e), suggesting rescued protein synthesis.

398   Like glutamate and proline, aspartate is derived from a TCA cycle intermediate,

399   specifically via transamination of oxaloacetate by glutamic-oxaloacetate transaminase 2 (GOT2).

400   Since GOT2 and PEPCK2 both use oxaloacetate as a substrate, we hypothesized that knocking

401   down GOT2 might phenocopy MPC expression by driving PEPCK2-mediated conversion of

402   oxalacetate into phosphoenolpyruvate and suppressing aspartate biosynthesis. Knock down of

403   *Got2* (the *Drosophila* gene encoding GOT2) reduced cell size in *Drosophila* fat body clones and

404   phenocopied MPC-expressing cells (Fig. 6i, j). Similarly, both GOT2 knock out and MPC-

405   expressing HepG2 cells were smaller than EV(Supplementary Fig. 8f). Expression of the MPC in

406   these GOT2 knock down systems had no significant impact on cell size (Fig. 6i, j and

407   Supplementary Fig. 8f), suggesting that the effects of MPC expression and GOT2 knock down

408   act similarly to limit amino acid synthesis and cell size. We next performed the reciprocal

409   experiment by over-expressing *Got2* to favor the production of aspartate from oxaloacetate. *Got2*

410   expression normalized cell size in both MPC-expressing fat body clones and in HepG2 spheroids

411   (Fig. 6i, j and Supplementary Fig. 8g, h). The efflux of aspartate from mitochondria into the

412   cytoplasm is a critical component of the malate-aspartate shuttle, which is a major redox shuttle

413   in human cells. To test whether increasing the abundance of aspartate would ameliorate the high

414   NADH/NAD$^+$ ratio observed in MPC-expressing cells, we supplemented growth media with

415   exogenous aspartate and assessed cellular redox status. We found that excess aspartate

416   reduced the cellular NADH/NAD$^+$ ratio in these cells such that it was comparable with control cells

417   (Fig. 6k). We observed similar results when we treated these cells with NMN or UK5099 (Fig. 6k).

418   Moreover, all these treatments increased protein synthesis in MPC-expressing cells (Fig. 6l, m).

419

420   **Mitochondrial pyruvate import reduces the size of rat primary hepatocytes**

421   Although HepG2 cells exhibit some features of hepatocytes, they are a transformed,

422   immortalized, and proliferative hepatocellular carcinoma cell line. We wanted to test whether the

423   MPC expression phenotypes that we observed in *Drosophila* fat bodies and HepG2 cells could

424   be recapitulated in a more physiologically relevant mammalian model. We chose primary rat

425   hepatocytes, which have been used extensively to interrogate hepatocyte cell metabolism and

426   signaling and also have the advantage of being genetically tractable. We expressed MPC1 and

427   MPC2 in cultured primary rat hepatocytes (Fig. 7a), and, consistent with our results in other

428   systems, we found that expression of MPC reduced cell size (Fig. 7b, c) and decreased protein

429   synthesis (Fig. 7d). MPC-expressing primary hepatocytes also had a higher NADH to NAD$^+$ ratio

430   in both the cytoplasmic and mitochondrial fractions (Fig. 7f). We assessed gluconeogenesis in

431   primary hepatocytes by quantifying glucose in the culture media following incubation with the

432   gluconeogenic precursors, pyruvate, and lactate. Glucose production was higher in MPC-

433   expressing hepatocytes compared with controls (Fig. 7e). Treatment with UK5099 eliminated this

434   effect and reduced glucose production to a similar rate in both cells (Fig. 7e). These results

435   demonstrate that augmented mitochondrial pyruvate in hepatocytes, and related cells in

436   *Drosophila*, drives a metabolic program that results in an increased NADH/NAD$^+$ ratio. This

437   scenario results in accelerated gluconeogenesis, decreased protein synthesis, and educed cell

438   size.

439

Discussion

441   We investigated whether pyruvate metabolism influences biosynthetic capacity and cell

442   size in the *Drosophila* fat body and in HepG2 spheroids. During the third instar phase of

443   *Drosophila* larval growth, when cells are rapidly expanding in size, we observed a profoundly

444   decreased expression of the MPC in liver-like fat body cells. We found that this rewiring of

445   pyruvate metabolism is essential for cell growth as forced maintenance of MPC expression

446   resulted in dramatically smaller cells. By combining *Drosophila* genetic analyses and

447   metabolomics studies in HepG2 cells and spheroids, we demonstrated that excess mitochondrial

448   pyruvate elevates the cellular NADH/NAD$^+$ ratio and redirects carbohydrate metabolism to favor

449   gluconeogenesis over glycolysis (Fig. 7g). This shift reduces the availability of oxaloacetate for

450   aspartate and glutamate biosynthesis, triggering a broader imbalance in amino acid abundances

451   within the cell. We conclude that altering the fate of pyruvate to support biomass accumulation is

452   required for the cell size expansion that occurs during fat body development. We speculate that

453   this phenomenon also applies to the mammalian liver, which is the closest analog of the

454   *Drosophila* fat body, as both HepG2 cells and primary rat hepatocytes show similar effects

455   following ectopic MPC expression.

456   Why does simply reorienting the metabolism of pyruvate have this profound effect on cell

457   growth? Our data suggest that a central mediator of the phenotype is an elevated NADH/NAD$^+$

458   ratio, which likely results from MPC expression driving an acceleration of the TCA cycle, as

459   evidenced by an increase in the abundances of M+2 isotopomers of TCA cycle intermediates.

460 Although the increase in labeled succinate, fumarate, and malate is modest, it occurs despite a
461 reduction in glycolytic labeling. This suggests that less labeled pyruvate feeds the TCA in MPC-
462 expressing cells compared with controls and that we are likely underestimating the actual increase
463 in flux. The TCA cycle generates NADH and appears to do so more actively in cells with
464 ectopically expressed MPC. However, our oxygen consumption data suggest that the oxidative
465 phosphorylation system in these cells does not have the capacity to increase its activity in
466 response to the enhanced availability of mitochondrial pyruvate and an increased $NADH/NAD^+$
467 ratio. As a result, the increased TCA cycle flux and limited ETC activity together elevate the
468 $NADH/NAD^+$ ratio in both the mitochondria and cytoplasm, disrupting cellular redox balance
469 leading to a rewiring of cellular metabolism.

470 This redox situation causes two distinct but related perturbations that appear to both
471 contribute to decreased cell growth. First, we observed a clear depletion of amino acids and
472 evidence of decreased synthesis of amino acids that are primarily derived from TCA cycle
473 intermediates (aspartate, glutamate, and proline). A reduced NAD^+ pool impairs the capacity of
474 cells to synthesize aspartate (Birsoy et al., 2015; Sullivan et al., 2015; Sullivan et al., 2018), which
475 is used to synthesize glutamate and proline and which plays a crucial role in maintaining redox
476 balance in both the mitochondria and cytoplasm (Alkan et al., 2018; Holecek, 2023a; Lieu et al.,
477 2020; Wei et al., 2020; Yoo et al., 2020). Replenishing any of these TCA cycle-derived amino
478 acids via genetic or nutritional increases in their availability was sufficient to reverse the effect of
479 ectopic MPC expression on cell size. Thus, amino acid depletion is a key driver of the small size
480 phenotype. Second, the increased $NADH/NAD^+$ ratio also drives a particular metabolic program
481 that favors the conversion of mitochondrial pyruvate to oxaloacetate and a subsequent increase
482 in gluconeogenesis. This program is enforced by allosteric regulation via NADH, acetyl-CoA, and
483 ATP, which act on PC and several enzymes of glycolysis and gluconeogenesis. It also appears
484 to be important for the small size of MPC-expressing cells since loss of any of several steps along
485 the gluconeogenic pathway, particularly PC and PEPCK2, mitigates or eliminates the cell size
486 phenotype observed with ectopic MPC expression in fat body cells and HepG2 spheroids. It is
487 important to note that gluconeogenesis is a critical function of these cells, and its rate is carefully
488 controlled in response to varying physiological stimuli. Surprisingly, constitutive MPC expression
489 is sufficient to supersede the control enacted by physiological and hormonal signals and enact
490 the loss of biomass and impaired cell size.

491 We have previously shown that loss of the MPC enhanced the stem cell identity and
492 proliferation of intestinal stem cells, whereas ectopic MPC expression had the opposite effect

493   (Bensard et al., 2020; Schell et al., 2017). Such observations are consistent with our findings that

494   MPC expression inversely correlates with biomass accumulation. More recent data demonstrated

495   that enhanced MPC activity prevented the increase in cell size that occurs in cardiomyocytes in

496   response to hypertrophic signaling (Cluntun et al., 2021; Fernandez-Caggiano et al., 2020). In

497   these cases, the fate of mitochondrial pyruvate that determines cell growth is its oxidation in the

498   TCA cycle. In contrast, our studies of hepatocytes and related cells described herein, demonstrate

499   that the fate of pyruvate that suppresses growth in cell size is not oxidation by the TCA cycle, but

500   rather the production of glucose, which starts with its conversion to oxaloacetate by PC in the

501   mitochondria. Cardiomyocytes have low expression of PC compared with liver, where this enzyme

502   (as well as others including PEPCK2) serves a vital role during fasting by producing glucose,

503   which fuels the brain and other organs that require glucose for their survival and function (Hatting

504   et al., 2018; Petersen et al., 2017; Rui, 2014). This is an example of how the unique metabolic

505   physiology of specialized cells plays a critical role in maintaining organismal homeostasis.

506   One conclusion from the data presented herein is that a cell's metabolic program plays a

507   decisive role in determining the growth of that cell. It was striking how rapidly expression of the

508   MPC impacted cell size in the HepG2 model. Essentially, as soon as MPC over-expression

509   became detectable, the population of cells started to show a decrease in size. Notably, the

510   decrease in cell size following ectopic MPC expression occurred despite the upregulation of

511   multiple pro-growth signaling networks. It is unclear why these networks are hyperactivated in this

512   context as there is no evidence from our data indicating any nutrients are in excess abundance.

513   We hypothesize that there may be regulators of cell size that recognize when cells are

514   inappropriately small and engage these pathways to increase cell size. mTORC1, PI3K, and Myc

515   pathways typically promote biomass accumulation and increased cell size but fail to do so when

516   mitochondrial pyruvate is elevated. MPC expression reduced the abundance of amino acids, and

517   this appears to play a dominant role to impair protein synthesis and prevent the cell growth effects

518   expected following hyperactivation of the mTORC1 and Myc pathways. Thus, our data suggest

519   that the metabolic fate of pyruvate can override canonical pathways that mediate cell size—such

520   as mTORC1 signaling.

521   We demonstrate that the appropriate partitioning of pyruvate metabolism maintains the

522   redox state of a cell to support the accumulation of biomass that is necessary for its specialized

523   function. Increased mitochondrial pyruvate metabolism in cells from the fly "liver-like" fat body

524   disrupts these processes, causes cells to perform excess gluconeogenesis, and prevents cell

525   growth. As a result, the *Drosophila* larvae became hyperglycemic and experience developmental

526   delay. The abundances of MPC1 and MPC2 are upregulated in mouse livers during starvation

527   and in high-fat diet conditions, which correlates with increased rates of gluconeogenesis in both

528   circumstances. Conversely, loss of the MPC in liver impairs gluconeogenesis (Gray et al., 2015;

529   McCommis et al., 2015; Yiew & Finck, 2022). Moreover, liver dysfunction in diabetes and hepatic

530   steatosis are driven by reductive stress and an elevated NADH/NAD$^+$ ratio (Goodman et al., 2020;

531   Jokinen & Luukkonen, 2024). We are intrigued by the possibility that the fate of pyruvate might

532   have profound consequences on the redox state and gluconeogenic capacity of the mammalian

533   liver, including by functioning as part of the metabolic milieu that drives unrestrained

534   gluconeogenesis in diabetes. Our discovery that mitochondrial pyruvate regulates the cellular

535   redox state, thereby controlling biosynthesis, offers insights for developing therapeutic strategies

536   for these and other diseases.

537

538   **Methods**

539   ***Drosophila* Strains and Handling**

540   *Drosophila melanogaster* stocks were maintained at 25°C on semi-defined fly food composed of

541   20 g agar, 80 g baker's yeast, 30 g sucrose, 60 g glucose, 0.5 g MgSO4, 0.5 g CaCl2, 11 ml

542   tegosept and 6 ml propionic acid. This was base medium for all *Drosophila* experiments, but

543   specific fly food modifications are mentioned in text and figure legends. To induce clones in fat

544   bodies, synchronized eggs were transferred to 29°C for 4 days until dissection. For experiments

545   involving genetic manipulation of all fat body cells, *tubGal80^{ts20}* was used to restrict activity of *CG-*

546   *Gal4* at 18°C for 120 hours (57 hours equivalent time at 25°C) and larvae were shifted to 29°C till

547   dissection at specified time points.

548   Following fly stocks were procured from Bloomington stock center *UAS-MPC1-P2A-MPC2*

549   (28812582)*, CG-Gal4; tubGal80^{ts20}, hs-Flp1.22 (*BDSC, #77928), *Act>CD2>Gal4, UAS-GFP*

550   (BDSC, #4413), *Act>CD2>Gal4, UAS-RFP* (BDSC, #30558), *UAS-S6K^{STDETE}* (BDSC, #6914),

551   *UAS-Rheb^{PA}* (BDSC, #9689), *UAS-Myc^{OE}* (BDSC, #9675), *UAS-Myc^{RNAi}* (BDSC, #25783), *UAS-*

552   *PI3K93E$^{.Excel}$* (BDSC, #8287), *UAS-PI3K93E^{A2860C}* (BDSC, #8288), *UAS-TSC1^{RNAi}* (BDSC,

553   #31314), *UAS-hPC* (BDSC, #77928), *UAS-PC^{RNAi}* (BDSC, #56883), *UAS-PEPCK2^{RNAi}* (BDSC,

554   #36915), *UAS-FBPase^{RNAi}* (BDSC, #51871), *UAS-Pdk^{RNAi}* (BDSC, #35142), *UAS-NMNAT*

555   (BDSC, #37002), *UAS-CintNDX* (BDSC, #93883), *UAS-ScerNDI1* (BDSC, #93878), *UAS-Slif*

556   (BDSC, #52661), *UAS-GOT2^{RNAi}* (BDSC, #78778). From VDRC *UAS-MPC1$^{RNAi(KK)}$* and from NIG

557   *UAS-Pdha^{RNAi}, UAS-Dlat^{RNAi} (PDH E2)* were purchased.

Generation of Overexpression and CRISPR Mutant fly stock

Pc and *Pepck2* deletion fly stocks were generated using CRISPR-Cas9 as described (Gratz et al., 2014). We targeted specific nucleotide sequences of the genes of interest through homology-directed recombination using two guide RNAs and inserted a dsRed construct that expresses in adult eyes to facilitate the selection of mutant flies. We deleted exon 1 to exon 5 using guide RNAs for *Pc⁻KO*: 5′ guide ATACATTTAAGTCCTAGGC; 3′ guide TCGATTGATCCTGGAAACA. *Pepck2⁻KO*, being a single exon coding sequence, we generated complete deletion by using guides 5′ guide AAAGGGTGCACATCTGTGA; 3′ guide TTTGGGGCGTGGCCTAGAC. The plasmids were injected into y[1] M{GFP[E.3xP3]=vas-Cas9.RFP}ZH-2A w[1118] (BDSC, #55821) fly stock embryos (Bestgene) and one *Pc-KO* and five *Pepck2-KO* flies were picked up, confirmed for the dsRed expression in adult eyes and used in subsequent experiments.

To overexpress *Got2, Got2* cDNA was amplified from RNA extracted from larval fat bodies using primer 5' GAATTC ATGAGTAGAACCATTATTATGACGCTTAAGGAC, 3' CTCGAG CTTGGTAACCTTGTGTATGCTCTCAGCCAGG. The cDNA was then cloned into a pUAST-aatB plasmid using EcoRI and XhoI restriction enzymes, and the construct was injected into pBac{yellow[+]-attp-9A}VK00005 (BDSC, #9725) embryos to obtain the insertion

Mosaic Analysis and Phalloidin Staining for Cell Size Analysis

Fat body clones were induced by the leaky expression of heat shock flippase 1.22 during embryonic stages, and the 2D size of fat body cells was analyzed at 120 hours after egg laying (AEL) using fluorescence microscopy. Cell size analysis was conducted as reported earlier (Toshniwal et al., 2019). Fat bodies were dissected from larvae at the specified time points in 1X PBS buffer (pH 7.2, Invitrogen, #10010049) and fixed in 8% paraformaldehyde (Sigma Aldrich, # P6148) for 1 hour at room temperature (RT). The tissues were then washed twice with 0.1% PBT (0.1% Triton X-100 (Sigma Aldrich, # X100) in 1X PBS buffer) for 10 minutes each. Subsequently, the tissues were incubated with Rhodamine Phalloidin (Thermo Scientific, # R418) at a 1:400 dilution in 1X PBS buffer for 2 hours at room temperature (RT). After staining, the tissues were washed once with 0.1% PBT and then with 1X PBS before being mounted in DAPI-supplemented VectaShield (Vector Labs, #H1200). Representative images were captured using a Laser Scanning Confocal Microscope (LSM 880, Carl Zeiss). For cell size analysis, images were captured with a fluorescence microscope (Carl Zeiss, Axio Vision) at 20X magnification, focusing on a plane where all nuclei were in focus. The 2D areas of fat body cells were measured using FIJI software. Cell membranes stained with Rhodamine Phalloidin were traced using the freehand

590   tool, and the area of approximately 20-25 GFP-positive cells from fat bodies collected from about

591   five animals was measured as one replicate. All cell size analyses were conducted in a blinded

592   manner.

Immunofluorescence on Fat Body Clones

594   Larval fat bodies at 120 hours after egg laying (AEL) at 29°C were dissected in 1X PBS buffer

595   (pH 7.2), fixed in 8% paraformaldehyde for 1 hour at room temperature (RT), and then washed

596   three times in 0.1% PBT (0.1% Triton X-100 in 1X PBS buffer) for 10 minutes each. The tissues

597   were blocked in 10% normal goat serum (NGS, Jackson ImmunoResearch Laboratories, #005-

598   000-121) in 0.1% PBT for 1 hour at RT, followed by incubation with primary antibodies overnight

599   at 4°C. Secondary antibody incubation was performed for 2 hours at RT. Following three to four

600   washes in 0.3% PBT (10 minutes each) at RT, the tissues were mounted in DAPI-supplemented

601   Vectashield (Vector Laboratories, #H1200). Images were captured using a Laser Scanning

602   Confocal Microscope (LSM 880, Carl Zeiss).

Image Acquisition and Analysis

604   For all experiments, confocal images were captured using the same laser power and identical

605   settings, with z-stacks of the dissected tissue taken at 1 μm intervals along the Y-axis. The images

606   were analyzed using Fiji software, where a similar number of z-stacks focusing on the nuclei were

607   projected at mean intensities. Using the freehand tool, cell membranes were outlined, and the

608   mean fluorescence intensity (mean gray value) for each cell was recorded. To account for

609   background fluorescence, the average mean gray values of the background (measured from

610   regions of interest [ROI] of the same size) were subtracted from the recorded mean gray values

611   of the cells. The resulting mean gray values, adjusted for background fluorescence, were then

612   normalized, and the percent normalized mean gray values (with standard deviation, SD) of GFP-

613   negative and GFP-positive cells were plotted.

Measurement of Protein Synthesis in Fat Bodies

615   Protein synthesis in *Drosophila* fat bodies was analyzed using the Click-iT Plus OPP Alexa Fluor

616   594 kit (Molecular Probes, #C10457). Fat bodies were dissected at 120 hours AEL in Shields and

617   Sang M3 Insect Media (SSM3, Sigma, #S8398) and incubated with 5 mM O-propargyl-puromycin

618   (OPP) in SSM3 media for 30 minutes at RT. Tissues were then washed three times with 1X PBS

619   for 10 minutes each and fixed in 8% paraformaldehyde for 1 hour at RT. After fixation, the tissues

620   were washed twice with 0.1% PBT (0.1% Triton X-100 in 1X PBS) supplemented with 0.5% bovine

621   serum albumin (BSA) for 10 minutes each. The OPP was developed for 30 minutes at RT using

622   the Click-iT reaction mixture, which included 88 μl of OPP Reaction Buffer, 20 μl of Copper (III)

623   Sulfate (component D), 2.5 μl of component B, and 100 μl of Buffer Additive (component E),

624   following the manufacturer's instructions. The tissues were then washed twice in Reaction Rinse

625   Buffer for 10 minutes each, followed by two washes in 0.1% PBT supplemented with 0.5% BSA

626   for 10 minutes each at RT. After a final wash in 1X PBS, the fat bodies were mounted in DAPI-

627   supplemented Vectashield. Images were captured using a confocal microscope (LSM 880, Zeiss).

LipidTOX Staining in Larval Fat Body Tissues

629   At 120 hours AEL, 3rd instar larvae were dissected in 1X PBS. The fat bodies were fixed in 8%

630   paraformaldehyde for 1 hour at room temperature. After fixation, tissues were rinsed twice with

631   1X PBS. They were then incubated for 30 minutes in a 1:100 dilution of LipidTOX Red (Invitrogen,

632   #H34351) in PBS, followed by two additional rinses with PBS. The tissues were mounted in DAPI-

633   supplemented Vectashield and imaged using a confocal microscope. To quantify lipid droplet size,

634   the diameters of lipid droplets from 35 fat body clones were measured using FIJI software.

EdU Incorporation in Fat Bodies

636   At 120 hours AEL, fat bodies were dissected in 1X PBS and incubated with 5 μM 5-ethyl-2'-

637   deoxyuridine (EdU) in 1X PBS for 30 minutes at room temperature. The tissues were then washed

638   three times with 1X PBS for 10 minutes each, followed by fixation in 8% paraformaldehyde for 1

639   hour at room temperature. After fixation, the tissues were washed with 0.1% PBT supplemented

640   with 0.5% bovine serum albumin. EdU detection was performed using Click-iT Plus EdU Alexa

641   Fluor 594 (Molecular Probes, #C10639) for 30 minutes at room temperature, according to the

642   manufacturer's instructions. Following development, the fat bodies were mounted in DAPI-

643   supplemented Vectashield. Images were captured using a confocal microscope (LSM 880, Zeiss).

RNA Isolation and RNA Sequencing

645   To collect fat body tissues, w^{1118} flies were mated at 25°C. The following day, flies were starved

646   for one hour, and eggs were collected every 2 hours. The first collection was discarded, and the

647   subsequent two collections were incubated at 25°C. After 20 hours, early hatched 1st instar larvae

648   were discarded, and 1st instar larvae collected over a 2-hour period were kept at 25°C. Fat bodies

649   from 10 male larvae at the specified time points were dissected and preserved in 1X PBS. For

650   RNA isolation from MPC-overexpressing fat bodies at 120 hours AEL, RNA was extracted and

651   purified using the NucleoSpin RNA kit (Takara Bio USA, Inc., #740955.50) with on-column DNA

652   digestion, as per the manufacturer's instructions. Four independent samples for each time point

653   were prepared for sequencing.

654   Library preparation for poly(A)-selected RNAs was carried out using the Illumina RNA TruSeq
655   Stranded mRNA Library Prep Kit with oligo-dT selection. Sequencing was performed using the
656   Illumina NovaSeq Reagent Kit v1.5 (150 bp paired-end reads) at the High-Throughput Genomics
657   Core Facility at the University of Utah. The raw sequencing data were analyzed using the
658   BDGP6.28 genome and gene feature files. Differentially expressed genes were identified using
659   DESeq2 version 1.30.0 with a 5% false discovery rate. RNA quality control, library preparation,
660   and sequencing were performed by the University of Utah Huntsman Cancer Institute High
661   Throughput Genomics and Bioinformatics Shared Resource. RNA-seq data from this study are
662   available at NCBI GEO.

663   **QPCR**
664   500 ng RNA was used to make cDNA using Superscript II reverse transcriptase (Molecular
665   Probes, #18064-022), dNTP (Molecular Probes, #18427-088) and oligodT (Molecular Probes,
666   #18418012). QPCR analyses were performed on cDNA as described using PowerUp SYBR
667   Green Master Mix (Applied Biosystems, #2828831) on QuantStudio 7 Flex (Applied Biosystems)
668   instrument. Fold changes in transcript level were determined using the ΔΔCt method. Transcript
669   levels were normalized to *rp49*. Each experiment was performed using 4–5 independent samples.
670   Following primers were used to do qPCR. List of primers is provided in Appendix 3

671   **Hemolymph Glucose and fat body glucose measurement**
672   Glucose concentrations in larval hemolymph and fat bodies were measured as previously
673   described (Ugrankar-Banerjee et al., 2023). To isolate hemolymph, 10 third instar larvae were
674   selected from culture tubes, thoroughly washed to remove any food residues, and then dried.
675   Hemolymph was collected by bleeding the larvae on a parafilm strip using Dumont 5 forceps (Fine
676   Science Tools, #11254-20). Two microliters of the colorless hemolymph were transferred to a 96-
677   well plate and mixed with 200 µl of Autokit Glucose reagent (Wako, #997-03001). For measuring
678   intercellular glucose, fat bodies were dissected from 10 larvae per genotype and homogenized in
679   approximately 300 microliters of ice-cold 1X PBS using a 29G1/2 syringe. The lysates were
680   inactivated at 70°C for 10 minutes, then centrifuged at maximum speed at 4°C. Thirty microliters
681   of the lysate were mixed with 170 µl of Autokit Glucose reagent. The plates were incubated at
682   37°C for 30 minutes, and absorbance was measured at 600 nm. Glucose concentrations were
683   determined based on the absorbance values recorded for glucose standards.

684   **HepG2 Cells – Knock down and Overexpression Strategies**

685   HepG2 cells were purchased from ATCC and maintained in EMEM supplemented with 10% FBS

686   and 1% PenStrep at 37°C in a 5% CO_2 atmosphere.

687   For inducible overexpression of human MPC1 and MPC2, the HA-MPC2-P2A-T2A-MPC1-FLAG

688   sequence was cloned into the pLVX-TetOne-Zeocin vector. Lentiviral particles were generated

689   using Gag-Pol, pMD2.G, and VSVG packaging plasmids.

690   Viral particles were produced by co-transfecting 293T cells with the respective packaging

691   plasmids using polyethylenimine (PEI, Sigma, #765090) as the transfection reagent at a 3:1 mass

692   ratio of PEI to DNA. The virus-containing medium was collected 48 hours post-transfection,

693   filtered through a 0.45 µm filter, and added to HepG2 cells cultured in normal medium, along with

694   polybrene (Sigma, #P1240000) at a concentration of 10 µg/ml. Transduced cells were selected

695   with 10 µg/ml Zeocin (Gibco, #R25001) for 1 week, and the level of overexpression was assessed

696   by western blotting.

697   For PC over-expression, PC coding sequence was amplified from mRNA isolated from HepG2

698   cells using primers 5' GAATTC ATGCTGAAGTTCCGAACAGTCCATGGG, 3' GGATCC

699   CTCGATCTCCAGGATGAGGTCGTCACC and cloned into pLenti-CMV-Blast. Similarly, SLC1A3

700   cDNA was amplified with primers 5' GGATCC ATGACTAAAAGCAATGGAGAAGAGC, 3'

701   CTACATCTTGGTTTCAATGTCGATGG and GOT2 coding sequence was amplified using

702   primers   5'   GGATCC   ATGGCCCTGCTGCACTCCGG,   3'   TCTAGA

703   CTTGGTGACCTGGTGAATGGCATGG and cloned in pLenti-CMV-Blast (addgene, #17486). The

704   coding sequences of NDI (addgene, #72876) and d2GFP (addgene, #115665) were also cloned

705   into pLenti-CMV-Blast vector. Cells were selected on 3 µg/ml blasticidin (Gibco, A1113903) for 3

706   days.   To   generate   knock   out   cells,   following   gRNAs   were   used.   PCg5e-

707   GAAGCCTATCTCATCGGCCG *CGG,*   PCg6e-   CGAAGTCCGCTCGCTCAGAG *AGG*,

708   PEPCK2g2e-ATCTCCACTAAGCACTCGCA   *GGG*,   PEPCK2g3e-

709   CATGCGTATTATGACCCGAC *TGG*, GOT2ga- GAGTGGCCGGGTAAGCTGAGCAG *AGG*,

710   GOT2gb-GGAGTGGACCCGCTCCGGAACAG *TGG*. The guides were annealed and clones in

711   lentiCRISPRv2 with blasticidin (addgene, #83480) resistance using BsmBI.

712   **HepG2 Cells and 2D Cell Size Analysis**

713   HepG2 cells were cultured on 12 mm coverslips in a 24-well plate at a low density of 10,000 cells

714   per well in Human Plasma-Like Medium (Gibco, #A4899101) supplemented with 10% FBS

715   (Sigma, F0926) and 1% PenStrep (Thermo, #15140). The next day, treatments were initiated as

716   described in the figure legends, including 1 µg/ml doxycycline (Sigma, #D5207), 10 µM UK5099

717　(Sigma, PZ0160-5MG), 10 mM glycine (Sigma, #G7403), 5 mM alanine (Sigma, #A7469), 5 mM

718　asparagine (Sigma, #A4159), 5 mM aspartic acid (Sigma, #A7219), 5 mM glutamic acid (Sigma,

719　#G8415), 5 mM proline (Sigma, #P5607), 5 mM serine (Sigma, #S4311), 10 µM AZD7545

720　(MedChemExpress, #HY-16082), 1 mM dichloroacetate (Sigma, #347795), 100 nM duroquinone

721　(Sigma, #D223204), and 2 nM gramicidin (Sigma, #G5002).

722　For time-course experiments in Figure 3, cells were fixed at 2, 4, 6, 8, 10, 12, 18, and 24 hours

723　after doxycycline treatment using 4% paraformaldehyde in 1X PBS for 20 minutes at RT. For all

724　other experiments, cells were fixed 24 hours after doxycycline treatment. Following fixation, cells

725　were washed once with 0.1% PBT (0.1% Triton X-100 in 1X PBS) for 10 minutes and incubated

726　with Rhodamine Phalloidin at a 1:400 dilution in 1X PBS buffer for 20 minutes at RT. After a

727　couple of washes in 1X PBS, cells were mounted in DAPI-supplemented VectaShield.

728　Images were captured using a fluorescence microscope (Carl Zeiss, Axio Vision) focusing on the

729　plane of the cellular nuclei at 20X magnification, where all nuclei were in focus, and the 2D area

730　of HepG2 cells was measured using FIJI software. All cell size analyses were conducted in a

731　blinded manner.

732　For 3D cell volume analysis, images were captured using a Laser Scanning Confocal Microscope

733　(LSM 880, Carl Zeiss). The red fluorescence signal was used for 3D reconstruction, and cell

734　volume was measured using an ImageJ Macro code in FIJI.

735　**Measurement of Protein Synthesis in HepG2 Cells**

736　HepG2 cells were cultured in either 2D monolayers or spheroid forms. At the desired time point,

737　cells were treated with 20 µg/ml puromycin (Sigma, #P4512) in Human Plasma-Like Medium

738　(HPLM) for 30 minutes at 37°C. Following treatment, cells were washed with 1X PBS, and proteins

739　were extracted using 1X RIPA buffer at 4°C. Protein concentrations were quantified, and 15 µg

740　of total protein was separated by SDS-PAGE using standard methods. Proteins were then

741　transferred onto a nitrocellulose membrane, and puromycin-labeled peptides were detected using

742　an anti-puromycin [3RH11] antibody (Kerafast, #EQ0001) followed by incubation with an

743　appropriate secondary antibody.

744　Protein synthesis in HepG2 cells was also analyzed using the Click-iT HPG Alexa Fluor 594 kit

745　(Molecular Probes, #C10429). HepG2 cells were grown on 12 mm coverslips at a density of

746　10,000 cells per well and treated with 1 µg/ml doxycycline for 24 hours. Cells were then incubated

747　with 50 µM L-homopropargylglycine (HPG) in methionine-free DMEM (Gibco, #21013024) for 30

748   minutes at 37°C. After incubation, cells were washed twice with 1X PBS for 2 minutes each and

749   fixed in 4% paraformaldehyde for 20 minutes at room temperature.

750   For OPP staining, appropriately fixed cells were washed twice with 0.1% PBT (0.1% Triton X-100

751   in 1X PBS) supplemented with 0.5% bovine serum albumin (BSA) for 10 minutes each. HPG was

752   detected using the Click-iT reaction mixture, which included 88 µl of OPP Reaction Buffer, 20 µl

753   of copper solution (component D), 2.5 µl of component B, and 100 µl of Buffer Additive

754   (component E), following the manufacturer's instructions. Cells were washed twice in Reaction

755   Rinse Buffer for 10 minutes each, followed by two washes in 0.1% PBT supplemented with 0.5%

756   BSA for 10 minutes each at room temperature. After a final wash in 1X PBS, the coverslips were

757   mounted in DAPI-supplemented Vectashield. Images of the cells were captured using a confocal

758   microscope (LSM 880, Zeiss).

759   **Analysis of Spheroids**

760   HepG2 cells were cultured in ultra-low attachment 96-well plates (Costar, #7007) at a density of

761   10,000 cells per well in Human Plasma-Like Medium (HPLM) supplemented with 10% FBS and

762   1% penicillin-streptomycin. Treatments were applied as specified in the figure legends, including

763   1 µg/ml doxycycline, 5 mM aspartate, 5 mM glutamate, 10 µM UK5099, MEM non-essential amino

764   acids (Gibco, #11140050), 100 nM nicotinamide riboside (Sigma, #SMB00907), and 10 µM NMN

765   (Sigma, #N3501). Cells were incubated for 6 days at 37°C with CO_2 and O_2. Brightfield images

766   of the spheroids were captured using a Zeiss Axio Observer Z1 microscope, and spheroid size

767   was measured using FIJI software.

768   To quantify cell numbers, 12 spheroids from each condition (EV or MPC+) were pooled,

769   dissociated by trypsinization, and the number of cells was counted using a CellQuant system (Bio-

770   Rad).

771   For cell cycle analysis, cells were stained using Vybrant® DyeCycle™ Violet stain (Molecular

772   Probes, #V35003). After pooling and dissociating 12 spheroids from each condition (EV or

773   MPC+), cells were centrifuged and resuspended in 200 µL of 5 µM Vybrant® DyeCycle™ Violet

774   stain in EMEM supplemented with 10% FBS. The staining was performed by incubating the cells

775   at 37°C for 30 minutes, protected from light. Samples were analyzed using a BD Celesta flow

776   cytometer with ~405 nm excitation and ~440 nm emission. The resulting FCS files were

777   processed in FlowJo software, where the forward scatter of singlets was recorded, and median

778   data were used to plot graphs. Vybrant dye staining was employed to assess the distribution of

779   cells in the G1, S, and G2/M phases.

780 For apoptosis detection, an Annexin V/PI staining kit (Molecular Probes, #V13241) was used, with

781 5 μM camptothecin (MedChemExpress, #HY-16560) serving as a positive control. Sixteen

782 spheroids were collected, dissociated with trypsin as described above, and resuspended in 200

783 μL of 1X annexin-binding buffer. Cells were incubated with 1 μl of Alexa Fluor™ 488 Annexin V

784 (Component A) and 0.2 μl of 100 μg/ml PI working solution at room temperature for 15 minutes.

785 Stained cells were then analyzed using a BD Canto flow cytometer, measuring fluorescence

786 emission at 530 nm and 575 nm (or equivalent) with 488-nm excitation.

787 **Biomolecule Separation and Measurement**

788 For this experiment, biomolecules were extracted and measured from both *Drosophila* larvae fat

789 bodies and HepG2 cell spheroids. Fat bodies were dissected from 10 male larvae at 120 hours

790 after egg laying (AEL) and collected in 150 μl of 1X PBS. The samples were lysed by performing

791 three freeze-thaw cycles. A total of 24 spheroids were homogenized in 150 μl of

792 radioimmunoprecipitation assay (RIPA) buffer (50 mM Tris-HCl, 1% NP-40, 0.5% sodium

793 deoxycholate, 0.1% SDS, 150 mM NaCl, and 2 mM EDTA).

794 Lysates were centrifuged at 7500 × g for 5 minutes to remove debris. The resulting supernatant

795 was used for the following measurements. Triglyceride Measurement- For triglyceride analysis,

796 30 μL of the supernatant was incubated for 10 minutes at 75°C. Following this, 10 μl of

797 homogenate from the spheroids or 2 μL from fat bodies was added to 200 μl of Triglycerides

798 Reagent (Thermo Fisher Scientific, #TR22421). The mixture was incubated for 10 minutes at

799 37°C in 96-well microplates with gentle shaking. Absorbance was measured at 550 nm using the

800 Synergy Neo2 multimode plate reader (BioTek).

801 Protein Measurement- Protein concentrations were determined by mixing 2 μl of the supernatant

802 with 200 μl of BCA Protein Assay Reagent (Thermo Scientific, #23225). The mixture was

803 incubated for 30 minutes at 37°C with gentle shaking in 96-well microplates. Absorbance was

804 measured at 560 nm.

805 RNA and DNA Separation- The remaining 100 μl of the supernatant was processed for RNA and

806 DNA separation using TRIzol reagent (1 ml; Invitrogen, # 15596026). To separate RNA, 0.2 ml of

807 chloroform was added to the sample, followed by centrifugation at 12,000 × g for 15 minutes at

808 4°C. The RNA in the interphase was purified using 75% ethanol, following standard methods, and

809 quantified using a NanoDrop spectrophotometer. DNA was extracted from the organic phase by

810 adding 100% ethanol, followed by isopropanol precipitation. The resulting pellets were washed

811 with 0.3 M guanidine hydrochloride in 95% ethanol, resuspended in 0.1 M sodium citrate in 10%

812   ethanol (pH 8.5), and washed with 75% ethanol. Finally, the DNA pellets were resuspended in

813   0.1 ml of 8 mM NaOH by pipetting. The pH was adjusted to 7.2 with HEPES, and the DNA was

814   quantified using a NanoDrop spectrophotometer.

815   **Measurement Of NADH/NAD+ Protocol**

816   For HepG2 cells, 1×10^6 cells treated with 1ug/ml dox for 24 hours were scraped in 1.5 ml tube.

817   For NADH/NAD+ ratio analysis from spheroids, 18 spheroids were treated with 1ug/ml dox for 6

818   days were resuspended in 1mL 1XPBS. Scraped cells or pooled spheroids were centrifuged

819   (13,500xg, 10 s, 4°C) and tresuspended in 250 ul lysis buffer. Fat bodies from male 10 larvae

820   were dissected in 1X PBS and resuspended in lysis buffer provided with kit. To separate

821   cytoplasmic and mitochondrial fractions by rapid subcellular fractionation, lysates were

822   centrifuged (13,500xg, 10 s, 4°C) and the supernatant was collected for the cytosolic fraction,

823   while the remaining pellet contained the mitochondria. Mitochondrial pellet was resuspended in

824   100 ul lysis buffer.

825   NADH to NAD+ ratios were measured using Amplite Fluorimetric NAD+/NADH ratio assay kit (AAT

826   Bioquest, #15263) as directed by instructions provided. Briefly, 25uL of cytoplasmic or

827   mitochondrial fractions were mixed with either NADH or NAD+ extraction solution. Samples were

828   incubated at 37°C for 15 minutes. Later 25ul of either NAD+ or NADH extraction was added which

829   was followed by incubation with 75ul mix of NADH sensor buffer and NAD+/NADH recycling

830   enzyme for 1 hour at RT. Fluorescence intensity was recoded at 540 nm excitation and 590 nm

831   emission.

832   **Protein Extraction and Western Blotting**

833   HepG2 cells were directly scraped into RIPA supplemented with protease and phosphatase

834   inhibitors (Roche Molecular, #04906845001). For spheroids, 18 spheroids were pooled, washed

835   with 1X PBS, and then incubated in RIPA buffer with the protease and phosphatase inhibitor

836   cocktail. After 45 minutes on ice with vertexing every 15 minutes, lysates were centrifuged at

837   16,000xg for 15 minutes at 4°C to remove insoluble material.

838   Protein concentration was measured using the Bicinchoninic Acid (BCA) protein assay (Thermo

839   Fisher Scientific, 23225). Samples were mixed with 4x sample loading buffer and heated at 95°C

840   for 5 minutes. Protein samples (15 μg) were separated on SDS-polyacrylamide gel

841   electrophoresis (SDS-PAGE) at 20 mA per gel, transferred onto a 0.45 μm nitrocellulose

842   membrane (GE Healthcare) using the Mini Trans-Blot module (Bio-Rad) at 120 V for

843   approximately 2 hours.

844   The membrane was blocked with 5% non-fat milk (Serva) in Tris-buffered saline with 0.05%

845   Tween 20 (TBS-T) for 1 hour. It was then incubated overnight with primary antibodies diluted in

846   TBS-T. The next day, the membrane was washed with TBS-T and incubated with fluorophore-

847   conjugated secondary antibodies in TBS-T for 1 hour. Following additional washes with TBS-T,

848   fluorescence was detected using the Odyssey CLx imaging system (LI-COR Biosciences) and

849   analyzed using FIJI software. Antibodies used are listed in Appendix 1.

850   **Steady-State Metabolomic Studies**

851   10 million HepG2 cells with MPC+ and EV control expression were grown in 2D culture were

852   treated with 1ug/ml dox in HPLM supplemented with 10% HPLM. After 24 hours, culture medium

853   was collected and quenched with 1:4 volume of 100% methanol. Cells were washed and

854   quenched with 1 ml of 80% methanol in water. Cell lysates were then subjected to three rapid

855   freeze-thaw cycles and then spun at 16,000xg for 10 min at 4°C. The supernatants were

856   evaporated using a SpeedVac concentrator. Each sample or treatment were with 4 to 5 replicates.

857   **^{13}C-glucose tracing for M+3 vs M+2 ratio of TCA cycle metabolism**

858   10 million HepG2 cells with MPC+ and EV control expression were grown in 2D culture and were

859   treated with 1ug/ml dox in HPLM. After 24 hours, culture medium was changed to ^{13}C-glucose

860   tracing media: glucose-free HPLM supplemented with 4.5g/L ^{13}C glucose and 10% dialyzed FBS.

861   0 hour, 1 hour, 2 hours, and 4 hours later, cells were washed and quenched with 1 ml of 80%

862   methanol in water. Cells were scrapped out in Methanol and lysates were then subjected to three

863   rapid freeze-thaw cycles and then spun at 16,000xg for 10 min at 4°C. The supernatants were

864   evaporated using a SpeedVac concentrator.

865   **^{13}C-Lactate Tracing for Gluconeogenesis Assay**

866   10 million HepG2 cells with MPC+ and EV control expression were grown in 2D culture were

867   treated with 1ug/ml dox in DMEM without glucose, without glutamine (Gibco, #A1443001) with

868   10% dialyzed FBS. After 16 hours, culture medium was replaced with 6 ml of 1ug/ml dox in DMEM

869   without glucose, without glutamine and without FBS. 3 hours later, culture medium was replaced

870   with 6 ml of 1ug/ml dox and 20mM lactate (Sigma, #490040) containing DMEM without glucose

871   or glutamine or FBS. After 4 hours, 300 µl culture medium was collected and quenched with 1:4

872   volume of 100% methanol. Cells were washed and quenched with 1 ml of 80% methanol in water.

873   Cell lysates were then subjected to three rapid freeze-thaw cycles and then spun at 16,000xg for

874   10 min at 4°C. The supernatants were evaporated using a SpeedVac concentrator. Each cell

875   types had 4 to 5 replicates.

Gas Chromatography-Mass Spectrometry Derivatization

Dried metabolites were derivatized and prepared for Gas chromatography following standard methods. Dried samples were resuspended in 30 µl of anhydrous pyridine with methoxamine hydrochloride (10 mg/ml) and incubated at RT overnight. Next day, the samples were heated at 70°C for 15 min and centrifuged at 16,000*g* for 10 min. The supernatant was transferred to a pre-prepared gas chromatography–mass spectrometry autoinjector vial with 70 µl of *N*-(*tert*-butyldimethylsilyl)-*N*-methyltrifluoroacetamide (MTBSTFA) derivatization reagent. The samples were incubated at 70°C for 1 hour, after which aliquots of 1 µl were injected for analysis. Samples were analyzed using either an Agilent 6890 or 7890 gas chromatograph coupled to an Agilent 5973N or 5975C Mass Selective Detector, respectively. The observed distributions of mass isotopologues of glucose, pyruvate, citrate, succinate, aspartate, glutamate, malate, fumarate, phosphoenolpyruvate were corrected for natural abundance.

Liquid chromatography-mass spectrometry

Following standard methods, dried metabolites were resuspended in 100 µl of 0.03% formic acid in analytical-grade water, vortexed, and centrifuged to remove insoluble material. 20 µl of supernatant was collected and injected to AB SCIEX QTRAP 5500 liquid chromatography/triple quadrupole mass spectrometer (Applied Biosystems SCIEX). Chromatogram review and peak area integration were performed using MultiQuant (version 2.1, Applied Biosystems SCIEX). The peak area for acetyl CoA, ADP, ATP, NAD^+, NADH was normalized against the total ion count of that sample.

Oxygen consumption rate

Oxygen consumption rates (OCR) were measured using an XFe96 Extracellular Flux Analyzer (Agilent) according to the manufacturer's instructions. Cells were plated at a density of 60,000 cells per well in Seahorse microplates (Agilent) and allowed to adhere for 6 hours. MPC was induced with 1 µg/ml doxycycline overnight. Afterward, the cell culture media was removed and replaced with Seahorse assay media, which consisted of DMEM supplemented with 4 mM glutamine. OCR was assessed under basal conditions and following sequential injections of 1 mM glucose, oligomycin (2 µM), FCCP (0.5 µM), and a mix of rotenone plus antimycin A (2 µM each). Immediately after the measurements, cells were lysed in RIPA buffer, and the protein concentration was used to normalize the OCR data.

Primary Hepatocyte Cultures and Analysis

907   Rat primary hepatocytes (Lonza, #RWCP01) were thawed and plated in a 24-well plate at a

908   density of 0.16 million cells per well in Hepatocyte Plating Medium (Lonza, #MP100). Four hours

909   post-plating, the medium was replaced with Hepatocyte Basal Medium (HBM) supplemented with

910   BCM SingleQuots (Lonza, #CC-4182), including Bovine Pituitary Extract (BPE), Insulin,

911   Hydrocortisone, Gentamicin/Amphotericin-B (GA), Transferrin, and human Epidermal Growth

912   Factor (hEGF).

913   Twenty-four hours after plating, the hepatocytes were transfected with 1 µg of either pT3.GFP or

914   pT3.MPC2Flag-P2AT2A-MPC1HA using Lipofectamine 3000 (Invitrogen, #L3000001). Forty-

915   eight hours post-transfection, cells were lysed in 1X RIPA buffer, and Western blot analysis was

916   performed to confirm the overexpression of MPC1 and MPC2.

917   Forty-eight hours post-transfection, hepatocytes were fixed in 4% paraformaldehyde in 1X PBS.

918   Following several washes with 0.1% PBT, cells were incubated in 5% BSA and stained with anti-

919   MPC1 antibody overnight at 4°C. MPC1 was detected using a secondary anti-rabbit Alexa Fluor

920   antibody. Cells were also stained with Phalloidin Red. Coverslips were mounted in DAPI-

921   supplemented Vectashield, and images were captured using an LSM 880 confocal microscope.

922   Cell area marked by Phalloidin Red was quantified using differential interference contrast filter

923   and analyzed with FIJI software.

924   For protein synthesis measurement, hepatocytes were incubated with 20 µg/ml puromycin for 30

925   minutes. Puromycin-tagged peptides were visualized by immunostaining with rabbit anti-

926   puromycin antibody (1:500) and mouse anti-Flag M2 antibody (1:1000, Sigma, F1800), followed

927   by the appropriate secondary antibodies. Images were captured with the LSM 880 confocal

928   microscope. Puromycin intensity was measured using FIJI, and the percent change in puromycin

929   intensity in Flag-positive cells was compared to Flag-negative cells.

930   Gluconeogenesis was assessed using lactate and pyruvate as substrates. Forty-eight hours post-

931   transfection, hepatocytes were incubated in low-glucose DMEM with 1 mM sodium pyruvate and

932   4 mM glutamine without FBS. After 16 hours, hepatocytes were treated with 200 ng glucagon in

933   no-glucose DMEM without FBS for 3 hours. Cells were then cultured in media with 20 mM lactate

934   and 2 mM pyruvate, with and without 10 µM UK5099, for 2 and 4 hours. Glucose levels in the

935   media were measured using the Amplex Red Glucose Assay Kit (Invitrogen, #A22189) according

936   to the manufacturer's instructions. Glucose production per cell per hour was plotted on a graph.

937   The compartmentalized NADH to NAD$^+$ ratio in hepatocytes was quantified 48 hours post-

938   transfection using the Amplite Fluorimetric NAD$^+$/NADH Ratio Assay Kit as described previously.

939

Figure Legends

Figure 1: Increased mitochondrial pyruvate transport reduces size of *Drosophila* fat body cells.

a-b. a) A schematic representation of *Drosophila* developmental stages with specified time points (hours after egg laying (AEL) at 25°C) at which larvae were dissected to collect fat bodies. **b)** Representative images of larval fat bodies at the indicated times (hours AEL) stained with rhodamine phalloidin to visualize cell membranes and DAPI to visualize DNA. The scale bar represents 25 µm.

c. Quantification of fat body cell area based on rhodamine phalloidin stained cell membranes at the indicated time points. Data are presented as mean ± standard deviation (s.d.) from six biological replicates, with each replicate averaging the size of 50 randomly selected cells from fat bodies dissected from five male larvae.

d-e. d) A schematic of pyruvate metabolism. In the cytoplasm, pyruvate is a product of glycolysis, synthesized by Pyruvate Kinase (Pyk) or from lactate via Lactate Dehydrogenase (LDH). Pyruvate is transported into mitochondria by the Mitochondrial Pyruvate Carrier (MPC) complex. Within mitochondria, pyruvate is converted into acetyl-CoA by Pyruvate Dehydrogenase (PDH) or into oxaloacetate by Pyruvate Carboxylase (PC), both of which are substrates for the TCA cycle. PEPCK2 converts oxaloacetate into phosphoenolpyruvate. **e)** *Pyk*, *Mpc1*, *Mpc2, Pdha* and *Dlat* transcripts were quantified from larval fat bodies collected at the indicated times.

f-g. f) Representative confocal microscope images of phalloidin- and DAPI-stained fat bodies with flip-out Gal4 clones expressing MPC1-P2A-MPC2 (MPC+), marked with GFP at 120 hours AEL. The images at the bottom show magnified insets of GFP-positive cells in control and MPC expressing clones. **g)** Quantification of GFP-positive clonal cell area with the indicated genetic manipulations- control, MPC+ and *Mpc1*-KD. Data are presented as mean ± s.d. from six biological replicates, with each set averaging the size of 20 clonal cells from fat bodies collected from five male larvae.

h-i. h) Images showing control and MPC+ clones from larvae fed on no sugar diet. **I)** Quantification of the area of control, MPC+ and *Mpc1*-KD fat body clonal cells from larvae fed on a diet containing either 9% sugar or no sugar.

j. Quantification of the area of MPC+ fat body clonal cells from larvae fed a diet supplemented with or without 20 µM UK5099.

972 **k.** Fold change of the abundances of the indicated macromolecules in fat bodies expressing MPC

973 (MPC+) in all fat body cells using CG-Gal4. The abundance of each individual macromolecule is

974 normalized to that of the respective macromolecular abundance in GFP expressing, control fat

975 bodies. Data are represented as mean ± s.d. from three biological replicates with fat bodies

976 collected from 10 larvae at 120 hours AEL.

977 **l-m. l**) Representative images of fat body clones stained with O-propargyl-puromycin (OPP, 20

978 µM for 30 minutes), showing control and MPC expressing GFP-positive cells. The top panels

979 show GFP-positive clones and OPP staining in red, while the bottom panels show respective OPP

980 channel. Arrows indicate cells with the specified genetic manipulation. The scale bar represents

981 20 µm. **M)** Quantification of OPP fluorescence intensity of control or MPC+ fat body cells

982 compared to neighboring non clonal cell. Data are presented as mean ± s.d. from six biological

983 replicates, with each set averaging the size of 20 clonal cells from fat bodies collected from five

984 male larvae.

985 Unpaired t-tests or one-way ANOVA tests were performed to evaluate the statistical significance

986 of the data, with p-values mentioned in the graphs where significance was noted.

987

988 **Supplementary Figure 1: Transcriptomic changes in fat body during larval development**

989 **(related to Main Figure 1).**

990 **a.** A heatmap displaying changes in mRNA abundance of genes encoding mitochondrial proteins

991 and enzymes involved in various metabolic pathways in wild type- w^{1118} fat bodies collected at the

992 specified time points. Right. Clustered hallmarks are indicated by a color gradient corresponding

993 to relative gene expression levels.

994 **b.** A heatmap illustrating transcriptomic changes in signaling pathways in w^{1118} fat body cells

995 during *Drosophila* larval development.

996 **c**. Quantification of *Pepck* and *Pepck2* transcripts from larval fat bodies collected at the indicated

997 times.

998

999 **Supplementary Figure 2 – Increased mitochondrial pyruvate transport reduces size of**

1000 ***Drosophila* fat body cells. (Related to Main Figure 1)**

1001 **a.** Schematic representation of experimental time course using temperature-sensitive Gal80^{ts20} to

1002 control Gal4 expression. At 18°C, Gal80^{ts20} is active, inhibiting Gal4 expression; at 29°C, Gal80^{ts20}

1003 is inactive, allowing Gal4 expression. The temperature switch occurs towards the end of the 2nd

1004   instar stage so that MPC expression construct is induced temporally only during the 3rd instar

1005   stage. Fat bodies were collected at the specified time points.

1006   **b.** Quantification of *Mpc1* and *Mpc2* transcripts from fat bodies of CG-Gal4>MPC+ versus CG-

1007   Gal4>GFP or control larvae, dissected at the indicated times after the induction of Gal4 activity.

1008   **c.** Quantification of fat body cell area in MPC+ (CG-Gal4>MPC+) versus control (CG-Gal4>GFP)

1009   larvae at the indicated times after Gal4 induction. Data are presented as mean ± s.d. from six

1010   biological replicates, with each replicate representing the average size from 50 randomly selected

1011   cells from fat bodies dissected from five male larvae.

1012   **d.** Schematics illustrating the use of the Ay-Gal4 cassette to generate clones with MPC

1013   expression. Clones are generated by leaky expression of hs-flp1.22-flippase, which binds to

1014   specific FRT sites in chromatin, leading to the excision of the spacer *'yellow'* gene and positioning

1015   of the *actin5C* promoter next to the Gal4 coding sequence. This is followed by Gal4 expression in

1016   the cell and subsequent expression of UAS-GFP or UAS-MPC1-P2A-MPC2 constructs. Due to

1017   the leaky and random expression of the flippase, GFP-marked mosaicism occurs in only 1-5% of

1018   fat body cells.

1019   **e-f.** Representative images of fat bodies with MPC expression and control clones, showing

1020   increased abundance of (**e**) MPC1 and (**f**) MPC2 proteins. Arrows indicate cells with the specified

1021   genetic manipulation. The scale bar represents 20 µm.

1022   **g.** Representative images of fat bodies with MPC+ and control clones dissected from larvae fed

1023   on a diet supplemented with 20 µM UK5099. Arrows indicate cells with the specified genetic

1024   manipulation. The scale bar represents 20 µm.

1025   **h-k.** The abundances of (**h**) DNA, (**i**) RNA, (**j**) triacylglycerides (TAGs), and (**k**) protein in fat bodies

1026   where MPC is expressed in all fat body cells using CG-Gal4 driver. The abundance of each

1027   individual macromolecule is normalized to that of the control. Data are represented as mean ±

1028   s.d. from three biological replicates with fat bodies collected from ten larvae at 120 hours AEL.

1029   **l-n. l)** Representative images of MPC+ and control fat body clones showing lipid droplets stained

1030   with LipidTox in red. The area in square is presented in high-magnification insets below to show

1031   lipid distribution in the clonal cells. The scale bar represents 25 µm. **m)** Quantification of lipid

1032   droplets relative to cell size in MPC+ versus control cells. **n)** The data are presented as the

1033   number of lipid droplets per cell area and the fraction of cell area covered by lipid droplets.

1034   **o-p. o)** Representative EdU-stained confocal images of MPC+ and control fat body cells, showing

1035   replicating DNA. Arrows indicate cells with the specified genetic manipulation. The scale bar

1036   represents 20 µm. **p)** Quantification of total EdU fluorescence intensity in GFP-positive cells

1037   compared to neighboring GFP-negative cells in MPC+ versus control clones. Data are presented

1038   as mean ± s.d.

1039   Unpaired t-tests were performed to evaluate the statistical significance of the data, with p-values

1040   noted in the graph if significance was observed.

1041

1042   **Figure 2: mTORC1 and Myc pathways are hyperactivated in MPC overexpressing fat body**

1043   **cells.**

1044   **a**. Schematic of the mTORC1 pathway. The mTORC1 pathway is activated by pro-growth signals

1045   such as insulin, leading to the phosphorylation of S6 kinase (S6K) and 4EBP. S6K phosphorylates

1046   ribosomal protein S6, while 4EBP phosphorylation inactivates 4EBP and releases elongation

1047   factor eIF4E. These events increase ribosomal assembly and elongation rates, thereby enhancing

1048   protein synthesis.

1049   **b-c**. **b)** Representative images of fat body clones with *S6k* over-expression, control clones, and

1050   MPC+ clones, stained for phosphorylated S6 (p-S6) in red (top panels) and white (bottom panels).

1051   Arrows indicate clonal cells with the specified genetic manipulation. The scale bar represents 20

1052   µm. **c)** Quantification of total p-S6 fluorescence intensity in GFP-positive cells compared to

1053   neighboring GFP-negative cells in MPC+ versus control clones. Data are presented as mean ±

1054   s.d. with statistical significance as scored with One-way Annova test.

1055   **d-e**. **d)** Representative images of fat body clones with *Rheb* over-expression, control clones, and

1056   MPC+ clones stained for phosphorylated 4EBP (p-4EBP) in red (top panels) and white (bottom

1057   panels). Arrows indicate clonal cells with the specified genetic manipulation. The scale bar

1058   represents 20 µm. **e)** Quantification of total p-4EBP fluorescence intensity in MPC+ versus control

1059   clones with statistical significance as scored with One-way Annova test.

1060   **f-g. f**) Representative images of fat body clones with *Myc* knockdown, control clones, and MPC+

1061   clones stained for Myc protein in red (top panels) and white (bottom panels). Arrows indicate

1062   clonal cells with the specified genetic manipulation. The scale bar represents 20 µm. **g)**

1063   Quantification of total Myc fluorescence intensity in MPC+ versus control clones with statistical

1064   significance as scored with One-way ANOVA test.

1065   **h-i**. **h)** Representative images of fat body clones from starved wild type, control clones, and MPC+

1066   clones, stained for phosphorylated eIF2α (p-eIF2α) in red (top panels) and white (bottom panels).

1067   Arrows indicate clonal cells with the specified genetic manipulation. The scale bar represents 20

1068   µm. **i)** Quantification of total p-eIF2α fluorescence intensity in MPC+ versus control clones with

1069   statistical significance as scored with One-way ANOVA test. Data are presented as mean ± s.d.

1070   One-way ANOVA tests were performed to evaluate the statistical significance of the data, with p-

1071   values noted in the graph if significance was observed.

1072

1073   **Supplementary Figure 3: mTORC1 and Myc pathways are hyperactivated in MPC**

1074   **overexpressing fat body cells. (Related to Main Figure 2)**

1075   **a**. Representative images of fat body clones with PI3K-DN (dominant-negative) expression,

1076   control clones, and MPC+ clones stained for dFoxo in red (top panels) and white (bottom panels).

1077   Arrows indicate clonal cells with the specified genetic manipulations. The scale bar represents 20

1078   μm.

1079   **b**. Transcriptomic analysis of MPC+ fat bodies compared to control, represented as Hallmarks

1080   from GSEA (Gene Set Enrichment Analysis).

1081   **c-d**. Quantification of the area of MPC+ cells with or without *PI3K* over-expression **(c),** and with

1082   or without *Tsc1* knock down **(d).** Data are presented as mean ± s.d. from five biological replicates,

1083   where each data point represents the average size of 20 clones from fat bodies collected from

1084   five male larvae.

1085   **e-f**. Quantification of cell area in MPC+ clones with *Myc* over-expression **(e)** or *Myc* knockdown

1086   **(f).** Data are presented as mean ± s.d. from five biological replicates, where each data point

1087   represents the average size of 20 clones from fat bodies collected from five male larvae.

1088

1089   **Figure 3: Increased mitochondrial pyruvate transport reduces size of HepG2 spheroids.**

1090   **a.** Western blots showing inducible expression of MPC1 and MPC2 at 2-hour intervals following

1091   treatment with 1 μg/ml doxycycline. Citrate synthase and tubulin were used as loading controls.

1092   Both endogenous and epitope tag bands are shown.

1093   **b.** Quantification of the 2D area of HepG2 cells with MPC expression (MPC+) or empty vector

1094   (EV) fixed and stained with rhodamine phalloidin at the indicated times after doxycycline

1095   treatment. Data are presented as mean ± s.d. from five biological replicates, with each replicate

1096   representing the average size of 25 randomly selected cells.

1097   **c.** Quantification of the 2D area of MPC+ or EV HepG2 cells treated with 10 μM UK5099. Data

1098   are presented as mean ± s.d. from five biological replicates, with each replicate representing the

1099   average size of 25 randomly selected cells.

1100   **d-e. d)** Representative brightfield images of HepG2 spheroids with empty vector (EV) or MPC

1101   expression (MPC+) treated with 1 μg/ml doxycycline for six days. The scale bar represents 200

1102 µm. **e)** Quantification of spheroid area from images of MPC+ or EV HepG2 spheroids, with or

1103 without doxycycline treatment. Data are presented as mean ± s.d. from 30 technical replicates.

1104 **f-g. f)** Forward scatter (FSC) of cells dissociated from MPC+ (red) or EV spheroids with cell count

1105 normalized to mode. **g)** Median FSC of MPC+ HepG2 spheroids treated with or without 1 µg/ml

1106 doxycycline. Data are presented as mean ± s.d. from three biological replicates.

1107 **h.** Fold change in macromolecules—DNA, TAGs, RNA, and protein—fractionated from EV or

1108 MPC+ HepG2 spheroids normalized to that in EV HepG2 cells.

1109 **i-j. i)** Representative images showing L-Homopropargylglycine (HPG)-labeled newly synthesized

1110 proteins in EV or MPC+ HepG2 cells. The top panels show HPG staining, and the lower panels

1111 show nuclei stained with DAPI. The scale bar represents 20 µm. **j)** Quantification of HPG

1112 fluorescence intensity is presented as mean ± s.d. from 35 cells, for both EV and MPC+ cells.

1113 **k-l. k)** Western blot analysis of nascent protein synthesis using a puromycin incorporation assay

1114 (20 µg/ml puromycin for 30 minutes) in either EV or MPC+ HepG2 spheroids (protein lysates from

1115 16 spheroids loaded in each lane). **l)** Quantification of 70 kD band intensity in puromycin blot

1116 normalized with tubulin band intensity and represented as mean ± s.d. from three independent

1117 experiments.

1118 **m.** Relative accumulation of destabilized GFP (d2GFP) in EV or MPC+ HepG2 spheroids treated

1119 with or without 1 µg/ml doxycycline ± 10 µM UK5099. Data are presented as mean ± s.d. from

1120 three biological replicates.

1121 Unpaired t-tests, one-way, or two-way ANOVA tests were performed to evaluate the statistical

1122 significance of the data, with p-values noted in the graph if significance was observed.

1123

1124 **Supplementary Figure 4: MPC overexpression reduces size of HepG2 cells in 2D and**

1125 **spheroid culture (Related to Main Figure 3).**

1126 **a**. Quantification of cell volume from confocal images of HepG2 cells expressing MPC (MPC+) or

1127 an empty vector (EV). Data is presented as mean ± s.d. from 22 EV cells and 25 MPC+ cells.

1128 **b**. Quantification of the number of cells per spheroid in EV or MPC+ HepG2 cells with or without

1129 doxycycline treatment. Data is presented as mean ± s.d. from 18 technical replicates.

1130 **c**. Cell cycle profiles of MPC+ HepG2 spheroids treated with or without doxycycline treatment.

1131 Data is presented as mean ± s.d. from three biological replicates.

1132 **d**. Annexin/Propidium Iodide (PI) analysis of MPC+ HepG2 cells cultured with or without

1133 doxycycline. Data is presented as mean ± s.d. from three biological replicates.

1134 **e-h**. Concentrations of **(e)** DNA, **(f)** RNA, **(f)** triacylglcyerides (TAGs) and **(g)** protein measured

1135 for 18 MPC+ and 18 EV HepG2 cells. Data is shown as mean ± s.d. from three biological

1136 replicates.

1137 Unpaired t-tests and one-way ANOVA tests were performed to evaluate the statistical significance

1138 of the data, with p-values mentioned in the graph if significance is noted.

1139

1140 **Figure 4: Increased mitochondrial pyruvate metabolism promotes gluconeogenesis via**

1141 **Pyruvate Carboxylase to suppress protein synthesis.**

1142 **a.** Schematic illustration of the ^{13}C-glucose tracing strategy used to measure the activity of

1143 Pyruvate Dehydrogenase (PDH) and Pyruvate Carboxylase (PC). TCA metabolites labeled with

1144 two heavy carbons (^{13}C or M+2 TCA pool) result from PDH activity, whereas M+3 TCA metabolites

1145 result from PC activity. PDH is inhibited by PDK-mediated phosphorylation. DCA and AZD7545

1146 are inhibitors of PDK.

1147 **b.** Fractional enrichment of M+2 succinate in empty vector (EV; red) and MPC expressing (MPC+;

1148 blue) HepG2 cells at the indicated times after ^{13}C-glucose tracing. MPC expression was induced

1149 for 24 hours by treatment with 1 μg/ml doxycycline and media was changed to ^{12}C-glucose. The

1150 change in M+2 succinate is significant (by two-way ANOVA test) at one hour after ^{13}C glucose

1151 incubation.

1152 **c.** Fractional enrichment of M+3 succinate in EV (red) and MPC+ (blue) HepG2 at the indicated

1153 times after ^{13}C-glucose tracing. MPC expression was induced for 24 hours by treatment with 1

1154 μg/ml doxycycline. The change in M+3 succinate is significant (by two-way ANOVA test) at four

1155 hours after ^{13}C-glucose incubation.

1156 **d.** Rate of oxygen consumption (OCR) in EV and MPC+ HepG2 cells.

1157 **e-f. e)** Representative images of phalloidin- and DAPI-stained fat body cells. Arrows indicate GFP-

1158 positive clones with MPC expression (MPC+), *Pcb* knock down with MPC expression (MPC+,

1159 *Pcb*-KD) or *Pcb* overexpression (*Pcb*+). The scale bar represents 20 μm. **f)** Quantification of the

1160 area of GFP-positive clones with control, MPC+, *Pcb* over-expression (*Pcb*+), *Pcb* and MPC co-

1161 expression (MPC+, *Pcb*+), *Pcb* knock down (*Pcb*-KD) and *Pcb* knock down with MPC expression

1162 (MPC+, *Pcb*-KD) shown as mean ± s.d. of five biological replicates, with each group representing

1163 the analysis of 20 the indicated clonal cells.

1164 **g-h.** Concentration of glucose in the fat body **(g)** and hemolymph **(h)** of larva with fat body-specific

1165 expression MPC or control. Data is presented as mean ± s.d. of three biological replicates

1166 analyzed by unpaired t-tests.

1167 **i-k**. **i)** Schematic illustration of the strategy to analyze gluconeogenesis from ^{13}C-lactate. Cells

1168 convert ^{13}C-lactate into ^{13}C-pyruvate, which is transported into mitochondria by the MPC. PC

1169 converts ^{13}C-pyruvate (M+3) into oxaloacetate (M+3). PEPCK2 converts oxaloacetate (M+3) into

1170 phosphoenolpyruvate (M+3), which is converted into M+6 glucose and excreted from cells. **j)**

1171 Relative abundances of M+3 phosphoenolpyruvate (PEP) in EV and MPC+ HepG2 cells and **k)**

1172 M+6 glucose in their respective media following treatment with 20 mM ^{13}C-lactate for four hours.

1173 Data is presented as mean ± s.d. of three biological replicates, each with an average of three

1174 technical replicates.

1175 **l-m**. **l)** Representative brightfield images of EV, MPC+, and PC knockout (KO) or PEPCK2 KO

1176 with or without MPC expression HepG2 spheroids. The scale bar represents 200 μm. **m)**

1177 Quantification of spheroid area is presented as mean ± s.d. of 30 technical replicates.

1178 **n-o**. **n)** Representative images of phalloidin- and DAPI-stained of fat body cells. Arrows indicate

1179 GFP-positive clones with MPC expression (MPC+), and *Pepck2* knockdown with MPC expression

1180 (MPC+, *Pepck2*-KD). The scale bar represents 20 μm. **o)** Quantification of the area of GFP-

1181 positive clones with MPC+, *Pepck2* knock down (*Pepck2*-KD), *Pepck2* knock down with MPC+

1182 (MPC+, *Pepck2*-KD), *Fbp* knock down (*Fbp*-KD), *Fbp* knock down with MPC+ (MPC+, *Fbp*-KD).

1183 Data is presented as mean ± s.d. of five biological replicates, with each group analyzing 20 clonal

1184 cells of the mentioned genetic manipulations.

1185 **n-o**. **n)** Representative images of fat body clones stained with OPP (red). Arrows indicate GFP-

1186 positive clones with MPC expression (MPC+), *Pcb* knockdown with MPC expression (MPC+, *Pcb*-

1187 KD), or *Pepck2* knockdown with MPC expression (MPC+, *Pepck2*-KD). The scale bar represents

1188 20 μm. **o)** Quantification of OPP intensity in the indicated clones compared with adjacent wild-

1189 type cells. Data is presented as mean ± s.d.

1190 Unpaired t-tests, one-way ANOVA tests, or two-way ANOVA tests were performed to evaluate

1191 the statistical significance of the data, with p-values mentioned in the graph if significance is noted.

1192

1193 **Supplementary Figure 5: Surge of mitochondrial pyruvate reduced glycolysis and**

1194 **promotes gluconeogenesis via Pyruvate Carboxylase (Related to Main Figure 4).**

1195 **a-c.** Fractional enrichment of M+3 3-phosphoglyceric acid **(a)**, M+3 pyruvate **(b)**, and M+3 alanine

1196 **(c)** in empty vector (EV; red) and MPC expressing (MPC+; blue)) HepG2 cells at the indicated

1197 times after ^{13}C glucose tracing.

1198 **d-e.** Fractional enrichment of M+2 fumarate **(d)** and M+2 malate **(e)** in EV (red) and MPC+ (blue)

1199 HepG2 cells.

1200   **f-g.** Fractional enrichment of M+3 fumarate **(f)** and M+3 malate **(g)** in EV (red) and MPC+ (blue)

1201   HepG2 cells. A two-way ANOVA test showed significant differences at four hours after ^{13}C glucose

1202   tracing.

1203

1204   **Supplementary Figure 6: Surge of mitochondrial pyruvate promotes gluconeogenesis via**

1205   **Pyruvate Carboxylase to suppress protein synthesis (Related to Main Figure 4).**

1206   **a.** Quantification of the area of GFP-positive fat body clones with control, MPC expression

1207   (MPC+), *Pcb* knockout (*Pcb KO*), or MPC expression with *Pcb* knockout (MPC+, *Pcb* KO). Data

1208   is presented as mean ± s.d. of five biological replicates, with each group analyzing 20 clonal cells

1209   of the indicated genetic manipulations.

1210   **b.** Quantification of the areas of HepG2 cells with MPC+ with or without pyruvate carboxylase

1211   (PC) knockout using two independent sgRNA guides (PCg5 and PCg6). Western blots show the

1212   efficiency of PC knockout. Data is presented as mean ± s.d. of five biological replicates, each

1213   representing 25 randomly selected cells for each indicated genotype.

1214   **c-d. c)** Representative images of phalloidin- and DAPI-stained fat body cells. Arrows indicate

1215   GFP-positive clones with MPC expression (MPC+), *Pdha* knock down (*Pdha*-KD), or MPC

1216   expression with *Pdk* knock down (MPC+, *Pdk*-KD). The scale bar represents 20 µm. Right. **d)**

1217   Quantification of the areas of GFP-positive clones with control, MPC+, *Pdha* knock down (*Pdha*-

1218   KD), *Pdha*-knock down with MPC expression (MPC+, *Pdha-* KD), *Dlat* knock down (*Dlat*-KD), *Dlat*

1219   knock down with MPC expression (MPC+, *Dlat*-KD); *Pdk* knock down (*Pdk*-KD), and *Pdk* knock

1220   down with MPC expression (MPC+, *Pdk*-KD). Data is presented as mean ± s.d. of five biological

1221   replicates, with 20 clonal cells analyzed for each of the indicated genetic manipulations.

1222   **e.** Quantification of the areas of MPC+ HepG2 cells treated with the PDK inhibitors AZD7545 (10

1223   µM) or dichloroacetate (1 mM). Data is presented as mean ± s.d. of five biological replicates, with

1224   25 randomly selected cells analyzed for each of the indicated groups.

1225   **f.** Quantification of the areas of MPC+, PEPCK2 knock out HepG2 cells. Western blots show the

1226   efficiency of PEPCK2 knockout. Data is presented as mean ± s.d. of five biological replicates with

1227   25 randomly selected cells analyzed for each of the indicated groups.

1228   **g.** Quantification of the area of GFP-positive control; MPC+; *Pepck2 KO*; and MPC+, *Pepck2 KO*

1229   fat body clonal cells. Data is presented as mean ± s.d. of five biological replicates, with 20 clonal

1230   cells analyzed for each of the indicated genetic manipulations.

1231   Unpaired t-tests, one-way ANOVA tests, or two-way ANOVA tests were performed to evaluate

1232   the statistical significance of the data, and p-values are mentioned in the graph if significance is

1233   noted.

1234

1235   **Figure 5: Redox imbalance impedes protein synthesis and cell growth from elevated**

1236   **pyruvate metabolism in mitochondria.**

1237   **a.** NADH/NAD$^+$ ratios from the cytoplasmic and mitochondrial fractions of control and MPC-

1238   expressing (MPC+) fat bodies. Data is presented as mean ± s.d. of six biological replicates.

1239   **b.** NADH/NAD$^+$ ratios from the cytoplasmic and mitochondrial fractions of empty vector (EV) and

1240   MPC-expressing (MPC+) HepG2 spheroids. Data is presented as mean ± s.d. of six biological

1241   replicates.

1242   **c-d. c)** Representative images of phalloidin- and DAPI-stained fat bodies. Arrows indicate GFP-

1243   positive cells with either MPC+ or MPC and *Nmnat* co-expression (MPC+, *Nmnat*+). The scale

1244   bar represents 20 μm. **d)** Quantification of the areas of GFP-positive cells with control, MPC+,

1245   *Nmnat* overexpression (*Nmnat*+), MPC and *Nmnat* co-expression (MPC+, *Nmnat*+). Data is

1246   presented as mean ± s.d. of five biological replicates, with 20 clonal cells analyzed for each of the

1247   indicated genetic manipulations.

1248   **e-f. e)** Representative images of Phalloidin and DAPI-stained fat body tissues. Arrows indicate

1249   GFP-positive cells showing MPC expression (MPC+); NDI and MPC expression (MPC+, NDI+);

1250   and NDX and MPC expression (MPC+, NDX+). The scale bar represents 20 μm. **f)** Quantification

1251   of the area of GFP-positive cells with control, MPC+, NDI expression (NDI+), NDI and MPC

1252   expression (MPC+, NDI+), NDX expression (NDX+), NDX and MPC co-expression (MPC+,

1253   NDX+). Data is presented as mean ± s.d. of five biological replicates, with 20 clonal cells analyzed

1254   for each of the indicated genetic manipulations.

1255   **g-h. g)** Representative bright field images of EV or MPC+ HepG2 spheroids cultured with NAD$^+$

1256   supplements (100 nM nicotinamide riboside or 1 μM NMN) as indicated. The scale bar represents

1257   200 μm. **h)** Quantification of spheroid area is presented as mean ± s.d. of 30 technical replicates.

1258   **i-j. i)** Representative images MPC+ or MPC+, NDI+ GFP-positive clones and of fat body cells

1259   stained with OPP (bottom). Clonal cells are mapped with dotted lines. The scale bar represents

1260   20 μm. **j)** Fold change in OPP intensity of 35 GFP-positive cells compared with adjacent wild-type

1261   cells. Data is presented as mean ± s.d.

1262   **k.** Relative accumulation of destabilized GFP (d2GFP) in spheroids of EV or MPC+ HepG2 cells

1263   treated with NAD$^+$ supplements (100 nM nicotinamide riboside or 1 μM NMN) as indicated.

1264   Unpaired t-tests, one-way ANOVA tests, or two-way ANOVA tests were performed to assess the

1265   statistical significance of the data, with p-values indicated in the graph where significance was

1266   observed.

1267

1268   **Supplementary Figure 7: Redox imbalance impedes protein synthesis and cell growth from**

1269   **elevated pyruvate metabolism in mitochondria. (related to main figure 5)**

1270   **a-b. a)** A schematic illustration of mitochondrial pyruvate metabolism and gluconeogenesis.

1271   Following are the abbreviations: PEP- phosphoenolpyruvate, F1,6BP- fructose-1, 6-

1272   bisphosphate, F6P- fructose-6-phosphate, G6P- glucose-6-phosphate, F6Pase- fructose

1273   bisphosphatase and G6PC- glucose-6-phosphatase **b)**   Western blot analysis shows the

1274   expression levels of phosphorylated PDH (p-PDH), total PDH, G6PC, PEPCK2, PC, and tubulin

1275   in MPC-overexpressing (MPC+) HepG2 cells treated with 1 μg/ml doxycycline at the indicated

1276   time points.

1277   **c.** Schematic illustrating the regulation of PDH, PC, and gluconeogenesis by a network of

1278   cofactors and substrates. Following are the abbreviations: 1,3 BPG- 1,3-bisphosphoglycerate,

1279   G3P- glucose-3-phosphate, PGK- phosphoglycerate kinase, GAPDH- glyceraldehyde-3-

1280   phosphate dehydrogenase.

1281   **d.** Fold enrichment of acetyl-CoA in EV and MPC+ HepG2 cells. Data is presented as mean ±

1282   s.d. of three biological replicates using unpaired t-tests.

1283   **e.** The ratio of ATP to ADP in EV and MPC+ HepG2 cells. Data is presented as mean ± s.d. of

1284   three biological replicates using unpaired t-tests.

1285   **f-h.** Cellular concentrations of NADH **(f)** and NAD^+ **(g)** and $NADH/NAD^+$ ratios **(h)** in EV and MPC+

1286   HepG2 cells 24 hours after treatment with 1 μg/ml doxycycline. Data is presented as mean ± s.d.

1287   of three biological replicates using unpaired t-tests.

1288   **i.** Quantification of the areas of MPC+ HepG2 cells cultured with 2 nM gramicidin. Data is

1289   presented as mean ± s.d. of five biological replicates, with 25 randomly selected cells analyzed

1290   for each of the indicated groups.

1291   **j-k. j)** Representative bright field images of EV or MPC+ HepG2 spheroids with NDI expression

1292   (NDI+). The scale bar represents 200 μm. **k)** Quantification of spheroid areas is presented as

1293   mean ± s.d. of 30 technical replicates. Western blots show the efficiency of MPC expression.

1294   **l.** Quantification of the area of MPC-expressing HepG2 cells cultured with or without 100 nM

1295   duroquinone. Data is presented as average ± s.d. of five biological replicates, with each group

1296 consisting of 25 randomly selected cells. Data is presented as mean ± s.d. of three biological

1297 replicates.

1298 Unpaired t-tests, one-way ANOVA, or two-way ANOVA tests were performed to assess the

1299 statistical significance, with p-values indicated in the graph where significance was noted.

1300

1301 **Figure 6: Reduced amino acid abundance impairs size of MPC overexpressing cells.**

1302 **a.** A heat map of the abundances of amino acids in empty vector (EV) and MPC expressing

1303 (MPC+) HepG2 cells cultured under standard conditions. Color codes indicate relative

1304 abundances for each amino acid: Blue (low), Green (similar), and Yellow (high).

1305 **b-c. b)** Representative bright field images of EV or MPC+ HepG2 spheroids cultured with 2x or

1306 3x the recommended concentration of non-essential amino acids cocktail (NEAA). The scale bar

1307 represents 200 μm. **c)** Quantification of spheroid areas from EV and MPC+ HepG2 spheroids

1308 cultured with 2x or 3x NEAA. Data is presented as mean ± s.d. of 30 technical replicates.

1309 **d-e**. **d)** Representative images of phalloidin- and DAPI-stained fat body cells from animals fed a

1310 standard diet or a diet supplemented with 5x NEAA. Arrows indicate GFP-positive clones with

1311 MPC expression (MPC+). The scale bar represents 20 μm. **e)** Quantification of the area of MPC+

1312 fat body clonal cells. Data is presented as mean ± s.d. of five biological replicates, with each data

1313 point representing the average size of 20 clones collected from five male larvae.

1314 **f-g. f)** Representative images of phalloidin- and DAPI-stained fat body cells. Arrows indicate GFP-

1315 positive MPC+ clones and MPC+ and *slimfast* over-expression (MPC+, *Slif*+). The scale bar

1316 represents 20 μm. **g)** Quantification of the area of GFP-positive clones with control, MPC

1317 expression, *Slimfast* over-expression (*Slif*+) and MPC+ clones with *Slimfast* over-expression

1318 (MPC+, *Slif*+). Data presented as mean ± s.d. of five biological replicates, with each 20 clonal

1319 cells analyzed for each of the indicated genetic manipulations.

1320 **h.** Quantification of the cell areas of EV or MPC+ HepG2 cells cultured under standard conditions

1321 or with excess of the indicated amino acid—10 mM glycine, 5 mM alanine, 5 mM serine, 5 mM

1322 asparagine, 5 mM aspartic acid, 5 mM glutamic acid or 5 mM proline. Data is presented as mean

1323 ± s.d. of five biological replicates.

1324 **i-j. i)** Representative images of phalloidin- and DAPI-stained fat body cells. Arrows indicated GFP-

1325 positive cells with MPC expression (MPC+), *Got2* knock down (*Got2* KD), and *Got2* over-

1326 expression with MPC expression (MPC+, *Got2*+). **j)** Quantification of the area of GFP-positive

1327 clones with control, MPC expression (MPC+), *Got2* knock down (*Got2*-KD), *Got2* knock down

1328 with MPC expression (MPC+, *Got2*-KD), *Got2* over-expression (*Got2*+) and *Got2* over-expression

1329 with MPC expression (MPC+, *Got2*+). Data is presented as mean ± s.d. of five biological

1330 replicates, with each 20 clonal cells analyzed for each of the specified genetic manipulations.

1331 **k.** NADH/NAD$^+$ ratio in cells treated with 10 μM UK5099, 1 μM NMN, or 5 mM aspartate. Data is

1332 presented as mean ± s.d. of three biological replicates.

1333 **l-m. l)** Western blot analysis of puromycin-labeled (20 μg/ml puromycin for 30 minutes) nascent

1334 protein in EV or MPC+ HepG2 cells cultured with 10 μM UK5099, 1 μM NMN, or 5 mM aspartate.

1335 **m)** Quantification of intensities of puromycin labeling in EV and MPC+ cell lysates.

1336 Unpaired t-tests and one-way ANOVA tests were performed to evaluate the statistical significance

1337 of the data, and p-values are noted in the graph if significance is observed.

1338

1339 **Supplementary Figure 8: Reduced Aspartate/ Glutamate abundance impairs size of MPC**

1340 **overexpressing cells.**

1341 **a-b. a)** Representative bright field images of empty vector (EV) or MPC over-expressing (MPC+)

1342 HepG2 spheroids cultured with either 5 mM aspartate (Asp) or 5 mM glutamate (Glu). The scale

1343 bar represents 200 μm. **b)** Quantification of spheroid area is presented as mean ± s.d. of 30

1344 technical replicates.

1345 **c-d. c)** Representative bright field images of EV or MPC+ HepG2 spheroids with SLC1A3

1346 overexpression (SLC13A+). The scale bar represents 200 μm. **d)** Quantification of spheroid area

1347 is presented as mean ± s.d. of 30 technical replicates. Western blots show the efficiency of MPC

1348 expression.

1349 **e.** Quantification of d2GFP in EV or MPC+ HepG2 spheroids cultured under standard conditions

1350 or with three times the recommended concentration of non-essential amino acids cocktail (3X

1351 NEAA).

1352 **f.** Quantification of the areas of EV and MPC+ HepG2 cells and HepG2 cells GOT2 knock out

1353 (GOT2-KO) with or without MPC expression. Data is presented as mean ± s.d. of five biological

1354 replicates, with 25 randomly selected cells analyzed per replicate.

1355 **g-h**. **g)** Representative bright field images of EV, MPC+, GOT2+, and MPC+, GOT2+ HepG2

1356 spheroids. The scale bar represents 200 μm. **h)** Quantification of spheroid areas is presented as

1357 mean ± s.d. of 30 technical replicates. Western blots show the efficiency of GOT2 over-

1358 expression.

1359 Unpaired t-tests and one-way ANOVA tests were performed to evaluate the statistical significance

1360 of the data, and p-values are noted in the graph if significance is observed.

1361

Figure 7: Increased mitochondrial pyruvate transport rewires metabolism and redox status to reduce protein synthesis and cell size in rat primary hepatocytes.

a. Western blot analysis of MPC overexpression in cultured rat primary hepatocytes.

b. Representative confocal images of rat primary hepatocytes expressing exogenous GFP or MPC. DIC images and DAPI staining of nuclei are also shown. Cell boundaries are marked with dotted lines. The scale bar represents 20 μm.

c. Quantification of the areas of GFP and MPC expressing primary hepatocytes. Data is presented as mean ± s.d. of six biological replicates, with 20 hepatocytes analyzed for GFP and MPC+.

d. Fluorescence intensity of puromycin-labeled nascent proteins in GFP and MPC+ primary hepatocytes. Data is presented as mean ± s.d. of six biological replicates, with 20 hepatocytes analyzed for each condition.

e. Quantification of glucose in the culture media of primary hepatocytes transfected with GFP or MPC constructs, conditioned with 20 mM lactate and 2 mM pyruvate for four hours. 10 μM UK5099 was used to inhibit MPC's downstream impact on gluconeogenesis. Data is presented as mean ± s.d. of 3 biological replicates.

f. NADH/NAD$^+$ ratios in the cytoplasmic and mitochondrial fractions of GFP or MPC+ primary hepatocytes. Data is presented as mean ± s.d. of three biological replicates.

g. Schematics illustrating the metabolic consequences of excess mitochondrial pyruvate in hepatocytes. Under normal conditions, mitochondrial pyruvate fuels the TCA cycle, maintaining redox balance and generating sufficient amino acids for cellular homeostasis. However, when mitochondrial pyruvate transport is increased and excess pyruvate is metabolized, both mitochondrial and cytoplasmic redox states are altered. This excess pyruvate enhances the activities of pyruvate carboxylase (PC), pyruvate dehydrogenase (PDH), and the TCA cycle, leading to an elevated NADH/NAD$^+$ ratio. The oxaloacetate produced by PC is converted into phosphoenolpyruvate via PEPCK2, promoting gluconeogenesis. This shift reduces the availability of aspartate and related amino acids necessary for protein synthesis, ultimately resulting in a reduction in cell size without impacting the canonical cell growth signaling pathways.

References

Alkan, H. F., Walter, K. E., Luengo, A., Madreiter-Sokolowski, C. T., Stryeck, S., Lau, A. N., Al-Zoughbi, W., Lewis, C. A., Thomas, C. J., Hoefler, G., Graier, W. F., Madl, T., Vander Heiden, M. G., & Bogner-Strauss, J. G. (2018). Cytosolic Aspartate Availability Determines Cell Survival When Glutamine Is Limiting. *Cell Metab*, *28*(5), 706-720 e706. https://doi.org/10.1016/j.cmet.2018.07.021

Amodeo, A. A., & Skotheim, J. M. (2016). Cell-Size Control. *Cold Spring Harb Perspect Biol, 8*(4), a019083. https://doi.org/10.1101/cshperspect.a019083

Arrese, E. L., & Soulages, J. L. (2010). Insect fat body: energy, metabolism, and regulation. *Annu Rev Entomol, 55*, 207-225. https://doi.org/10.1146/annurev-ento-112408-085356

Baena, E., Gandarillas, A., Vallespinos, M., Zanet, J., Bachs, O., Redondo, C., Fabregat, I., Martinez, A. C., & de Alboran, I. M. (2005). c-Myc regulates cell size and ploidy but is not essential for postnatal proliferation in liver. *Proc Natl Acad Sci U S A, 102*(20), 7286-7291. https://doi.org/10.1073/pnas.0409260102

Baker, S. A., & Rutter, J. (2023). Metabolites as signalling molecules. *Nat Rev Mol Cell Biol, 24*(5), 355-374. https://doi.org/10.1038/s41580-022-00572-w

Bensard, C. L., Wisidagama, D. R., Olson, K. A., Berg, J. A., Krah, N. M., Schell, J. C., Nowinski, S. M., Fogarty, S., Bott, A. J., Wei, P., Dove, K. K., Tanner, J. M., Panic, V., Cluntun, A., Lettlova, S., Earl, C. S., Namnath, D. F., Vazquez-Arreguin, K., Villanueva, C. J., . . . Rutter, J. (2020). Regulation of Tumor Initiation by the Mitochondrial Pyruvate Carrier. *Cell Metab, 31*(2), 284-300 e287. https://doi.org/10.1016/j.cmet.2019.11.002

Birsoy, K., Wang, T., Chen, W. W., Freinkman, E., Abu-Remaileh, M., & Sabatini, D. M. (2015). An Essential Role of the Mitochondrial Electron Transport Chain in Cell Proliferation Is to Enable Aspartate Synthesis. *Cell, 162*(3), 540-551. https://doi.org/10.1016/j.cell.2015.07.016

Bjorklund, M. (2019). Cell size homeostasis: Metabolic control of growth and cell division. *Biochim Biophys Acta Mol Cell Res, 1866*(3), 409-417. https://doi.org/10.1016/j.bbamcr.2018.10.002

Bornstein, M. R., Tian, R., & Arany, Z. (2024). Human cardiac metabolism. *Cell Metab, 36*(7), 1456-1481. https://doi.org/10.1016/j.cmet.2024.06.003

Bricker, D. K., Taylor, E. B., Schell, J. C., Orsak, T., Boutron, A., Chen, Y. C., Cox, J. E., Cardon, C. M., Van Vranken, J. G., Dephoure, N., Redin, C., Boudina, S., Gygi, S. P., Brivet, M., Thummel, C. S., & Rutter, J. (2012). A mitochondrial pyruvate carrier required for pyruvate uptake in yeast, Drosophila, and humans. *Science, 337*(6090), 96-100. https://doi.org/10.1126/science.1218099

Chai, P., Lan, P., Li, S., Yao, D., Chang, C., Cao, M., Shen, Y., Ge, S., Wu, J., Lei, M., & Fan, X. (2022). Mechanistic insight into allosteric activation of human pyruvate carboxylase by acetyl-CoA. *Mol Cell, 82*(21), 4116-4130 e4116. https://doi.org/10.1016/j.molcel.2022.09.033

Cluntun, A. A., Badolia, R., Lettlova, S., Parnell, K. M., Shankar, T. S., Diakos, N. A., Olson, K. A., Taleb, I., Tatum, S. M., Berg, J. A., Cunningham, C. N., Van Ry, T., Bott, A. J., Krokidi, A. T., Fogarty, S., Skedros, S., Swiatek, W. I., Yu, X., Luo, B., . . . Drakos, S. G. (2021). The pyruvate-lactate axis modulates cardiac hypertrophy and heart failure. *Cell Metab, 33*(3), 629-648 e610. https://doi.org/10.1016/j.cmet.2020.12.003

Colombani, J., Raisin, S., Pantalacci, S., Radimerski, T., Montagne, J., & Leopold, P. (2003). A nutrient sensor mechanism controls Drosophila growth. *Cell, 114*(6), 739-749. https://doi.org/10.1016/s0092-8674(03)00713-x

Dang, C. V. (1999). c-Myc target genes involved in cell growth, apoptosis, and metabolism. *Mol Cell Biol, 19*(1), 1-11. https://doi.org/10.1128/MCB.19.1.1

DeBerardinis, R. J., & Thompson, C. B. (2012). Cellular metabolism and disease: what do metabolic outliers teach us? *Cell, 148*(6), 1132-1144. https://doi.org/10.1016/j.cell.2012.02.032

Deliu, L. P., Ghosh, A., & Grewal, S. S. (2017). Investigation of protein synthesis in Drosophila larvae using puromycin labelling. *Biol Open, 6*(8), 1229-1234. https://doi.org/10.1242/bio.026294

Edgar, B. A., & Orr-Weaver, T. L. (2001). Endoreplication cell cycles: more for less. *Cell*, *105*(3), 297-306. https://doi.org/10.1016/s0092-8674(01)00334-8

Fernandez-Caggiano, M., Kamynina, A., Francois, A. A., Prysyazhna, O., Eykyn, T. R., Krasemann, S., Crespo-Leiro, M. G., Vieites, M. G., Bianchi, K., Morales, V., Domenech, N., & Eaton, P. (2020). Mitochondrial pyruvate carrier abundance mediates pathological cardiac hypertrophy. *Nat Metab*, *2*(11), 1223-1231. https://doi.org/10.1038/s42255-020-00276-5

Ghosh-Choudhary, S., Liu, J., & Finkel, T. (2020). Metabolic Regulation of Cell Fate and Function. *Trends Cell Biol*, *30*(3), 201-212. https://doi.org/10.1016/j.tcb.2019.12.005

Ginzberg, M. B., Chang, N., D'Souza, H., Patel, N., Kafri, R., & Kirschner, M. W. (2018). Cell size sensing in animal cells coordinates anabolic growth rates and cell cycle progression to maintain cell size uniformity. *Elife*, *7*. https://doi.org/10.7554/eLife.26957

Gonzalez, A., & Hall, M. N. (2017). Nutrient sensing and TOR signaling in yeast and mammals. *EMBO J*, *36*(4), 397-408. https://doi.org/10.15252/embj.201696010

Gonzalez, S., & Rallis, C. (2017). The TOR Signaling Pathway in Spatial and Temporal Control of Cell Size and Growth. *Front Cell Dev Biol*, *5*, 61. https://doi.org/10.3389/fcell.2017.00061

Goodman, R. P., Markhard, A. L., Shah, H., Sharma, R., Skinner, O. S., Clish, C. B., Deik, A., Patgiri, A., Hsu, Y. H., Masia, R., Noh, H. L., Suk, S., Goldberger, O., Hirschhorn, J. N., Yellen, G., Kim, J. K., & Mootha, V. K. (2020). Hepatic NADH reductive stress underlies common variation in metabolic traits. *Nature*, *583*(7814), 122-126. https://doi.org/10.1038/s41586-020-2337-2

Gospodaryov, D. V., Strilbytska, O. M., Semaniuk, U. V., Perkhulyn, N. V., Rovenko, B. M., Yurkevych, I. S., Barata, A. G., Dick, T. P., Lushchak, O. V., & Jacobs, H. T. (2020). Alternative NADH dehydrogenase extends lifespan and increases resistance to xenobiotics in Drosophila. *Biogerontology*, *21*(2), 155-171. https://doi.org/10.1007/s10522-019-09849-8

Gratz, S. J., Ukken, F. P., Rubinstein, C. D., Thiede, G., Donohue, L. K., Cummings, A. M., & O'Connor-Giles, K. M. (2014). Highly specific and efficient CRISPR/Cas9-catalyzed homology-directed repair in Drosophila. *Genetics*, *196*(4), 961-971. https://doi.org/10.1534/genetics.113.160713

Gray, L. R., Sultana, M. R., Rauckhorst, A. J., Oonthonpan, L., Tompkins, S. C., Sharma, A., Fu, X., Miao, R., Pewa, A. D., Brown, K. S., Lane, E. E., Dohlman, A., Zepeda-Orozco, D., Xie, J., Rutter, J., Norris, A. W., Cox, J. E., Burgess, S. C., Potthoff, M. J., & Taylor, E. B. (2015). Hepatic Mitochondrial Pyruvate Carrier 1 Is Required for Efficient Regulation of Gluconeogenesis and Whole-Body Glucose Homeostasis. *Cell Metab*, *22*(4), 669-681. https://doi.org/10.1016/j.cmet.2015.07.027

Grewal, S. S. (2009). Insulin/TOR signaling in growth and homeostasis: a view from the fly world. *Int J Biochem Cell Biol*, *41*(5), 1006-1010. https://doi.org/10.1016/j.biocel.2008.10.010

Hatting, M., Tavares, C. D. J., Sharabi, K., Rines, A. K., & Puigserver, P. (2018). Insulin regulation of gluconeogenesis. *Ann N Y Acad Sci*, *1411*(1), 21-35. https://doi.org/10.1111/nyas.13435

Hausler, N., Browning, J., Merritt, M., Storey, C., Milde, A., Jeffrey, F. M., Sherry, A. D., Malloy, C. R., & Burgess, S. C. (2006). Effects of insulin and cytosolic redox state on glucose production pathways in the isolated perfused mouse liver measured by integrated 2H and 13C NMR. *Biochem J*, *394*(Pt 2), 465-473. https://doi.org/10.1042/BJ20051174

Henry, J. A., Couch, L. S., & Rider, O. J. (2024). Myocardial Metabolism in Heart Failure with Preserved Ejection Fraction. *J Clin Med*, *13*(5). https://doi.org/10.3390/jcm13051195

1493 Herzig, S., Raemy, E., Montessuit, S., Veuthey, J. L., Zamboni, N., Westermann, B., Kunji, E. R.,
1494   & Martinou, J. C. (2012). Identification and functional expression of the mitochondrial
1495   pyruvate carrier. *Science*, *337*(6090), 93-96. https://doi.org/10.1126/science.1218530
1496 Holecek, M. (2023a). Aspartic Acid in Health and Disease. *Nutrients*, *15*(18).
1497   https://doi.org/10.3390/nu15184023
1498 Holecek, M. (2023b). Roles of malate and aspartate in gluconeogenesis in various physiological
1499   and pathological states. *Metabolism*, *145*, 155614.
1500   https://doi.org/10.1016/j.metabol.2023.155614
1501 Iritani, B. M., & Eisenman, R. N. (1999). c-Myc enhances protein synthesis and cell size during B
1502   lymphocyte development. *Proc Natl Acad Sci U S A*, *96*(23), 13180-13185.
1503   https://doi.org/10.1073/pnas.96.23.13180
1504 Ito, K., Awano, W., Suzuki, K., Hiromi, Y., & Yamamoto, D. (1997). The Drosophila mushroom
1505   body is a quadruple structure of clonal units each of which contains a virtually identical set
1506   of neurones and glial cells. *Development*, *124*(4), 761-771.
1507   https://doi.org/10.1242/dev.124.4.761
1508 Jitrapakdee, S., St Maurice, M., Rayment, I., Cleland, W. W., Wallace, J. C., & Attwood, P. V.
1509   (2008). Structure, mechanism and regulation of pyruvate carboxylase. *Biochem J*, *413*(3),
1510   369-387. https://doi.org/10.1042/BJ20080709
1511 Jokinen, M. J., & Luukkonen, P. K. (2024). Hepatic mitochondrial reductive stress in the
1512   pathogenesis and treatment of steatotic liver disease. *Trends Pharmacol Sci*, *45*(4), 319-
1513   334. https://doi.org/10.1016/j.tips.2024.02.003
1514 Kast, A., Nishikawa, J., Yabe, T., Nanri, H., & Albert, H. (1988). Circadian rhythm of liver
1515   parameters (cellular structures, mitotic activity, glycogen and lipids in liver and serum)
1516   during three consecutive cycles in phenobarbital-treated rats. *Chronobiol Int*, *5*(4), 363-
1517   385. https://doi.org/10.3109/07420528809067782
1518 Kiesel, V. A., Sheeley, M. P., Coleman, M. F., Cotul, E. K., Donkin, S. S., Hursting, S. D., Wendt,
1519   M. K., & Teegarden, D. (2021). Pyruvate carboxylase and cancer progression. *Cancer*
1520   *Metab*, *9*(1), 20. https://doi.org/10.1186/s40170-021-00256-7
1521 Lang, F., Busch, G. L., Ritter, M., Volkl, H., Waldegger, S., Gulbins, E., & Haussinger, D. (1998).
1522   Functional significance of cell volume regulatory mechanisms. *Physiol Rev*, *78*(1), 247-
1523   306. https://doi.org/10.1152/physrev.1998.78.1.247
1524 Li, X., Zhao, X., Fang, Y., Jiang, X., Duong, T., Fan, C., Huang, C. C., & Kain, S. R. (1998).
1525   Generation of destabilized green fluorescent protein as a transcription reporter. *J Biol*
1526   *Chem*, *273*(52), 34970-34975. https://doi.org/10.1074/jbc.273.52.34970
1527 Lieu, E. L., Nguyen, T., Rhyne, S., & Kim, J. (2020). Amino acids in cancer. *Exp Mol Med*, *52*(1),
1528   15-30. https://doi.org/10.1038/s12276-020-0375-3
1529 Liu, S., Tan, C., Tyers, M., Zetterberg, A., & Kafri, R. (2022). What programs the size of animal
1530   cells? *Front Cell Dev Biol*, *10*, 949382. https://doi.org/10.3389/fcell.2022.949382
1531 Lloyd, A. C. (2013). The regulation of cell size. *Cell*, *154*(6), 1194-1205.
1532   https://doi.org/10.1016/j.cell.2013.08.053
1533 Lunt, S. Y., & Vander Heiden, M. G. (2011). Aerobic glycolysis: meeting the metabolic
1534   requirements of cell proliferation. *Annu Rev Cell Dev Biol*, *27*, 441-464.
1535   https://doi.org/10.1146/annurev-cellbio-092910-154237
1536 McCommis, K. S., Chen, Z., Fu, X., McDonald, W. G., Colca, J. R., Kletzien, R. F., Burgess, S.
1537   C., & Finck, B. N. (2015). Loss of Mitochondrial Pyruvate Carrier 2 in the Liver Leads to
1538   Defects in Gluconeogenesis and Compensation via Pyruvate-Alanine Cycling. *Cell Metab*,
1539   *22*(4), 682-694. https://doi.org/10.1016/j.cmet.2015.07.028
1540 McCommis, K. S., Kovacs, A., Weinheimer, C. J., Shew, T. M., Koves, T. R., Ilkayeva, O. R.,
1541   Kamm, D. R., Pyles, K. D., King, M. T., Veech, R. L., DeBosch, B. J., Muoio, D. M., Gross,

R. W., & Finck, B. N. (2020). Nutritional modulation of heart failure in mitochondrial pyruvate carrier-deficient mice. *Nat Metab*, *2*(11), 1232-1247. https://doi.org/10.1038/s42255-020-00296-1

Merker, M. P., Audi, S. H., Bongard, R. D., Lindemer, B. J., & Krenz, G. S. (2006). Influence of pulmonary arterial endothelial cells on quinone redox status: effect of hyperoxia-induced NAD(P)H:quinone oxidoreductase 1. *Am J Physiol Lung Cell Mol Physiol*, *290*(3), L607-619. https://doi.org/10.1152/ajplung.00302.2005

Metallo, C. M., & Vander Heiden, M. G. (2013). Understanding metabolic regulation and its influence on cell physiology. *Mol Cell*, *49*(3), 388-398. https://doi.org/10.1016/j.molcel.2013.01.018

Musselman, L. P., Fink, J. L., Ramachandran, P. V., Patterson, B. W., Okunade, A. L., Maier, E., Brent, M. R., Turk, J., & Baranski, T. J. (2013). Role of fat body lipogenesis in protection against the effects of caloric overload in Drosophila. *J Biol Chem*, *288*(12), 8028-8042. https://doi.org/10.1074/jbc.M112.371047

Pavlova, N. N., King, B., Josselsohn, R. H., Violante, S., Macera, V. L., Vardhana, S. A., Cross, J. R., & Thompson, C. B. (2020). Translation in amino-acid-poor environments is limited by tRNA(Gln) charging. *Elife*, *9*. https://doi.org/10.7554/eLife.62307

Petersen, M. C., Vatner, D. F., & Shulman, G. I. (2017). Regulation of hepatic glucose metabolism in health and disease. *Nat Rev Endocrinol*, *13*(10), 572-587. https://doi.org/10.1038/nrendo.2017.80

Reinke, H., & Asher, G. (2018). Liver size: Waning by day, Waxing by Night. *Hepatology*, *67*(1), 441-443. https://doi.org/10.1002/hep.29506

Rui, L. (2014). Energy metabolism in the liver. *Compr Physiol*, *4*(1), 177-197. https://doi.org/10.1002/cphy.c130024

Sanz, A., Soikkeli, M., Portero-Otin, M., Wilson, A., Kemppainen, E., McIlroy, G., Ellila, S., Kemppainen, K. K., Tuomela, T., Lakanmaa, M., Kiviranta, E., Stefanatos, R., Dufour, E., Hutz, B., Naudi, A., Jove, M., Zeb, A., Vartiainen, S., Matsuno-Yagi, A., . . . Jacobs, H. T. (2010). Expression of the yeast NADH dehydrogenase Ndi1 in Drosophila confers increased lifespan independently of dietary restriction. *Proc Natl Acad Sci U S A*, *107*(20), 9105-9110. https://doi.org/10.1073/pnas.0911539107

Saxton, R. A., & Sabatini, D. M. (2017). mTOR Signaling in Growth, Metabolism, and Disease. *Cell*, *168*(6), 960-976. https://doi.org/10.1016/j.cell.2017.02.004

Schell, J. C., Olson, K. A., Jiang, L., Hawkins, A. J., Van Vranken, J. G., Xie, J., Egnatchik, R. A., Earl, E. G., DeBerardinis, R. J., & Rutter, J. (2014). A role for the mitochondrial pyruvate carrier as a repressor of the Warburg effect and colon cancer cell growth. *Mol Cell*, *56*(3), 400-413. https://doi.org/10.1016/j.molcel.2014.09.026

Schell, J. C., Wisidagama, D. R., Bensard, C., Zhao, H., Wei, P., Tanner, J., Flores, A., Mohlman, J., Sorensen, L. K., Earl, C. S., Olson, K. A., Miao, R., Waller, T. C., Delker, D., Kanth, P., Jiang, L., DeBerardinis, R. J., Bronner, M. P., Li, D. Y., . . . Rutter, J. (2017). Control of intestinal stem cell function and proliferation by mitochondrial pyruvate metabolism. *Nat Cell Biol*, *19*(9), 1027-1036. https://doi.org/10.1038/ncb3593

Schmoller, K. M., & Skotheim, J. M. (2015). The Biosynthetic Basis of Cell Size Control. *Trends Cell Biol*, *25*(12), 793-802. https://doi.org/10.1016/j.tcb.2015.10.006

Shen, Y., Liu, W., Zuo, J., Han, J., & Zhang, Z. C. (2021). Protocol for visualizing newly synthesized proteins in primary mouse hepatocytes. *STAR Protoc*, *2*(3), 100616. https://doi.org/10.1016/j.xpro.2021.100616

Siess, E. A., Brocks, D. G., Lattke, H. K., & Wieland, O. H. (1977). Effect of glucagon on metabolite compartmentation in isolated rat liver cells during gluconeogenesis from lactate. *Biochem J*, *166*(2), 225-235. https://doi.org/10.1042/bj1660225

1591 Sinturel, F., Gerber, A., Mauvoisin, D., Wang, J., Gatfield, D., Stubblefield, J. J., Green, C. B.,
1592   Gachon, F., & Schibler, U. (2017). Diurnal Oscillations in Liver Mass and Cell Size
1593   Accompany Ribosome Assembly Cycles. *Cell*, *169*(4), 651-663 e614.
1594   https://doi.org/10.1016/j.cell.2017.04.015
1595 Stacpoole, P. W. (2017). Therapeutic Targeting of the Pyruvate Dehydrogenase
1596   Complex/Pyruvate Dehydrogenase Kinase (PDC/PDK) Axis in Cancer. *J Natl Cancer Inst*,
1597   *109*(11). https://doi.org/10.1093/jnci/djx071
1598 Stine, Z. E., Walton, Z. E., Altman, B. J., Hsieh, A. L., & Dang, C. V. (2015). MYC, Metabolism,
1599   and Cancer. *Cancer Discov*, *5*(10), 1024-1039. https://doi.org/10.1158/2159-8290.CD-15-
1600   0507
1601 Sugden, M. C., & Holness, M. J. (2011). The pyruvate carboxylase-pyruvate dehydrogenase axis
1602   in islet pyruvate metabolism: Going round in circles? *Islets*, *3*(6), 302-319.
1603   https://doi.org/10.4161/isl.3.6.17806
1604 Sullivan, L. B., Gui, D. Y., Hosios, A. M., Bush, L. N., Freinkman, E., & Vander Heiden, M. G.
1605   (2015). Supporting Aspartate Biosynthesis Is an Essential Function of Respiration in
1606   Proliferating Cells. *Cell*, *162*(3), 552-563. https://doi.org/10.1016/j.cell.2015.07.017
1607 Sullivan, L. B., Luengo, A., Danai, L. V., Bush, L. N., Diehl, F. F., Hosios, A. M., Lau, A. N.,
1608   Elmiligy, S., Malstrom, S., Lewis, C. A., & Vander Heiden, M. G. (2018). Aspartate is an
1609   endogenous metabolic limitation for tumour growth. *Nat Cell Biol*, *20*(7), 782-788.
1610   https://doi.org/10.1038/s41556-018-0125-0
1611 Tan, C., Ginzberg, M. B., Webster, R., Iyengar, S., Liu, S., Papadopoli, D., Concannon, J., Wang,
1612   Y., Auld, D. S., Jenkins, J. L., Rost, H., Topisirovic, I., Hilfinger, A., Derry, W. B., Patel, N.,
1613   & Kafri, R. (2021). Cell size homeostasis is maintained by CDK4-dependent activation of
1614   p38 MAPK. *Dev Cell*, *56*(12), 1756-1769 e1757.
1615   https://doi.org/10.1016/j.devcel.2021.04.030
1616 Tom Dieck, S., Muller, A., Nehring, A., Hinz, F. I., Bartnik, I., Schuman, E. M., & Dieterich, D. C.
1617   (2012). Metabolic labeling with noncanonical amino acids and visualization by
1618   chemoselective fluorescent tagging. *Curr Protoc Cell Biol*, *Chapter 7*, 7 11 11-17 11 29.
1619   https://doi.org/10.1002/0471143030.cb0711s56
1620 Toshniwal, A. G., Gupta, S., Mandal, L., & Mandal, S. (2019). ROS Inhibits Cell Growth by
1621   Regulating 4EBP and S6K, Independent of TOR, during Development. *Dev Cell*, *49*(3),
1622   473-489 e479. https://doi.org/10.1016/j.devcel.2019.04.008
1623 Ugrankar-Banerjee, R., Tran, S., Bowerman, J., Kovalenko, A., Paul, B., & Henne, W. M. (2023).
1624   The fat body cortical actin network regulates Drosophila inter-organ nutrient trafficking,
1625   signaling, and adipose cell size. *Elife*, *12*. https://doi.org/10.7554/eLife.81170
1626 van Riggelen, J., Yetil, A., & Felsher, D. W. (2010). MYC as a regulator of ribosome biogenesis
1627   and protein synthesis. *Nat Rev Cancer*, *10*(4), 301-309. https://doi.org/10.1038/nrc2819
1628 Vander Heiden, M. G., Cantley, L. C., & Thompson, C. B. (2009). Understanding the Warburg
1629   effect: the metabolic requirements of cell proliferation. *Science*, *324*(5930), 1029-1033.
1630   https://doi.org/10.1126/science.1160809
1631 Villalobos-Cantor, S., Barrett, R. M., Condon, A. F., Arreola-Bustos, A., Rodriguez, K. M., Cohen,
1632   M. S., & Martin, I. (2023). Rapid cell type-specific nascent proteome labeling in Drosophila.
1633   *Elife*, *12*. https://doi.org/10.7554/eLife.83545
1634 Wang, X., Shen, X., Yan, Y., & Li, H. (2021). Pyruvate dehydrogenase kinases (PDKs): an
1635   overview toward clinical applications. *Biosci Rep*, *41*(4).
1636   https://doi.org/10.1042/BSR20204402
1637 Wei, P., Bott, A. J., Cluntun, A. A., Morgan, J. T., Cunningham, C. N., Schell, J. C., Ouyang, Y.,
1638   Ficarro, S. B., Marto, J. A., Danial, N. N., DeBerardinis, R. J., & Rutter, J. (2022).
1639   Mitochondrial pyruvate supports lymphoma proliferation by fueling a glutamate pyruvate

transaminase 2-dependent glutaminolysis pathway. *Sci Adv*, *8*(39), eabq0117. https://doi.org/10.1126/sciadv.abq0117

Wei, Z., Liu, X., Cheng, C., Yu, W., & Yi, P. (2020). Metabolism of Amino Acids in Cancer. *Front Cell Dev Biol*, *8*, 603837. https://doi.org/10.3389/fcell.2020.603837

Weiss, R. C., Menezes, T. N., & McCommis, K. S. (2023). Metabolic Drivers and Rescuers of Heart Failure. *Mo Med*, *120*(5), 354-358. https://www.ncbi.nlm.nih.gov/pubmed/37841572

Xue, Y. W., Itoh, H., Dan, S., & Inoue, M. (2022). Gramicidin A accumulates in mitochondria, reduces ATP levels, induces mitophagy, and inhibits cancer cell growth. *Chem Sci*, *13*(25), 7482-7491. https://doi.org/10.1039/d2sc02024f

Yiew, N. K. H., & Finck, B. N. (2022). The mitochondrial pyruvate carrier at the crossroads of intermediary metabolism. *Am J Physiol Endocrinol Metab*, *323*(1), E33-E52. https://doi.org/10.1152/ajpendo.00074.2022

Yoo, H. C., Yu, Y. C., Sung, Y., & Han, J. M. (2020). Glutamine reliance in cell metabolism. *Exp Mol Med*, *52*(9), 1496-1516. https://doi.org/10.1038/s12276-020-00504-8

Zangari, J., Petrelli, F., Maillot, B., & Martinou, J. C. (2020). The Multifaceted Pyruvate Metabolism: Role of the Mitochondrial Pyruvate Carrier. *Biomolecules*, *10*(7). https://doi.org/10.3390/biom10071068

Zhang, S., Zatulovskiy, E., Arand, J., Sage, J., & Skotheim, J. M. (2022). The cell cycle inhibitor RB is diluted in G1 and contributes to controlling cell size in the mouse liver. *Front Cell Dev Biol*, *10*, 965595. https://doi.org/10.3389/fcell.2022.965595

Zhang, Y., Taufalele, P. V., Cochran, J. D., Robillard-Frayne, I., Marx, J. M., Soto, J., Rauckhorst, A. J., Tayyari, F., Pewa, A. D., Gray, L. R., Teesch, L. M., Puchalska, P., Funari, T. R., McGlauflin, R., Zimmerman, K., Kutschke, W. J., Cassier, T., Hitchcock, S., Lin, K., . . . Abel, E. D. (2020). Mitochondrial pyruvate carriers are required for myocardial stress adaptation. *Nat Metab*, *2*(11), 1248-1264. https://doi.org/10.1038/s42255-020-00288-1

Zheng, H., Yang, X., & Xi, Y. (2016). Fat body remodeling and homeostasis control in Drosophila. *Life Sci*, *167*, 22-31. https://doi.org/10.1016/j.lfs.2016.10.019

Zhu, J., & Thompson, C. B. (2019). Metabolic regulation of cell growth and proliferation. *Nat Rev Mol Cell Biol*, *20*(7), 436-450. https://doi.org/10.1038/s41580-019-0123-5

1686 **Table 1- Key Resource Table**

Reagent type (species) or resource	Designation	Source or reference	Identifiers	Additional Information
Strain (*Drosophila melanogaster*)	*UAS-MPC1-P2A-MPC2*	Schell et al., 2017	BDSC, #84087	Expresses Drosophila *Mpc1* and *Mpc2* cDNA separated by P2A cleavage site
Strain (*D. melanogaster*)	*hs-Flp1.22*	Bloomington *Drosophila* Stock Center	BDSC, #77928	
Strain (*D. melanogaster*)	*Act>CD2>Gal4, UAS-GFP*	Bloomington *Drosophila* Stock Center	BDSC, #4413	Ay-Gal4 fly stock used to induce mosaics in fat body
Strain (*D. melanogaster*)	*CG-Gal4*	Bloomington *Drosophila* Stock Center	BDSC, #7011	
Strain (*D. melanogaster*)	*UAS-S6k^{STDETE}*	Bloomington *Drosophila* Stock Center	BDSC, #6914	Drives constitutively active *S6k* expression
Strain (*D. melanogaster*)	*UAS-Rheb^{PA}*	Bloomington *Drosophila* Stock Center	BDSC, #9689	Drives Rheb overexpression
Strain (*D. melanogaster*)	*UAS-Myc^{OE}*	Bloomington *Drosophila* Stock Center	BDSC, #9675	Drives *Myc* overexpression
Strain (*D. melanogaster*)	*UAS-JF01761*	Bloomington *Drosophila* Stock Center	BDSC, #25783	Drives Myc dsRNA, used as *UAS-Myc^{RNAi}*
Strain (*D. melanogaster*)	*UAS-PI3K93E$^{.Excel}$*	Bloomington *Drosophila* Stock Center	BDSC, #8287	Drives *PI3K93* overexpression
Strain (*D. melanogaster*)	*UAS-Pi3K92E.A2860 C*	Bloomington *Drosophila* Stock Center	BDSC, #8288	Drives *PI3K93* dominant negative
Strain (*D. melanogaster*)	*UAS-Tsc1^{RNAi}*	Bloomington *Drosophila* Stock Center	BDSC, #31314	Drives *Tsc1* dsRNA, used as *UAS-Tsc1^{RNAi}*

Strain (*D. melanogaster*)	*UAS-hPC*	Bloomington *Drosophila* Stock Center	BDSC, #77928	Drives human PC cDNA
Strain (*D. melanogaster*)	*UAS-HMC04104*	Bloomington *Drosophila* Stock Center	BDSC, #56883	Drives *Pc* dsRNA, used as *UAS-PC^{RNAi}*
Strain (*D. melanogaster*)	*UAS-HMS00200*	Bloomington *Drosophila* Stock Center	BDSC, #36915	Drives *Pepck2* dsRNA, used as *UAS-Pepck2^{RNAi}*
Strain (*D. melanogaster*)	*UAS-HMC03445*	Bloomington *Drosophila* Stock Center	BDSC, #51871	Drives *Fbp* dsRNA, used as *UAS-Fbp^{RNAi}*
Strain (*D. melanogaster*)	*UAS-GL00009*	Bloomington *Drosophila* Stock Center	BDSC, #35142	Drives *Pdk* dsRNA, used as *UAS-Pdk^{RNAi}*
Strain (*D. melanogaster*)	*UAS-NMNAT*	Bloomington *Drosophila* Stock Center	BDSC, #39702	Drives *Nmnat* cDNA
Strain (*D. melanogaster*)	*UAS-CintNDX*	Bloomington *Drosophila* Stock Center	BDSC, #93883	Drives *Cionia intestinalis* NDX cDNA
Strain (*D. melanogaster*)	*UAS-ScerNDI1*	Bloomington *Drosophila* Stock Center	BDSC, #93878	Drives *Saccharomyces cerevisiae* NDI cDNA
Strain (*D. melanogaster*)	*UAS-slif*	Bloomington *Drosophila* Stock Center	BDSC, #52661	Drives *slimfast* cDNA
Strain (*D. melanogaster*)	*UAS-HMS05873*	Bloomington *Drosophila* Stock Center	BDSC, #78778	Drives *Got2* dsRNA, used as *UAS-Got2^{RNAi}*
Strain (*D. melanogaster*)	*UAS-Mpc1^{RNAi}*	Bricker et. al, 2012		Drives *Mpc1* dsRNA
Strain (*D. melanogaster*)	*UAS-Pdha^{RNAi}*	National Institute of Genetics, Japan	NIG 7010R-3	Drives *Pdha* dsRNA
Strain (*D. melanogaster*)	*UAS-Dlat^{RNAi}*	National Institute of Genetics, Japan	NIG 5261R-3	Drives *Dlat* dsRNA
Strain (*D. melanogaster*)	*w^{1118}*	Bloomington *Drosophila* Stock Center	BDSC:3605	Wild-type fly strain
Strain (*D. melanogaster*)	*UAS-GOT2*	This paper	see materials and methods	Drives *Got2* cDNA

Strain (*D. melanogaster*)	*Pcb KO*	This paper	see materials and methods	*Pcb* CRISPR deletion fly stock,
Strain (*D. melanogaster*)	*Pepck2 KO*	This paper	see materials and methods	*Pepck2* CRISPR deletion fly stock,
Cell line (Homo *sapiens*)	HepG2	ATCC	Cat# HB-8065	a hepatocellular carcinoma cell line
Primary hepatocytes	Cryopreserved Rat Hepatocytes	Lonza	Cat# RWCP01	Plateable, Rat Wistar Hannover Hepatocytes, cryopreserved
Antibody	anti-puromycin [3RH11] (host: mouse monoclonal)	Kerafast	Cat# EQ0001	Dilution factor 1:1000 for western blot And 1:200 for immunofluorescence
Antibody	anti-MPC1 (*Drosophila*) (host: rabbit monoclonal)	gift from R. Kletzein		Dilution factor 1:200 for immunofluorescence
Antibody	anti-MPC2 (*Drosophila*) (host: rabbit monoclonal)	gift from R. Kletzein		Dilution factor 1:200 for immunofluorescence
Antibody	anti-p-S6 (host: rabbit monoclonal)	gift from A. Teleman		Dilution factor 1:200 for immunofluorescence
Antibody	anti-dFoxo (host: rabbit monoclonal)	gift from P. Bellosta		Dilution factor 1:500 for immunofluorescence
Antibody	anti-p-4EBP (host: rabbit monoclonal)	Cell Signaling Technologies	Cat# 2855	Dilution factor 1:1000 for western blot And 1:500 for immunofluorescence
Antibody	anti-p-eIF2α (host: rabbit monoclonal)	Cell Signaling Technologies	Cat# 9721	Dilution factor 1:500 for immunofluorescence

Antibody	Cy3 conjugated anti-rabbit (host: donkey polyclonal)	Jacksons Immuno Research Laboratories	Cat# 711–165-152	Dilution factor 1:400 for immunofluorescence
Antibody	Cy3 conjugated anti-mouse (host: donkey polyclonal)	Jacksons Immuno Research Laboratories	Cat# 115-165-166	Dilution factor 1:400 for immunofluorescence
Antibody	anti-MPC1 (host: rabbit monoclonal)	Cell Signaling Technologies	Cat# 14462	Dilution factor 1:1000 for western blot
Antibody	anti-MPC2 (host: rabbit monoclonal)	Cell Signaling Technologies	Cat# 46141	Dilution factor 1:1000 for western blot
Antibody	anti-PDH (host: rabbit monoclonal)	Cell Signaling Technologies	Cat# 3205	Dilution factor 1:1000 for western blot
Antibody	anti- p-PDH (host: rabbit monoclonal)	Cell Signaling Technologies	Cat# 31866	Dilution factor 1:1000 for western blot
Antibody	anti-PC (host: rabbit monoclonal)	Cell Signaling Technologies	Cat# 66470	Dilution factor 1:1000 for western blot
Antibody	anti-PEPCK2 (D3E11) (host: rabbit monoclonal)	Cell Signaling Technologies	Cat# 8565	Dilution factor 1:1000 for western blot
Antibody	anti-Got2 (host: rabbit monoclonal)	Sigma	Cat# HPA018139	Dilution factor 1:1000 for western blot
Antibody	anti-tubulin (DM1A) (host: mouse monoclonal)	Cell Signaling Technologies	Cat# 3873	Dilution factor 1:1000 for western blot
Antibody	anti- Flag M2 (host: mouse monoclonal)	Sigma Aldrich	Cat# F1800	Dilution factor 1:10000 for western blot 1:1000 for
Antibody	IRDye 680RD anti-mouse (host: Donkey monoclonal)	Li-COR	Cat# 926-68072	Dilution factor 1:5000 for western blot immunofluorescence
Antibody	IRDye 800RD anti-Rabbit (host: Donkey monoclonal)	Li-COR	Cat# 926-32213	Dilution factor 1:5000 for western blot
Recombinant DNA reagent	pUAST-aatB			

Recombinant DNA reagent	pLVX-TetOne-Zeocin	Takara		
Recombinant DNA reagent	Gag-Pol	Addgene		
Recombinant DNA reagent	VSVG	Addgene		
Recombinant DNA reagent	pMD2.G	Addgene		
Recombinant DNA reagent	pLenti-CMV-Blast	Addgene	Cat# 17486	
Recombinant DNA reagent	pLVX-TetOne-HA-MPC2-P2A-T2A-MPC1-FLAG-Zeo	This paper	HA-tagged MPC2 and Flag-tagged MPC1 cDNA separated by P2A/T2A cleavage site cloned into pLenti-CMV-Blast	
Recombinant DNA reagent	pLenti-CMV-PC-V5-Blast	This paper	V5-tagged PC cDNA cloned into pLenti-CMV-Blast	
Recombinant DNA reagent	pLenti-CMV-GOT2-V5-Blast	This paper	V5-tagged GOT2 cDNA cloned into pLenti-CMV-Blast	
Recombinant DNA reagent	PB-CAG-GFPd2	Addgene	Cat# 115665	
Recombinant DNA reagent	PMXS-NDI	Addgene	Cat# 72876	
Recombinant DNA reagent	pLenti-CMV-d2GFP-Blast	This paper	d2GFP cloned into pLenti-CMV-Blast	
Recombinant DNA reagent	pLenti-CMV-NDI-V5-Blast	This paper	V5-tagged NDI cloned into pLenti-CMV-Blast	
Recombinant DNA reagent	pLenti-CMV-SLC1A3-V5-Blast	This paper	V5-tagged SLC1A3 cDNA cloned into pLenti-CMV-Blast; see materials and methods	
Recombinant DNA reagent	lentiCRISPRv2-blasticidin	Addgene	Cat# 83480	
Recombinant DNA reagent	lentiCRISPRv2-hPCg5e-blast	This paper	sgRNA targeting human PC exon 5 in lentiCRISPRv2 vector; see Materials and methods	

Recombinant DNA reagent	lentiCRISPRv2-hPCg6e-blast	This paper	sgRNA targeting human PC exon 6 in lentiCRISPRv2 vector; see Materials and methods	
Recombinant DNA reagent	lentiCRISPRv2-hPEPCK2g2e-blast	This paper	sgRNA targeting human PEPCK2 exon 2 in lentiCRISPRv2 vector; see Materials and methods	
Recombinant DNA reagent	lentiCRISPRv2-hPEPCK2g3e-blast	This paper	sgRNA targeting human PEPCK2 exon 3 in lentiCRISPRv2 vector; see Materials and methods	
Recombinant DNA reagent	lentiCRISPRv2-hGOT2ga-blast	This paper	sgRNA a targeting human GOT2 in lentiCRISPRv2 vector; see Materials and methods	
Recombinant DNA reagent	lentiCRISPRv2-hGOT2gb-blast	This paper	sgRNA b targeting human GOT2 in lentiCRISPRv2 vector; see Materials and methods	
Recombinant DNA reagent	pUAST-aatB-*dGOT2*	This paper	*dGOT2* cDNA was cloned into pLenti-CMV-Blast	
Commercial assay or kit	Annexin V/PI staining kit	Molecular Probes	Cat# V13241	
Commercial assay or kit	Click-iT Plus OPP Alexa Fluor 594 kit	Molecular Probes	Cat# C10457	
Commercial assay or kit	Click-iT HPG Alexa Fluor 594 kit	Molecular Probes	Cat# C10429	
Commercial assay or kit	Triglycerides Reagen	Thermo Fisher Scientific	Cat# TR22421	
Commercial assay or kit	BCA Protein Assay Reagent	Thermo Fisher Scientific	Cat# 23225	

Commercial assay or kit	TRIzol Reagent	Thermo Fisher Scientific	Cat# 15596026	
Commercial assay or kit	Amplite Fluorimetric NAD/NADH ratio assay kit	AAT Bioquest	Cat# 15263	
Commercial assay or kit	Click-iT Plus EdU Alexa Fluor 594	Molecular Probes	Cat# C10639	
Commercial assay or kit	NucleoSpin RNA kit	Takara Bio USA, Inc	Cat# 740955.50	
Commercial assay or kit	Autokit Glucose reagent	Wako	Cat# 997-03001	
Commercial assay or kit	Amplex Red Glucose Assay Kit	Thermo Fisher Scientific	Cat# A22189	
Chemical compound, drug	paraformaldehyde	Sigma Aldrich	Cat# P6148	
Chemical compound, drug	Rhodamine Phalloidin	Thermo Scientific	Cat# R418	
Chemical compound, drug	DAPI-supplemented VectaShield	Vector Labs	Cat# H1200	
Chemical compound, drug	Normal Goat Serum	Jackson ImmunoResearch Laboratories	Cat# 005-000-121	
Chemical compound, drug	Human Plasma-Like Medium	Gibco	Cat# 765090	
Chemical compound, drug	doxycycline	Sigma Aldrich	Cat# #D5207	
Chemical compound, drug	UK5099	Sigma Aldrich	Cat# PZ0160-5MG	
Chemical compound, drug	glycine	Sigma Aldrich	Cat# G7403	
Chemical compound, drug	alanine	Sigma Aldrich	Cat# A7469	
Chemical compound, drug	asparagine	Sigma Aldrich	Cat# A4159	

Chemical compound, drug	aspartic acid	Sigma Aldrich	Cat# A7219	
Chemical compound, drug	glutamic acid	Sigma Aldrich	Cat# G8415	
Chemical compound, drug	proline	Sigma Aldrich	Cat# P5607	
Chemical compound, drug	serine	Sigma Aldrich	Cat# S4311	
Chemical compound, drug	AZD7545	MedChemExpress,	Cat# HY-16082	
Chemical compound, drug	dichloroacetate	Sigma Aldrich	Cat# 347795	
Chemical compound, drug	duroquinone	Sigma Aldrich	Cat# D223204	
Chemical compound, drug	gramicidin	Sigma Aldrich	Cat# G5002	
Chemical compound, drug	nicotinamide riboside	Sigma Aldrich	Cat# SMB00907	
Chemical compound, drug	MEM non-essential amino acids	Gibco	Cat# 11140050	
Chemical compound, drug	Nicotinamide mononucleotide	Sigma Aldrich	Cat# N3501	
Chemical compound, drug	Vybrant® DyeCycle™ Violet stain	Molecular Probes	Cat# V35003	
Chemical compound, drug	Eagle's Minimal Essential Medium	ATCC	Cat# 30-2003	
Chemical compound, drug	Camptothecin	MedChemExpress	Cat# HY-16560	
Chemical compound, drug	Shields Sang M3 Insect Media	Sigma Aldrich	Cat# S8398	
Chemical compound, drug	puromycin	Sigma Aldrich	Cat# P4512	

Chemical compound, drug	methionine-free DMEM	Gibco	Cat# 21013024	
Chemical compound, drug	LipidTOX Red	Invitrogen	Cat# H34351	
Chemical compound, drug	SuperScript II Reverse Transcriptase	Molecular Probes	Cat# 18064-022	
Chemical compound, drug	PowerUp SYBR Green Master Mix	Applied Biosystems	Cat# 2828831	
Chemical compound, drug	^{13}C Glucose	Millipore Sigma	Cat# 389374	
Chemical compound, drug	DMEM, no glucose, no glutamine and no phenol red	Gibco	Cat# A1443001	
Chemical compound, drug	Sodium L-Lactate-C13 solution	Millipore Sigma	Cat# 490040	
Chemical compound, drug	Hepatocyte Plating Medium	Lonza	Cat# MP100	
Chemical compound, drug	Hepatocyte Basal Medium	Lonza	Cat# CC-4182	
Chemical compound, drug	Lipofectamine 3000	Invitrogen	Cat# L3000001	
Chemical compound, drug	Triton X-100	Sigma Aldrich	Cat# X100	
Chemical compound, drug	FBS	Sigma Aldrich	Cat# F0926	
Chemical compound, drug	PenStrep	Thermo Fisher Scientific	Cat# 15140	
Chemical compound, drug	NP-40	Millipore	Cat# 492018	
Chemical compound, drug	sodium deoxycholate	Sigma Aldrich	Cat# D6750	

Chemical compound, drug	SDS	Sigma Aldrich	Cat# L3771	
Chemical compound, drug	EDTA	Sigma Aldrich	Cat# E9884	
Chemical compound, drug	Tris-HCl	Roche	Cat# 10812846001	
Software	FIJI	NIH Image	RRID: SCR_002285	https://fiji.sc/
Software	Prism	GraphPad	RRID:SCR_002798	http://www.graphpad.com/
Software	FlowJo	FlowJo	RRID: SCR_008520	https://www.flowjo.com/solutions/flowjo/downloads
other	Ultra Low Cluster, 96 well, Ultra Low Attachment Polystyrene	Costar	Cat# 7007	
other	Dumont 5 forceps	Fine Science Tools	Cat# 11254-20	

1687

1688

Table 2-Oligos for *Drosophila* genes

1690

Name of gene	Sequence	Additional Information
rp49	GACGCTTCAAGGGA CAGTATCTG	QPCR- forward primer
rp49	AAACGCGGTTCTGCATGA	QPCR- reverse primer
Pyk	TCTTGGTGACTGGCTGAAGG	QPCR- forward primer
Pyk	GCCGTTCTTCTTTCCGAC	QPCR- reverse primer
Mpc1	CTCAAAGGAGTGGCGGGATT	QPCR- forward primer
Mpc1	CAGGGTCAGAGCCAATGTCA	QPCR- reverse primer
Mpc2	CAGCTGGTCCCAAGACGATA	QPCR- forward primer
Mpc2	CGCATCCAGACACGGAGAT	QPCR- reverse primer

Pdha	ATCATCTCGGCGTACCGTG	QPCR- forward primer
Pdha	GCCTCCGTAGAAGTTCGGTG	QPCR- reverse primer
Dlat	CTGGAGTCCAAGACACAACTG	QPCR- forward primer
Dlat	TGAAGTCGTTTACAGAGACGC	QPCR- reverse primer
Pepck	TGATCCCGAACGCACCATC	QPCR- forward primer
Pepck	CTCAGGGCGAAGCACTTCTT	QPCR- reverse primer
Pepck2	AATGCTGGGTAACTGGATAGCC	QPCR- forward primer
Pepck2	GGTGCGACCTTTCATGCAG	QPCR- reverse primer
Pc-KO	ATACATTTAAGTCCTAGGC	CRISPR 5' guide
Pc-KO	TCGATTGATCCTGGAAACA	CRISPR 3' guide
Pepck2-KO	AAAGGGTGCACATCTGTGA	CRISPR 5' guide
Pepck2-KO	TTTGGGGCGTGGCCTAGAC	CRISPR 3' guide
Got2	GAATTC ATGAGTAGAACCATTATTATGACGCTTAAGGAC	Primer for cDNA clone
Got2	CTCGAG CTTGGTAACCTTGTGTATGCTCTCAGCCAGG	Primer for cDNA clone

1691

Table 3-Oligos for human genes

1693

Name of gene	Sequence	Additional Information
PC	GAATTC ATGCTGAAGTTCCGAACAGTCCATGGG	Forward Primer for cDNA clone
PC	GGATCC CTCGATCTCCAGGATGAGGTCGTCACC	Reverse Primer for cDNA clone
SLC1A3	GGATCC ATGACTAAAAGCAATGGAGAAGAGC	Forward Primer for cDNA clone
SLC1A3	CTACATCTTGGTTTCAATGTCGATGG	Reverse Primer for cDNA clone
GOT2	GGATCC ATGGCCCTGCTGCACTCCGG	Forward Primer for cDNA clone
GOT2	TCTAGA CTTGGTGACCTGGTGAATGGCATGG	Reverse Primer for cDNA clone
PC	GAAGCCTATCTCATCGGCCG *CGG*	CRISPR guide targeting exon 5
PC	CGAAGTCCGCTCGCTCAGAG *AGG*	CRISPR guide targeting exon 6

PEPCK2	ATCTCCACTAAGCACTCGCA *GGG*	CRISPR guide targeting exon 2
PEPCK2	CATGCGTATTATGACCCGAC *TGG*	CRISPR guide targeting exon 3
GOT2	GAGTGGCCGGGTAAGCTGAGCAG *AGG*	CRISPR guide a
GOT2	GGAGTGGACCCGCTCCGGAACAG *TGG*	CRISPR guide b

1694

1695

Fly genotypes

Figure 1

#	acronym	Detailed genotype
b-d	*w^{1118}*	*w^{1118}*
f	Control	*hs-Flp 1.22; +/+; act>CD2>Gal4, UAS-GFP/+*
	MPC+	*hs-Flp 1.22; UAS-MPC1-P2A-MPC2/+; act>CD2>Gal4, UAS-GFP/+*
g	Control	*hs-Flp 1.22; +/+; act>CD2>Gal4, UAS-GFP/+*
	MPC+	*hs-Flp 1.22; UAS-MPC1-P2A-MPC2/+; act>CD2>Gal4, UAS-GFP/+*
	Mpc1-KD	*hs-Flp 1.22; UAS-Mpc1^{RNAi}/+; act>CD2>Gal4, UAS-GFP/+*
h	Control	*hs-Flp 1.22; +/+; act>CD2>Gal4, UAS-GFP/+*
	MPC+	*hs-Flp 1.22; UAS-MPC1-P2A-MPC2/+; act>CD2>Gal4, UAS-GFP/+*
I	Control	*hs-Flp 1.22; +/+; act>CD2>Gal4, UAS-GFP/+*
	MPC+	*hs-Flp 1.22; UAS-MPC1-P2A-MPC2/+; act>CD2>Gal4, UAS-GFP/+*
	Mpc1-KD	*hs-Flp 1.22; UAS-Mpc1^{RNAi}/+; act>CD2>Gal4, UAS-GFP/+*
j	Control	*hs-Flp 1.22; +/+; act>CD2>Gal4, UAS-GFP/+*
	MPC+	*hs-Flp 1.22; UAS-MPC1-P2A-MPC2/+; act>CD2>Gal4, UAS-GFP/+*
k	Control	*y, w; CG-Gal4/UAS-GFP; tubGal^{80ts20}/+*
	MPC+	*y, w; CG-Gal4/ UAS-MPC1-P2A-MPC2; tubGal^{80ts20}/+*
l&m	Control	*hs-Flp 1.22; +/+; act>CD2>Gal4, UAS-GFP/+*
	MPC+	*hs-Flp 1.22; UAS-MPC1-P2A-MPC2/+; act>CD2>Gal4, UAS-GFP/+*

1698

Supplementary Figure 1

#	acronym	Detailed genotype
a-c	*w^{1118}*	*w^{1118}*

1700

Supplementary Figure 2

#	acronym	Detailed genotype
b&c.	Control	*y, w; CG-Gal4/UAS-GFP; tubGal^{80ts20}/+*
	MPC+	*y, w; CG-Gal4/ UAS-MPC1-P2A-MPC2; tubGal^{80ts20}/+*
e&f	MPC+	*hs-Flp 1.22; UAS-MPC1-P2A-MPC2/+; act>CD2>Gal4, UAS-GFP/+*
g	Control	*hs-Flp 1.22; +/+; act>CD2>Gal4, UAS-GFP/+*
	MPC+	*hs-Flp 1.22; UAS-MPC1-P2A-MPC2/+; act>CD2>Gal4, UAS-GFP/+*
h-k	Control	*y, w; CG-Gal4/UAS-GFP; tubGal^{80ts20}/+*
	MPC+	*y, w; CG-Gal4/ UAS-MPC1-P2A-MPC2; tubGal^{80ts20}/+*
l-n	Control	*hs-Flp 1.22; +/+; act>CD2>Gal4, UAS-GFP/+*
	MPC+	*hs-Flp 1.22; UAS-MPC1-P2A-MPC2/+; act>CD2>Gal4, UAS-GFP/+*
o&p	Control	*hs-Flp 1.22; +/+; act>CD2>Gal4, UAS-GFP/+*
	MPC+	*hs-Flp 1.22; UAS-MPC1-P2A-MPC2/+; act>CD2>Gal4, UAS-GFP/+*

1702

1703 **Figure 2**

#	acronym	Detailed genotype
b&c	S6K+	*hs-Flp 1.22; UAS-S6K^{STDETE}/+; act>CD2>Gal4, UAS-GFP/+*
	Control	*hs-Flp 1.22; +/+; act>CD2>Gal4, UAS-GFP/+*
	MPC+	*hs-Flp 1.22; UAS-MPC1-P2A-MPC2/+; act>CD2>Gal4, UAS-GFP/+*
d&e	Rheb+	*hs-Flp 1.22; +/+; act>CD2>Gal4, UAS-GFP/ UAS-Rheb^{PA}*
	Control	*hs-Flp 1.22; +/+; act>CD2>Gal4, UAS-GFP/+*
	MPC+	*hs-Flp 1.22; UAS-MPC1-P2A-MPC2/+; act>CD2>Gal4, UAS-GFP/+*
f&g	*Myc*-KD	*hs-Flp 1.22; +/+; act>CD2>Gal4, UAS-GFP/ UAS-Myc^{RNAi}*
	Control	*hs-Flp 1.22; +/+; act>CD2>Gal4, UAS-GFP/+*
	MPC+	*hs-Flp 1.22; UAS-MPC1-P2A-MPC2/+; act>CD2>Gal4, UAS-GFP/+*
h&i	Control	*hs-Flp 1.22; +/+; act>CD2>Gal4, UAS-GFP/+*
	MPC+	*hs-Flp 1.22; UAS-MPC1-P2A-MPC2/+; act>CD2>Gal4, UAS-GFP/+*

1704

1705 **Supplementary Figure 3**

#	acronym	Detailed genotype
a	Control	*y, w; CG-Gal4/UAS-GFP; tubGal^{80ts20}/+*
	MPC+	*y, w; CG-Gal4/ UAS-MPC1-P2A-MPC2; tubGal^{80ts20}/+*
b	PI3K-DN	*hs-Flp 1.22; +/+; act>CD2>Gal4, UAS-GFP/ UAS-Pi3K92E.A2860C*
	Control	*hs-Flp 1.22; +/+; act>CD2>Gal4, UAS-GFP/+*
	MPC+	*hs-Flp 1.22; UAS-MPC1-P2A-MPC2/+; act>CD2>Gal4, UAS-GFP/+*
c	Control	*hs-Flp 1.22; +/+; act>CD2>Gal4, UAS-GFP/+*
	MPC+	*hs-Flp 1.22; UAS-MPC1-P2A-MPC2/+; act>CD2>Gal4, UAS-GFP/+*
	PI3K+	*hs-Flp 1.22; +/+; act>CD2>Gal4, UAS-GFP/ UAS-PI3K93E$^{.Excel}$*
	MPC+, *PI3K+*	*hs-Flp 1.22; UAS-MPC1-P2A-MPC2/+; act>CD2>Gal4, UAS-GFP/ UAS-PI3K93E$^{.Excel}$*
d	Control	*hs-Flp 1.22; +/+; act>CD2>Gal4, UAS-GFP/+*
	MPC+	*hs-Flp 1.22; UAS-MPC1-P2A-MPC2/+; act>CD2>Gal4, UAS-GFP/+*
	Tsc1-KD	*hs-Flp 1.22; +/+; act>CD2>Gal4, UAS-GFP/ UAS-Tsc1^{RNAi}*
	MPC+, *Tsc1*-KD	*hs-Flp 1.22; UAS-MPC1-P2A-MPC2/+; act>CD2>Gal4, UAS-GFP/ UAS-Tsc1^{RNAi}*
e	Control	*hs-Flp 1.22; +/+; act>CD2>Gal4, UAS-GFP/+*
	MPC+	*hs-Flp 1.22; UAS-MPC1-P2A-MPC2/+; act>CD2>Gal4, UAS-GFP/+*
	Myc+	*hs-Flp 1.22; +/+; act>CD2>Gal4, UAS-GFP/ UAS-Myc*
	MPC+, *Myc+*	*hs-Flp 1.22; UAS-MPC1-P2A-MPC2/+; act>CD2>Gal4, UAS-GFP/ UAS-Myc*
f	Control	*hs-Flp 1.22; +/+; act>CD2>Gal4, UAS-GFP/+*
	MPC+	*hs-Flp 1.22; UAS-MPC1-P2A-MPC2/+; act>CD2>Gal4, UAS-GFP/+*
	Myc-KD	*hs-Flp 1.22; +/+; act>CD2>Gal4, UAS-GFP/ UAS-Myc^{RNAi}*
	MPC+, *Myc*-KD	*hs-Flp 1.22; UAS-MPC1-P2A-MPC2/+; act>CD2>Gal4, UAS-GFP/ UAS-Myc^{RNAi}*

1706

1707 **Figure 4**

#	acronym	Detailed genotype
e	MPC+	*hs-Flp 1.22; UAS-MPC1-P2A-MPC2/+; act>CD2>Gal4, UAS-GFP/+*
	MPC+, *Pcb*-KD	*hs-Flp 1.22; UAS-MPC1-P2A-MPC2/+; act>CD2>Gal4, UAS-GFP/ UAS- -Pcb^{RNAi}*

	Pcb+	*hs-Flp 1.22; +/+; act>CD2>Gal4, UAS-GFP/ UAS-hPC*
f	Control	*hs-Flp 1.22; +/+; act>CD2>Gal4, UAS-GFP/+*
	MPC+	*hs-Flp 1.22; UAS-MPC1-P2A-MPC2/+; act>CD2>Gal4, UAS-GFP/+*
	Pcb+	*hs-Flp 1.22; +/+; act>CD2>Gal4, UAS-GFP/ UAS-hPC*
	MPC+, *Pcb*+	*hs-Flp 1.22; UAS-MPC1-P2A-MPC2/+; act>CD2>Gal4, UAS-GFP/ UAS-hPC*
	Pcb-KD	*hs-Flp 1.22; +/+; act>CD2>Gal4, UAS-GFP/ UAS-Pcb^{RNAi}*
	MPC+, *Pcb*-KD	*hs-Flp 1.22; UAS-MPC1-P2A-MPC2/+; act>CD2>Gal4, UAS-GFP/ UAS--Pcb^{RNAi}*
g&h	Control	*y, w; CG-Gal4/UAS-GFP; tubGal^{80ts20}/+*
	MPC+	*y, w; CG-Gal4/ UAS-MPC1-P2A-MPC2; tubGal^{80ts20}/+*
n	MPC+	*hs-Flp 1.22; UAS-MPC1-P2A-MPC2/+; act>CD2>Gal4, UAS-GFP/+*
	MPC+, *Pepck2*-KD	*hs-Flp 1.22; UAS-MPC1-P2A-MPC2/+; act>CD2>Gal4, UAS-GFP/UAS-Pepck2^{RNAi}*
o	Control	*hs-Flp 1.22; +/+; act>CD2>Gal4, UAS-GFP/+*
	MPC+	*hs-Flp 1.22; UAS-MPC1-P2A-MPC2/+; act>CD2>Gal4, UAS-GFP/+*
	Pepck2-KD	*hs-Flp 1.22; +/+; act>CD2>Gal4, UAS-GFP/UAS-Pepck2^{RNAi}*
	MPC+, *Pepck2*-KD	*hs-Flp 1.22; UAS-MPC1-P2A-MPC2/+; act>CD2>Gal4, UAS-GFP/UAS-Pepck2^{RNAi}*
	Fbp-KD	*hs-Flp 1.22; +/+; act>CD2>Gal4, UAS-GFP/UAS-Fbp^{RNAi}*
	MPC+, *Fbp*-KD	*hs-Flp 1.22; UAS-MPC1-P2A-MPC2/+; act>CD2>Gal4, UAS-GFP/UAS-Fbp2^{RNAi}*
p	MPC+	*hs-Flp 1.22; UAS-MPC1-P2A-MPC2/+; act>CD2>Gal4, UAS-GFP/+*
	MPC+, *Pcb*-KD	*hs-Flp 1.22; UAS-MPC1-P2A-MPC2/+; act>CD2>Gal4, UAS-GFP/ UAS-Pcb^{RNAi}*
	MPC+, *Pepck2*-KD	*hs-Flp 1.22; UAS-MPC1-P2A-MPC2/+; act>CD2>Gal4, UAS-GFP/UAS-Pepck2^{RNAi}*
q	Control	*hs-Flp 1.22; +/+; act>CD2>Gal4, UAS-GFP/+*
	MPC+	*hs-Flp 1.22; UAS-MPC1-P2A-MPC2/+; act>CD2>Gal4, UAS-GFP/+*
	Pcb-KD	*hs-Flp 1.22; +/+; act>CD2>Gal4, UAS-GFP/ UAS-Pcb^{RNAi}*
	MPC+, *Pcb*-KD	*hs-Flp 1.22; UAS-MPC1-P2A-MPC2/+; act>CD2>Gal4, UAS-GFP/ UAS-Pcb^{RNAi}*
	Pepck2-KD	*hs-Flp 1.22; +/+; act>CD2>Gal4, UAS-GFP/UAS-Pepck2^{RNAi}*
	MPC+, *Pepck2*-KD	*hs-Flp 1.22; UAS-MPC1-P2A-MPC2/+; act>CD2>Gal4, UAS-GFP/UAS-Pepck2^{RNAi}*

1708

1709 **Supplementary Figure 6**

#	acronym	Detailed genotype
a	Control	*hs-Flp 1.22; +/+; act>CD2>Gal4, UAS-GFP/+*
	MPC+	*hs-Flp 1.22; UAS-MPC1-P2A-MPC2/+; act>CD2>Gal4, UAS-GFP/+*
	Pcb-KO	*hs-Flp 1.22; Pcb-KO/+; act>CD2>Gal4, UAS-GFP/+*

	MPC+, *Pcb*-KO	*hs-Flp 1.22; UAS-MPC1-P2A-MPC2/ Pcb-KO; act>CD2>Gal4, UAS-GFP/+*
c	MPC+	*hs-Flp 1.22; UAS-MPC1-P2A-MPC2/+; act>CD2>Gal4, UAS-GFP/+*
	Pdha-KD	*hs-Flp 1.22; UAS-Pdha^{RNAi} /+; act>CD2>Gal4, UAS-GFP/ UAS-hPC*
	MPC+, *Pdk*-KD	*hs-Flp 1.22; UAS-MPC1-P2A-MPC2/+; act>CD2>Gal4, UAS-GFP/ UAS-Pdk^{RNAi}*
d	Control	*hs-Flp 1.22; +/+; act>CD2>Gal4, UAS-GFP/+*
	MPC+	*hs-Flp 1.22; UAS-MPC1-P2A-MPC2/+; act>CD2>Gal4, UAS-GFP/+*
	Pdha-KD	*hs-Flp 1.22; UAS-Pdha^{RNAi} /+; act>CD2>Gal4, UAS-GFP/ UAS-hPC*
	MPC+, *Pdha*-KD	*hs-Flp 1.22; UAS-MPC1-P2A-MPC2/ UAS-Pdha^{RNAi}; act>CD2>Gal4, UAS-GFP/+*
	Dlat-KD	*hs-Flp 1.22; UAS-Dlat^{RNAi} /+; act>CD2>Gal4, UAS-GFP/ UAS-hPC*
	MPC+, *Dlat*-KD	*hs-Flp 1.22; UAS-MPC1-P2A-MPC2/ UAS-Dlat^{RNAi}; act>CD2>Gal4, UAS-GFP/+*
	Pdk-KD	*hs-Flp 1.22; +/+; act>CD2>Gal4, UAS-GFP/ UAS-Pdk^{RNAi}*
	MPC+, *Pdk*-KD	*hs-Flp 1.22; UAS-MPC1-P2A-MPC2/+; act>CD2>Gal4, UAS-GFP/ UAS-Pdk^{RNAi}*

1710

1711 **Figure 5**

#	acronym	Detailed genotype
a	Control	*y, w; CG-Gal4/UAS-GFP; tubGal^{80ts20}/+*
	MPC+	*y, w; CG-Gal4/ UAS-MPC1-P2A-MPC2; tubGal^{80ts20}/+*
c	MPC+	*hs-Flp 1.22; UAS-MPC1-P2A-MPC2/+; act>CD2>Gal4, UAS-GFP/+*
	MPC+, *Nmnat*+	*hs-Flp 1.22; UAS-MPC1-P2A-MPC2/ UAS-Nmnat; act>CD2>Gal4, UAS-GFP/+*
d	Control	*hs-Flp 1.22; +/+; act>CD2>Gal4, UAS-GFP/+*
	MPC+	*hs-Flp 1.22; UAS-MPC1-P2A-MPC2/+; act>CD2>Gal4, UAS-GFP/+*
	Nmnat+	*hs-Flp 1.22; UAS-Nmnat/+; act>CD2>Gal4, UAS-GFP/+*
	MPC+, *Nmnat*+	*hs-Flp 1.22; UAS-MPC1-P2A-MPC2/ UAS-Nmnat; act>CD2>Gal4, UAS-GFP/+*
e	MPC+	*hs-Flp 1.22; UAS-MPC1-P2A-MPC2/+; act>CD2>Gal4, UAS-GFP/+*
	MPC+, NDI+	*hs-Flp 1.22; UAS-MPC1-P2A-MPC2/+; act>CD2>Gal4, UAS-GFP/ UAS-NDI*
	MPC+, NDX+	*hs-Flp 1.22; UAS-MPC1-P2A-MPC2/+; act>CD2>Gal4, UAS-GFP/ UAS-NDX*
f	Control	*hs-Flp 1.22; +/+; act>CD2>Gal4, UAS-GFP/+*
	MPC+	*hs-Flp 1.22; UAS-MPC1-P2A-MPC2/+; act>CD2>Gal4, UAS-GFP/+*
	NDI+	*hs-Flp 1.22; +/+; act>CD2>Gal4, UAS-GFP/ UAS-NDI*
	MPC+, NDI+	*hs-Flp 1.22; UAS-MPC1-P2A-MPC2/+; act>CD2>Gal4, UAS-GFP/ UAS-NDI*
	NDX+	*hs-Flp 1.22; +/+; act>CD2>Gal4, UAS-GFP/ UAS-NDX*
	MPC+, NDX+	*hs-Flp 1.22; UAS-MPC1-P2A-MPC2/+; act>CD2>Gal4, UAS-GFP/ UAS-NDX*
i	MPC+	*hs-Flp 1.22; UAS-MPC1-P2A-MPC2/+; act>CD2>Gal4, UAS-GFP/+*
	MPC+, NDX+	*hs-Flp 1.22; UAS-MPC1-P2A-MPC2/+; act>CD2>Gal4, UAS-GFP/ UAS-NDX*
j	Control	*hs-Flp 1.22; +/+; act>CD2>Gal4, UAS-GFP/+*

	MPC+	*hs-Flp 1.22; UAS-MPC1-P2A-MPC2/+; act>CD2>Gal4, UAS-GFP/+*
	NDX+	*hs-Flp 1.22; +/+; act>CD2>Gal4, UAS-GFP/ UAS-NDX*
	MPC+, NDX+	*hs-Flp 1.22; UAS-MPC1-P2A-MPC2/+; act>CD2>Gal4, UAS-GFP/ UAS-NDX*

1712

1713 **Figure 6**

#	acronym	Detailed genotype
d	MPC+	*hs-Flp 1.22; UAS-MPC1-P2A-MPC2/+; act>CD2>Gal4, UAS-GFP/+*
e	Control	*hs-Flp 1.22; +/+; act>CD2>Gal4, UAS-GFP/+*
	MPC+	*hs-Flp 1.22; UAS-MPC1-P2A-MPC2/+; act>CD2>Gal4, UAS-GFP/+*
f	MPC+	*hs-Flp 1.22; UAS-MPC1-P2A-MPC2/+; act>CD2>Gal4, UAS-GFP/+*
	MPC+, *slif*+	*hs-Flp 1.22; UAS-MPC1-P2A-MPC2/+; act>CD2>Gal4, UAS-GFP/ UAS-slif*
g	Control	*hs-Flp 1.22; +/+; act>CD2>Gal4, UAS-GFP/+*
	MPC+	*hs-Flp 1.22; UAS-MPC1-P2A-MPC2/+; act>CD2>Gal4, UAS-GFP/+*
	slif+	*hs-Flp 1.22; +/+; act>CD2>Gal4, UAS-GFP/ UAS-slif*
	MPC+, *slif*+	*hs-Flp 1.22; UAS-MPC1-P2A-MPC2/+; act>CD2>Gal4, UAS-GFP/ UAS-slif*
i	MPC+	*hs-Flp 1.22; UAS-MPC1-P2A-MPC2/+; act>CD2>Gal4, UAS-GFP/+*
	Got2-KD	*hs-Flp 1.22; +/+; act>CD2>Gal4, UAS-GFP/ UAS-Got2^{RNAi}*
	MPC+, *Got2*+	*hs-Flp 1.22; UAS-MPC1-P2A-MPC2/+; act>CD2>Gal4, UAS-GFP/UAS-Got2*
j	Control	*hs-Flp 1.22; +/+; act>CD2>Gal4, UAS-GFP/+*
	MPC+	*hs-Flp 1.22; UAS-MPC1-P2A-MPC2/+; act>CD2>Gal4, UAS-GFP/+*
	Got2-KD	*hs-Flp 1.22; +/+; act>CD2>Gal4, UAS-GFP/ UAS-Got2^{RNAi}*
	MPC+, *Got2*-KD	*hs-Flp 1.22; UAS-MPC1-P2A-MPC2/+; act>CD2>Gal4, UAS-GFP/ UAS-Got2^{RNAi}*
	Got2+	*hs-Flp 1.22; +/+; act>CD2>Gal4, UAS-GFP/UAS- Got2*+
	MPC+, *Got2*+	*hs-Flp 1.22; UAS-MPC1-P2A-MPC2/+; act>CD2>Gal4, UAS-GFP/UAS-Got2*+

1714
1715
1716
1717
1718
1719
1720
1721
1722
1723
1724
1725
1726
1727
1728
1729

Author Information

Ashish G. Toshniwal

Department of Biochemistry, The University of Utah, Salt Lake City, United States

Contribution

Conceptualization, Data curation, Formal analysis, Validation, Investigation, Visualization, Methodology, Writing – original draft, Writing – review and editing

0000-0001-8957-7970

ashish.toshniwal@biochem.utah.edu

Geanette Lam

Department of Biochemistry, The University of Utah, Salt Lake City, United States

Contribution

Methodology

Ahmad A Cluntun

Department of Biochemistry, The University of Utah, Salt Lake City, United States

Contribution

Investigation, Methodology

0000-0001-7612-8375

Present address: Department of Biochemistry & Molecular Biology, Rutgers Robert Wood Johnson Medical School, Piscataway, NJ 08854

Ahmad.cluntun@rutgers.edu

Alex J. Bott

Department of Biochemistry, The University of Utah, Salt Lake City, United States

Contribution

Investigation, Methodology

0000-0003-2273-8922

Hyuck-Jin Nam

Department of Human Genetics, University of Utah, Salt Lake City, UT 84132, USA

Contribution

Methodology

hjin@genetics.utah.edu

0000-0002-9489-6439

Rachel Skabelund

Department of Biochemistry, The University of Utah, Salt Lake City, United States

Contribution

Methodology

rachel.skabelund@biochem.utah.edu

0000-0001-6533-8887

Dona R. Wisidagama,

Department of Human Genetics, University of Utah, Salt Lake City, UT 84132, USA

Contribution

Investigation

roonalika@gmail.com

0009-0002-7029-3294

Carl S. Thummel
Department of Human Genetics, University of Utah, Salt Lake City, UT 84132, USA
Contribution
Conceptualization, Resources, Supervision, Funding acquisition, Writing – review and editing
cthummel@genetics.utah.edu
0000-0001-8112-4643

Jared Rutter
1. Department of Biochemistry, The University of Utah, Salt Lake City, United States
2. Howard Hughes Medical Institute, University of Utah, Salt Lake City, United States
Contribution
Conceptualization, Resources, Supervision, Funding acquisition, Writing – original draft, Project administration, Writing – review and editing
Lead contact
0000-0002-2710-9765
Rutter@biochem.utah.edu

Figure 1: Increased mitochondrial pyruvate transport reduces size of *Drosophila* fat body cells

Figure 2 – mTORC1 and Myc pathways are hyperactivated in MPC expressing fat body cells.
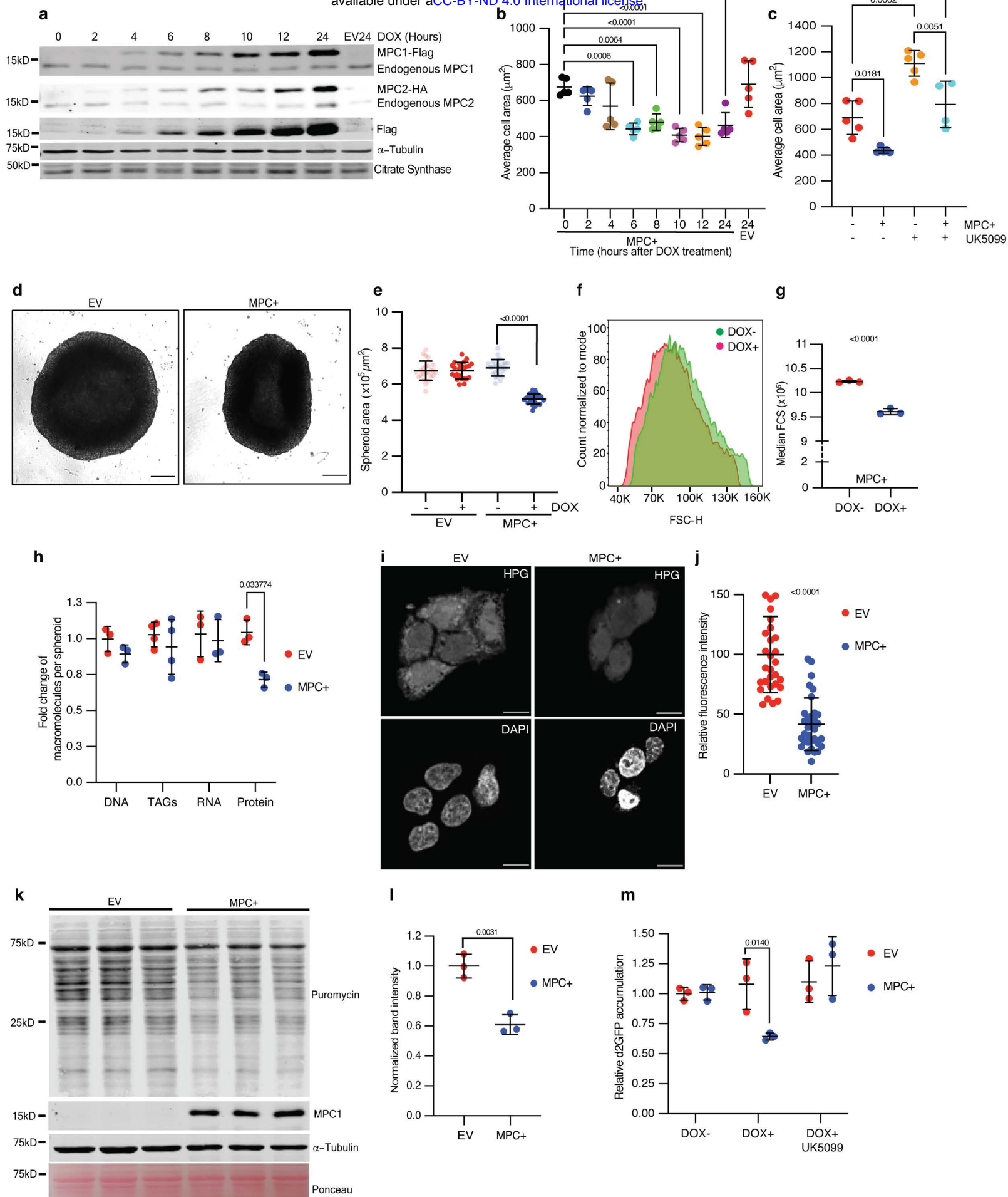
Figure 3 – Increased mitochondrial pyruvate transport reduces size of HepG2 spheroids.
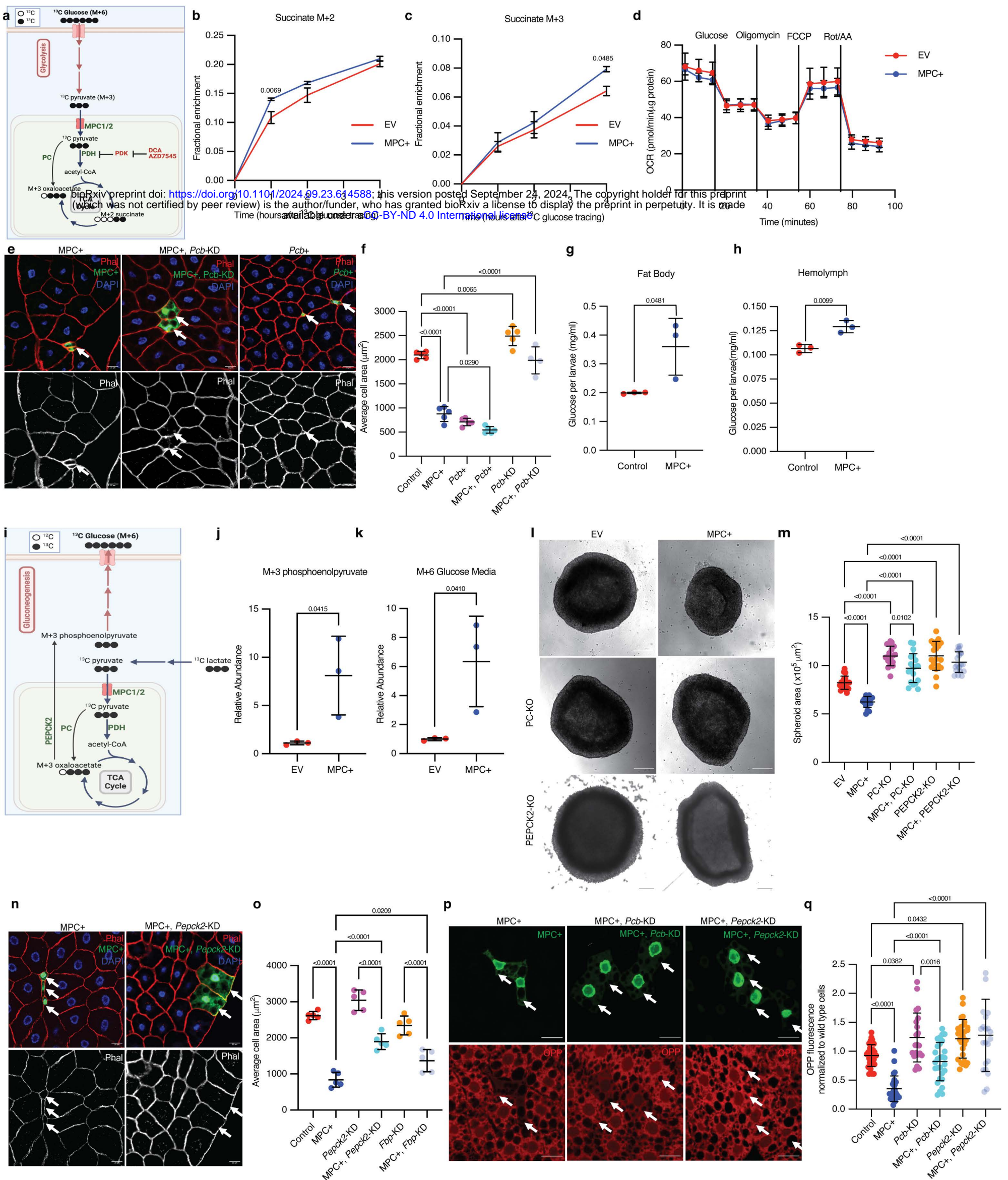
Figure 4: Increased mitochondrial pyruvate metabolism promotes gluconeogenesis via pyruvate carboxylase to suppress protein synthesis
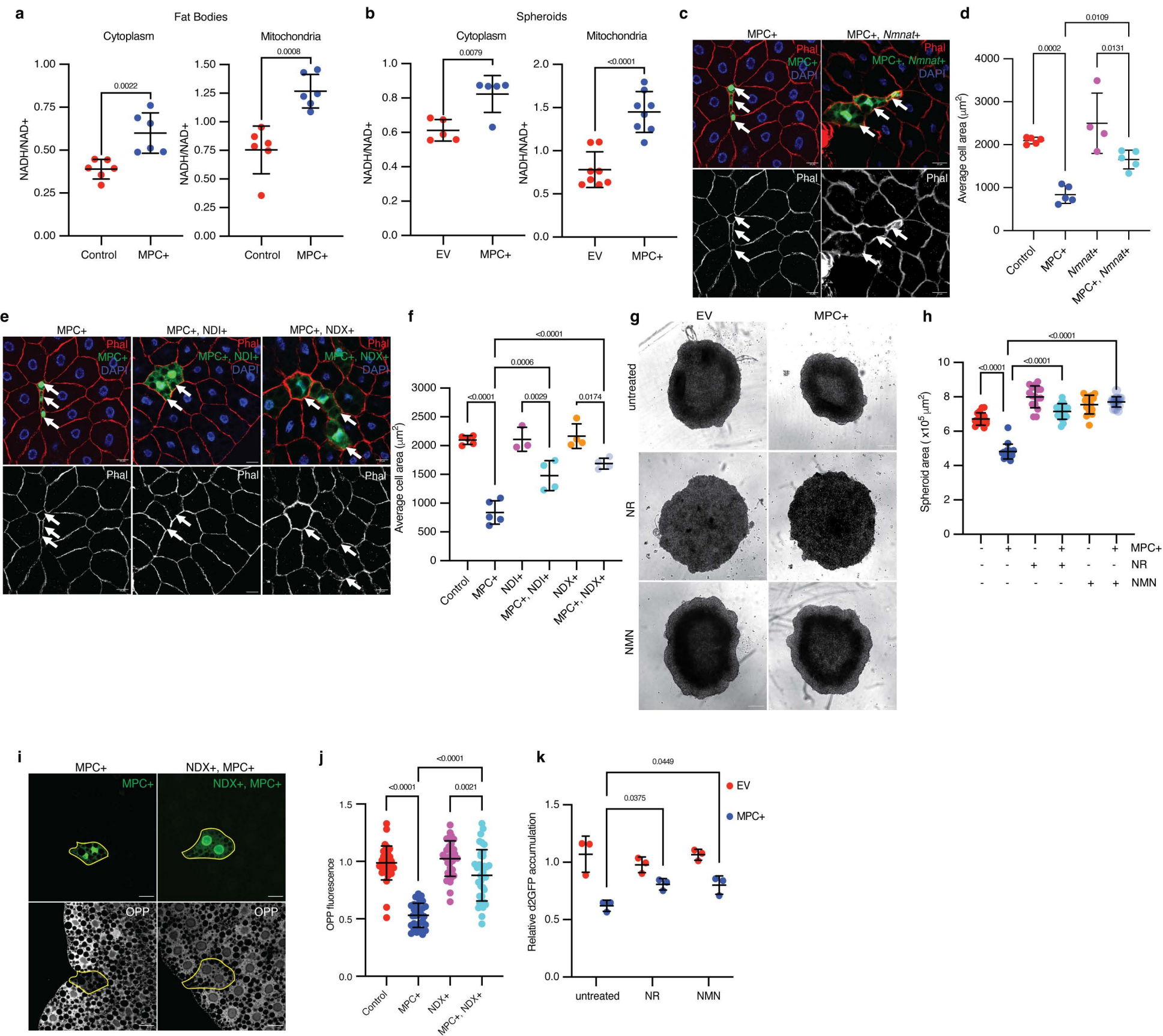
Figure 5 – Redox imbalance impedes protein synthesis and cell growth from elevated pyruvate metabolism in mitochondria.
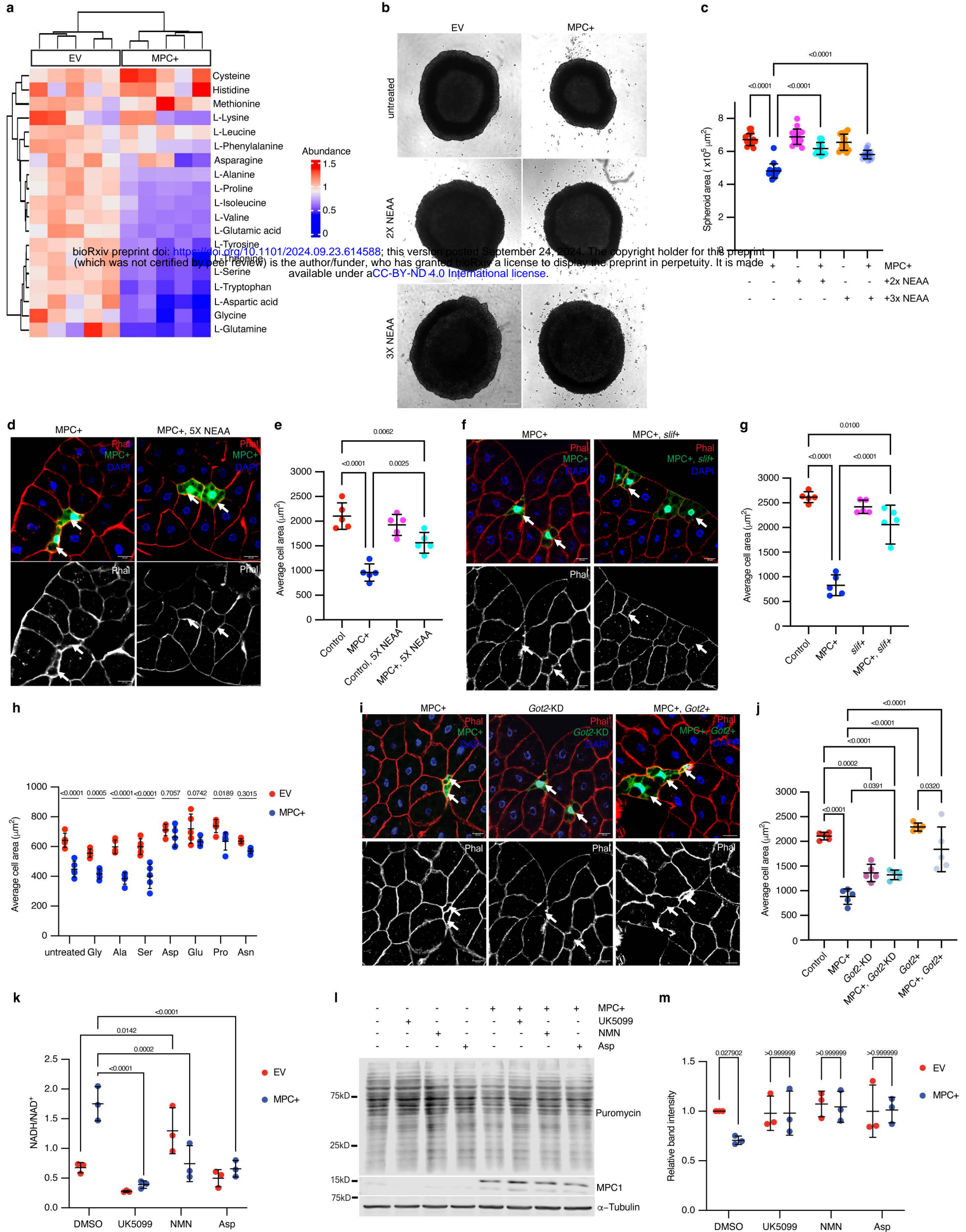
Figure 6 – Reduced amino acid abundance impairs size of MPC-expressing cells
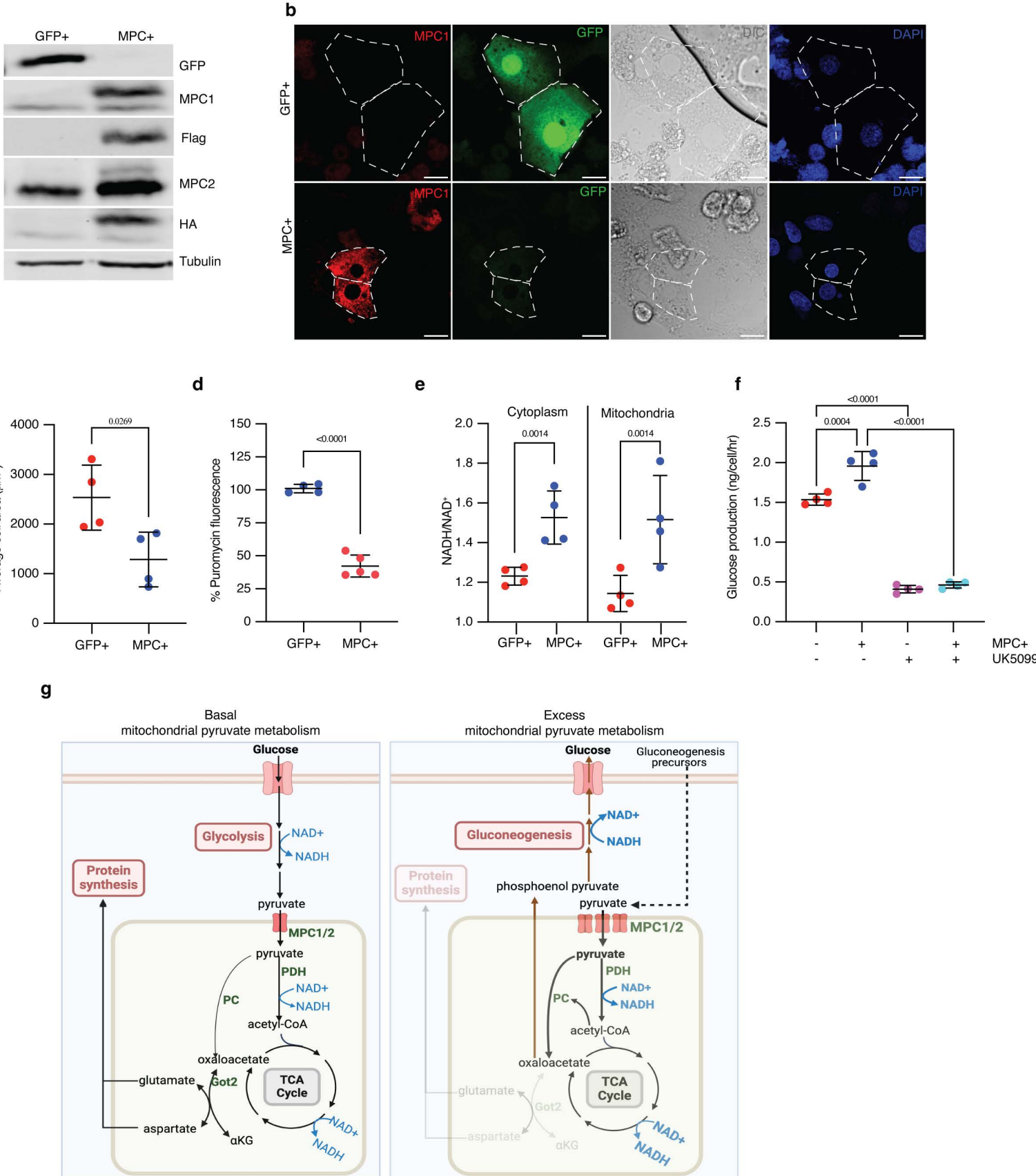
Figure 7– Increased mitochondrial pyruvate transport rewires metabolism and redox status to reduce protein synthesis and cell size in rat primary hepatocytes
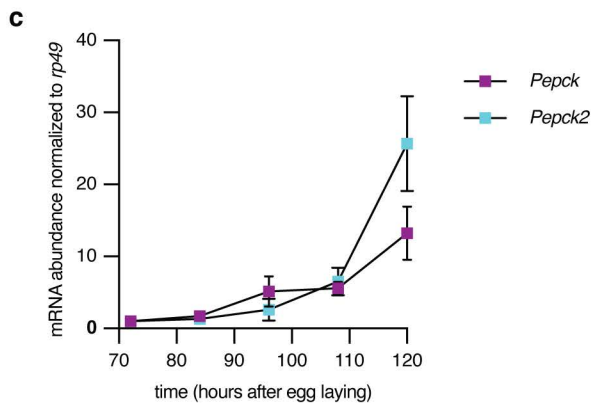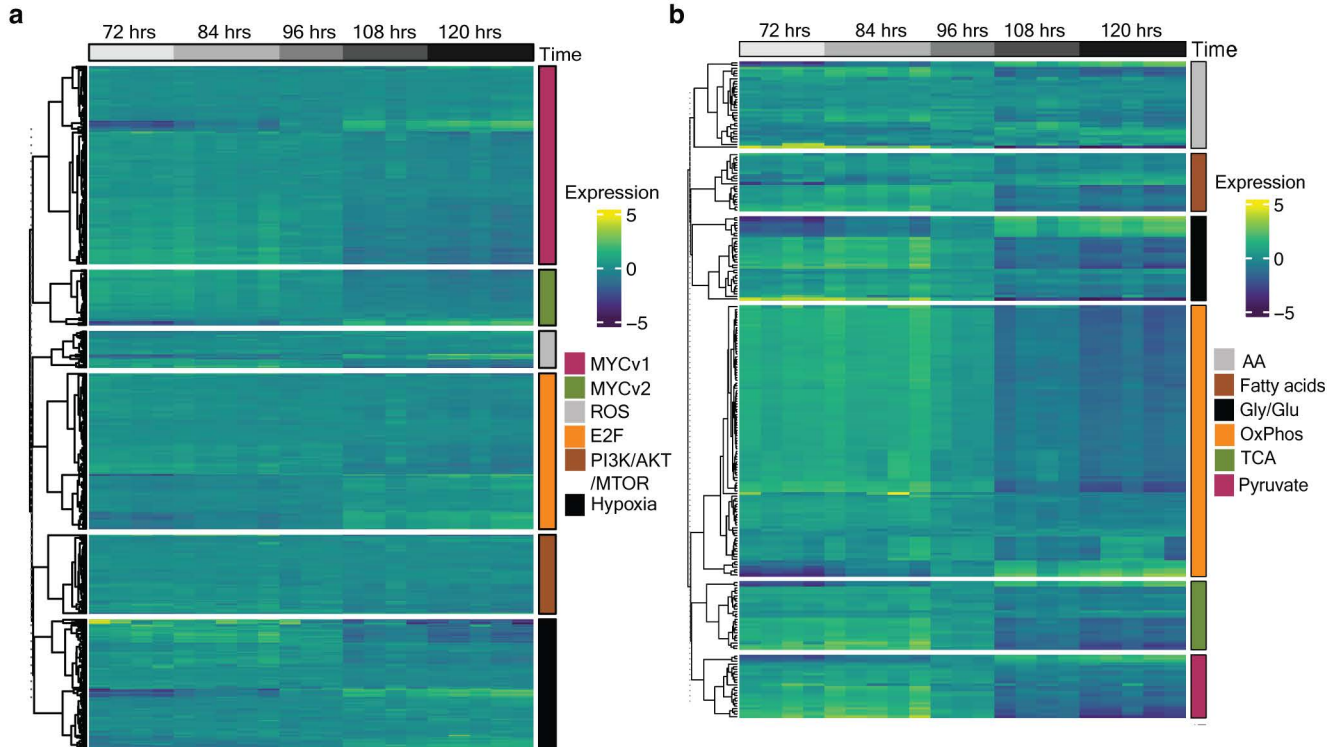
Supplementary Figure 1 – Transcriptomic changes in fat body during larval development (related to Main Figure 1)
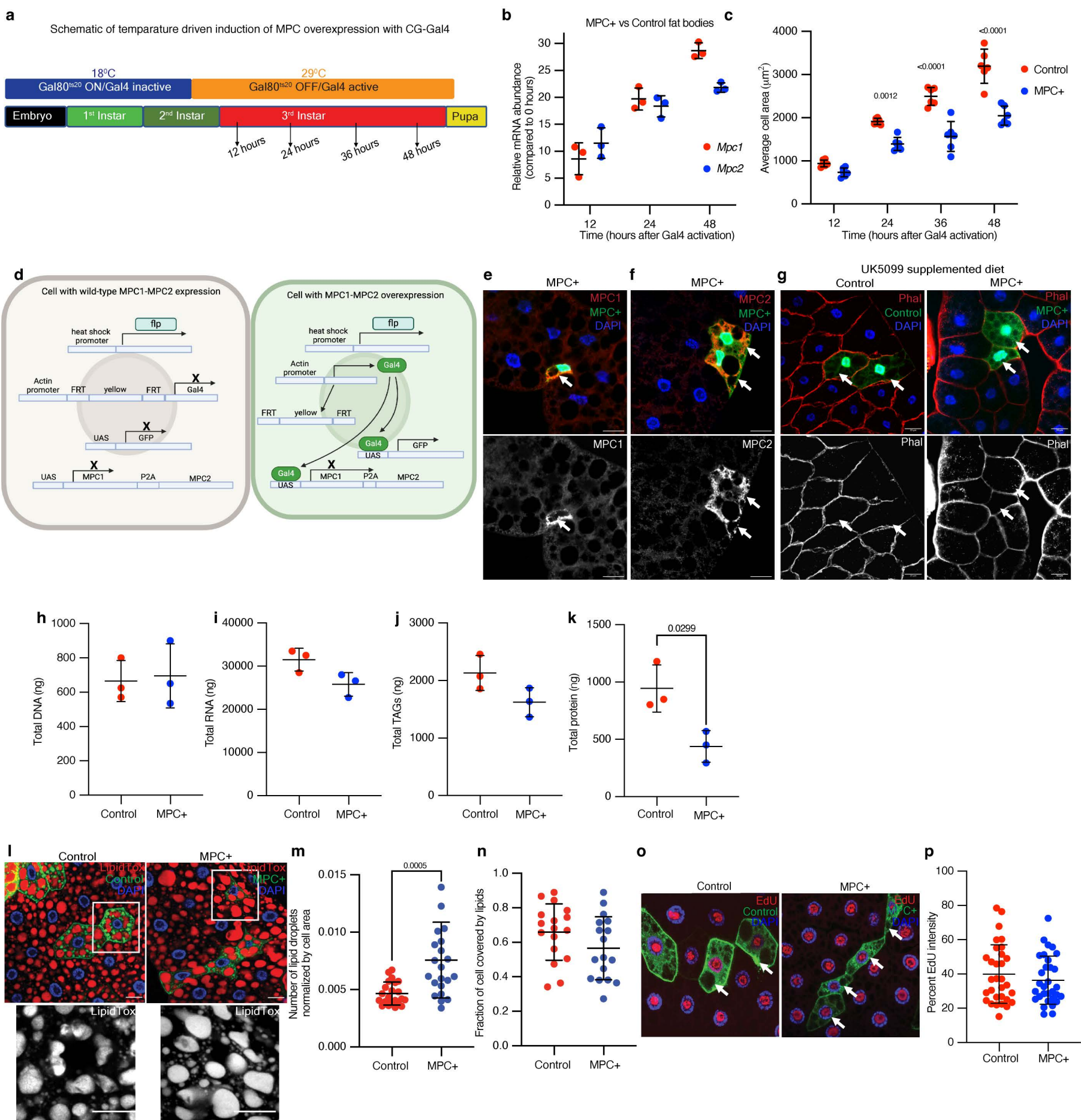
**Supplementary Figure 2 – MPC expression reduces size of *Drosophila* fat body cells. (related to Main Figure 1)**
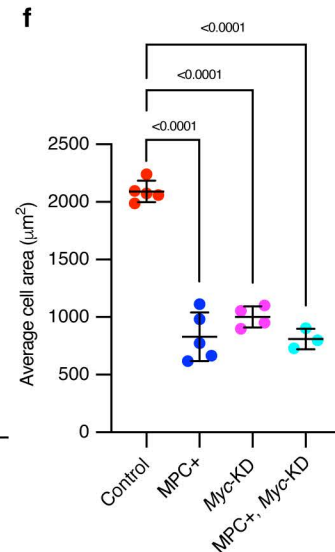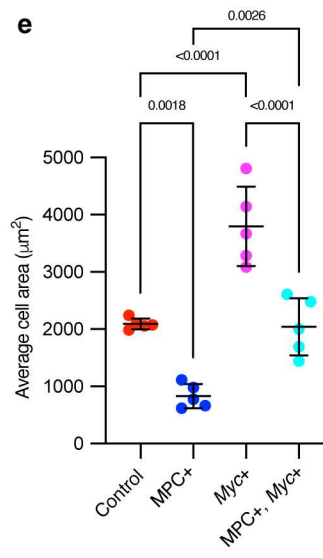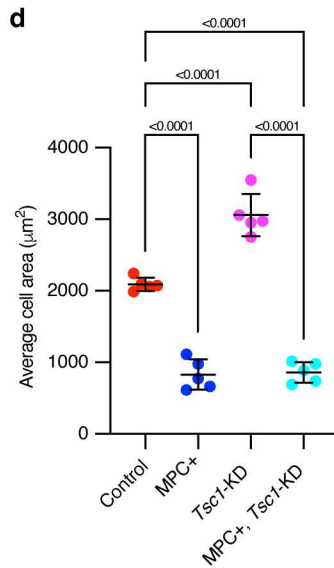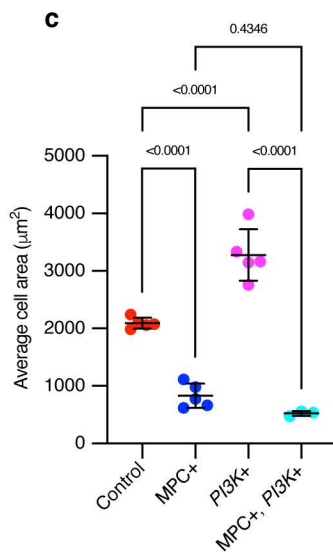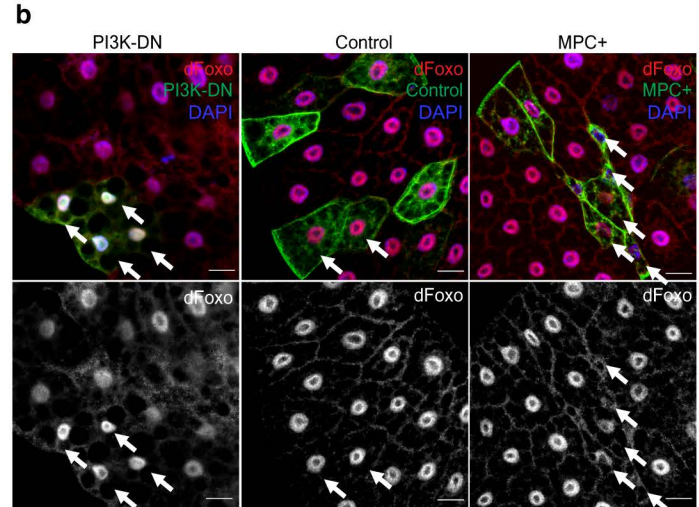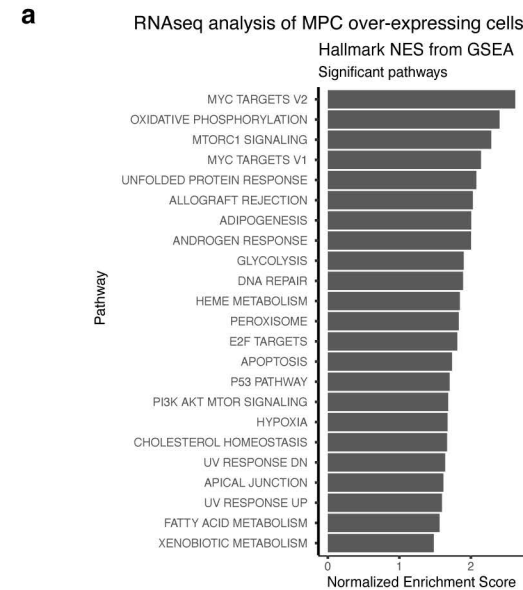
Supplementary Figure 3 – mTORC1 and Myc pathways are hyperactivated in MPC expressing fat body cells. (related to Main Figure 2)
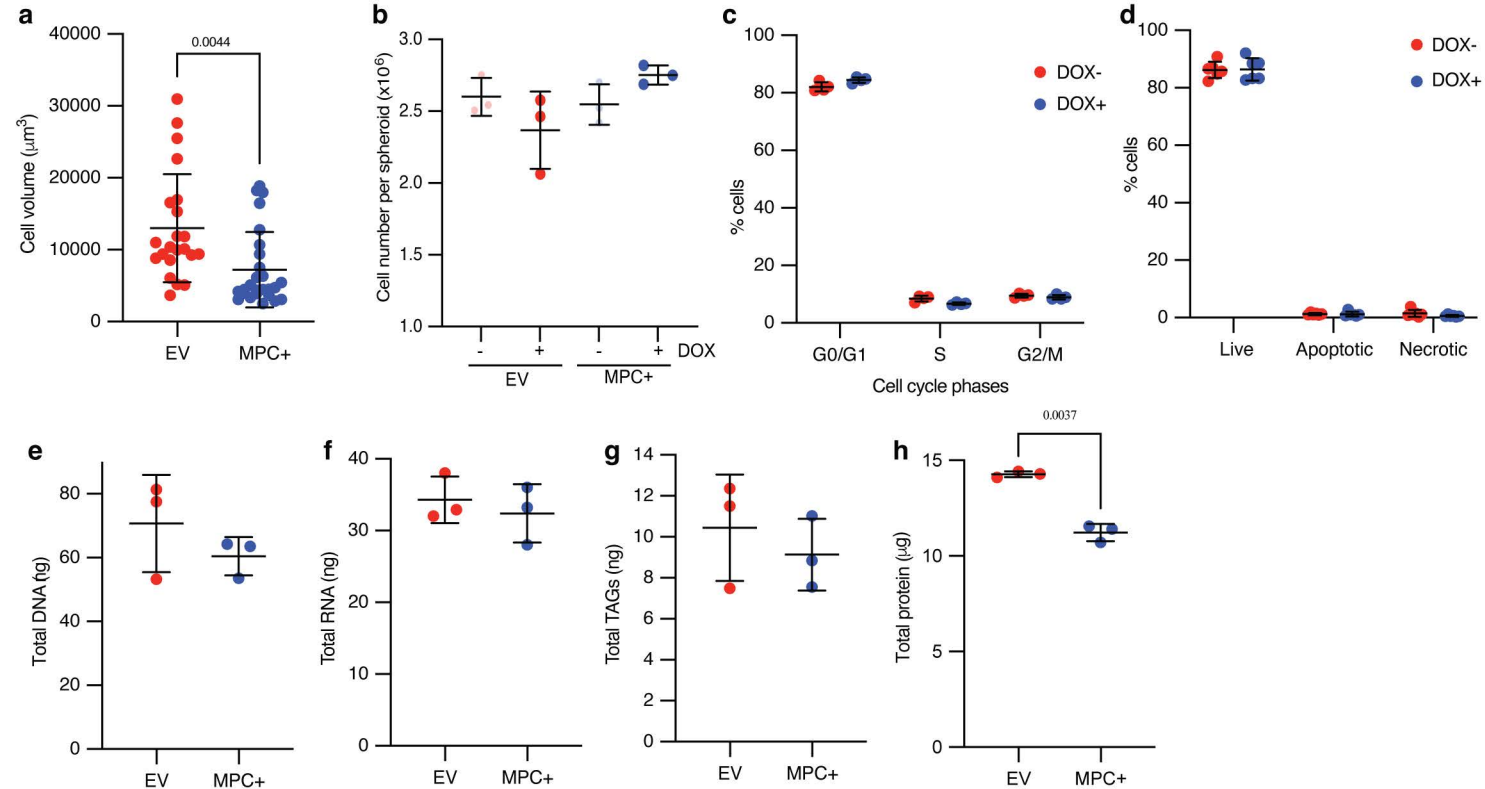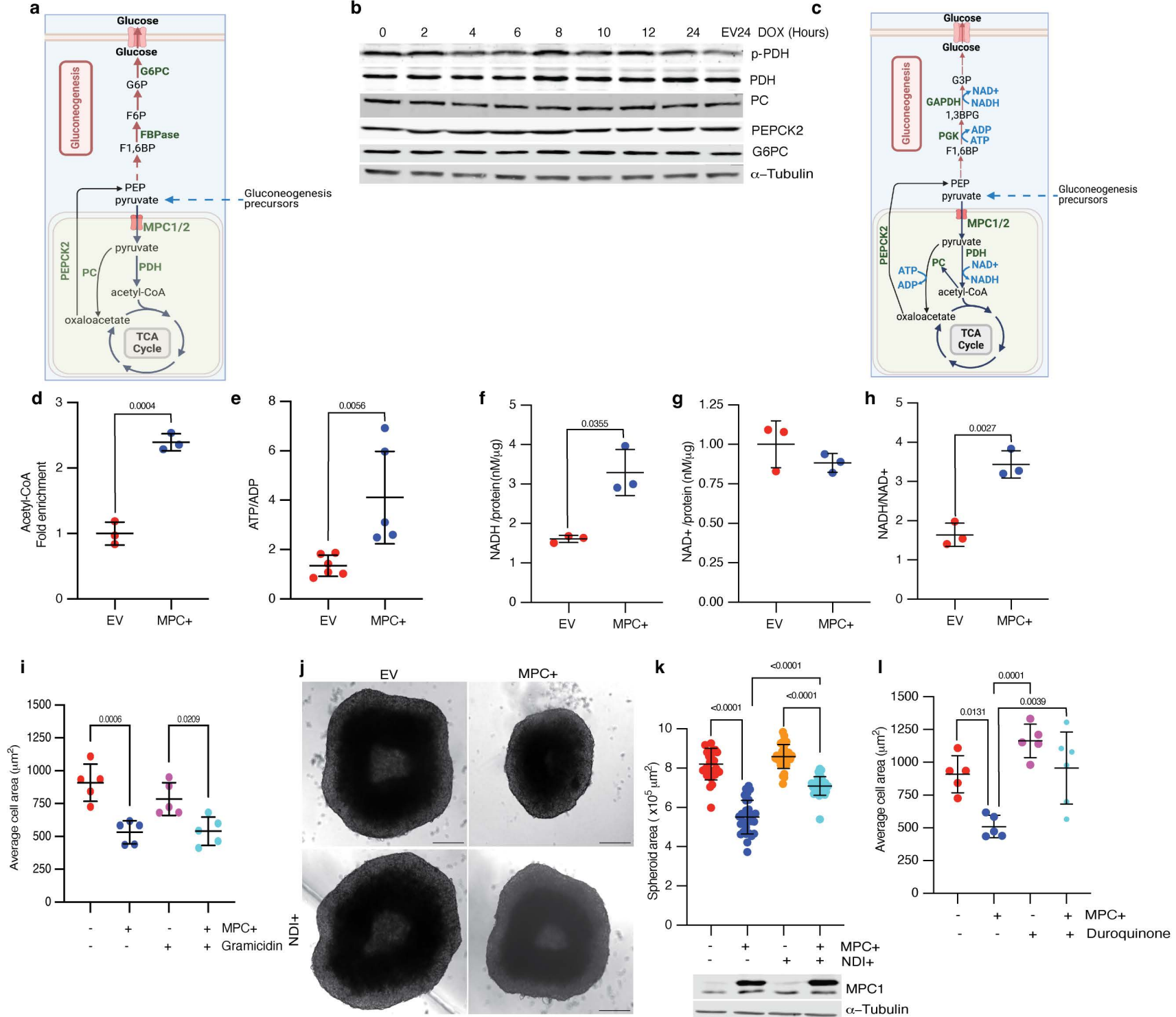
Supplementary Figure 4 – MPC expression reduces size of HepG2 cells in 2D and spheroid culture (Related to Main Figure 3).
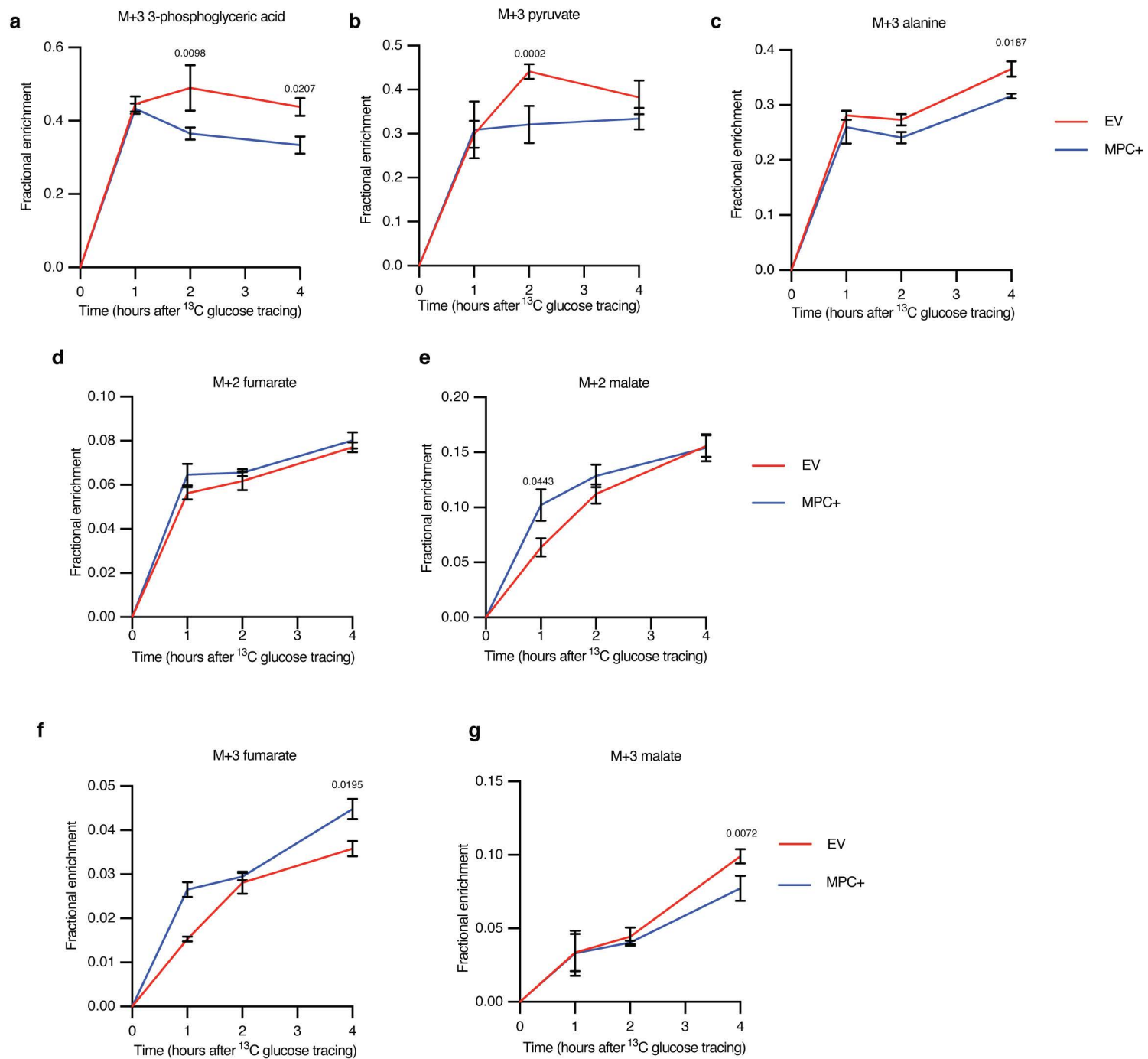
Supplementary Figure 5: ^{13}C glucose tarcing in MPC expressing HepG2 cells. (related to Main Figure 4)
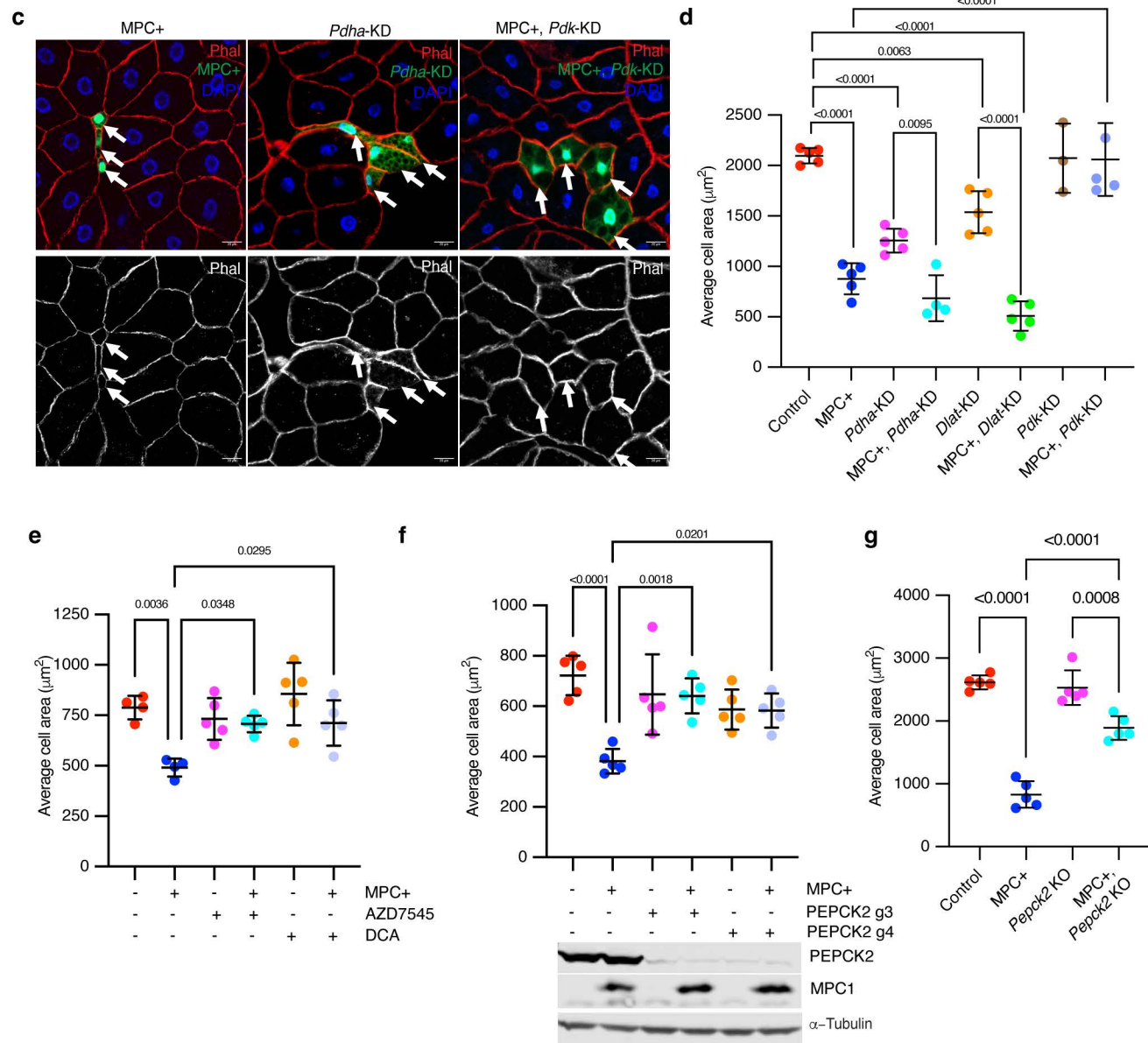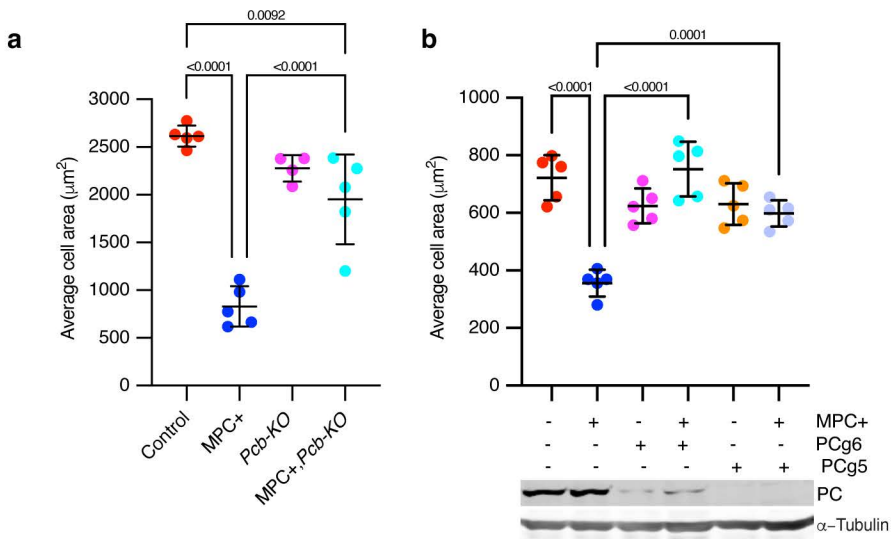
Supplementary Figure 6 - Elevated mitochondrial pyruvate transport increases gluconeogenesis. (related to figure 4)

Supplementary Figure 7 – Redox imbalance impedes protein synthesis and cell growth from elevated pyruvate metabolism in mitochondria. (Related to figure 5)
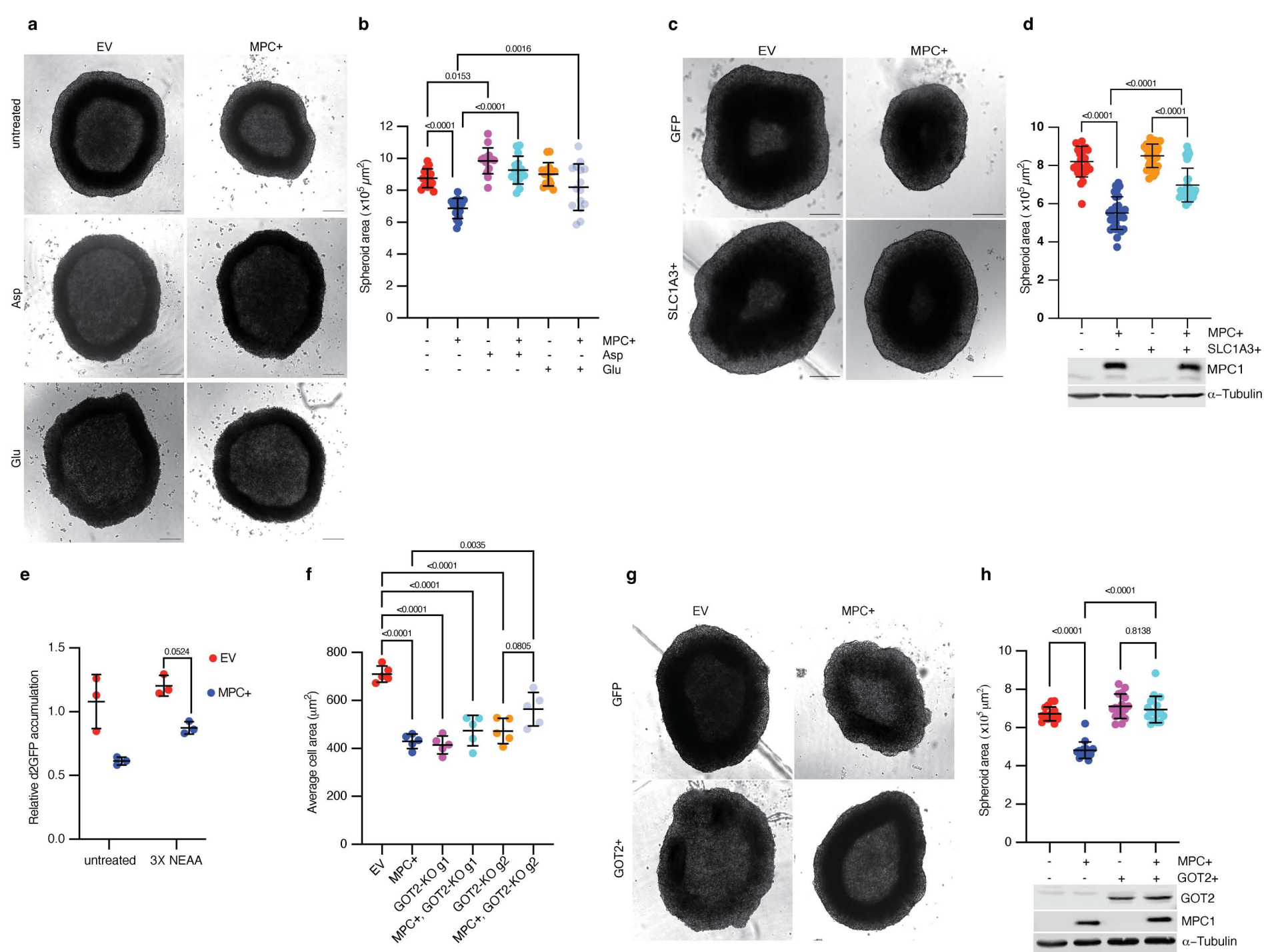
Supplementary Figure 8 – Reduced aspartate-glutamate abundance impairs size of MPC-expressing cells. (Related to figure 6)